

# Test Methodology Development for Contactless Proximity Coupling Systems Operating at Very High Bit Rates

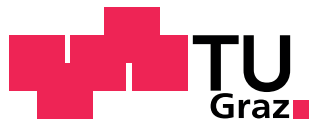
MASTER THESIS

by

DAVID SEEBACHER

---

Institute for Broadband Communication  
Faculty of Electrical and Information Engineering  
Graz University of Technology



Examiner: Ao.Univ.-Prof. Dipl.-Ing. Dr. Erich Leitgeb  
Supervisors: Dipl.-Ing. Dr. Michael Gebhart (NXP Semiconductors)  
Dipl.-Ing. Dr. Michael Stark (NXP Semiconductors)

Graz, June 2011

## STATUTORY DECLARATION

I declare that I have authored this thesis independently, that I have not used other than the declared sources / resources and that I have explicitly marked all material which has been quoted either literally or by content from the used sources.

.....

date

.....

(signature)

# Abstract

The increasing demand for higher data rates by new applications cannot be covered by the existing RFID systems operating at 13.56 MHz. The existing standard ISO/IEC 14443, that governs the communication between reader and cards currently defines data rates of up to 848 kbit/s. An amendment to this standard aims to introduce Very High Bit Rates (VHBR), enabling data rates of up to 6.78 Mbit/s based on multiple Phase Shift Keying (mPSK) or Amplitude Shift Keying (ASK). The current test methodology is defined for testing ASK transmission only. With the introduction of VHBR mPSK signals, a new test methodology to ensure interoperability between different reader and card manufacturers has to be defined.

The purpose of this thesis is to develop a test methodology based on the amendment to the test standard ISO/IEC 10373-6 and to verify this method on a real setup. A main parameter describing the signal quality besides the Signal to Noise Ratio (SNR), which is indirectly determined by the phase noise, is the amount of Inter Symbol Interference (ISI). Two parameters, namely  $ISI_m$  and  $ISI_d$ , are defined in the standard in order to provide measures for the ISI. Such a test methodology involves the generation of test signals with well defined ISI parameters and the analysis of these signals. The signal generation is accomplished by preprocessing the signal in software in order to set the test parameters and by making use of a special arbitrary waveform generator to provide the desired signal at the air interface. Signal preconditioning is used to compensate the channel influence.

For the signal analysis it was required to select an appropriate measurement instrument capable of measuring the mPSK signal with high accuracy. The measured signal undergoes postprocessing in software, firstly removing the frequency and phase errors before determining the correct sampling point for the final IQ-symbols. It was found that the proper determination of the sampling point is of utmost importance in order to measure the correct ISI parameters and therefore five different algorithms have been revised. Once the correct IQ-symbols are available the ISI and noise parameters are evaluated.

The test methodology is verified by performing a card reception test with a card evaluation system. By performing measurements on different antenna systems the signal analysis chain is verified and the range of ISI parameters that can be expected is determined. The test setup is now so far developed to be able to perform card reception tests with signals containing defined ISI. Furthermore the verification of reader signals is proven.

**Keywords:** RFID, VHD, VHBR, PSK signal analysis, contactless transponder test bench, ISI, NFC, ISO/IEC

# Kurzfassung

Der steigende Bedarf an immer höheren Datenraten für RFID Systeme im 13.56 MHz Bereich kann von den existierenden Systemen nicht mehr abgedeckt werden. Der existierende Standard ISO/IEC 14443 definiert die Kommunikation zwischen Karten und Lesegeräten und unterstützt Datenraten bis zu 848 kbits/s. In einer Ergänzung zum bestehenden Standard werden Very High Bit Rates (VHBR), Datenraten von bis zu 6.78 Mbit/s, basierend auf multiple Phase Shift Keying (mPSK) oder Amplitude Shift Keying (ASK), definiert. Die derzeitige Testmethode unterstützt nur das Testen von ASK Übertragungen. Durch die Einführung von VHBR ist es notwendig, die bestehende Testmethode um mPSK zu erweitern, um die Kompatibilität von Karten und Lesegeräten verschiedener Hersteller sicherzustellen.

Das Ziel dieser Diplomarbeit ist es, eine entsprechende Testmethode unter Berücksichtigung der Änderungsvorschläge für den Teststandard ISO/IEC 10373-6 zu entwickeln und mittels eines Testaufbaus zu verifizieren. Neben dem Signal to Noise Ratio (SNR), welches indirekt über das Phasenrauschen gemessen wird, ist die Höhe der Intersymbolinterferenz (ISI) ein wichtiges Maß für die Signalqualität. Im Standard sind zwei Parameter,  $ISI_m$  und  $ISI_d$  definiert, welche die ISI genauer spezifizieren. Die Testmethode beinhaltet die Erzeugung von Testsignalen mit genau definierten ISI Parametern, sowie die Analyse dieser Signale.

Zur Erzeugung der Signale an der Luftschnittstelle ist es notwendig, die Testsignale in Software zu berechnen, welche dann mittels eines speziellen Arbiträrsignalgenerators erzeugt werden. Um den Einfluss der Übertragungsfunktion der Antenne auf das Signal zu kompensieren wird ein Vorverzerrer eingesetzt.

Für die Signalanalyse war es erforderlich ein geeignetes Messgerät zur präzisen Messung des mPSK Signals auszuwählen.

Nach der Erfassung des Signals durch das Messgerät werden die Messdaten in Software nachbearbeitet, um unter anderem Frequenz- und Phasenfehler zu korrigieren. Nach diesen Korrekturen ist es notwendig den genauen Abtastzeitpunkt für die IQ-Symbole zu bestimmen, um die richtigen ISI Parameter zu messen. Daher werden 5 Algorithmen und ihre Eigenschaften genauer analysiert. Letztendlich werden die ISI Parameter, sowie das Phasenrauschen anhand der IQ-Symbole bestimmt.

Anhand von Kartenempfangstests mit Signalen innerhalb des definierten ISI Parameter-raums wird die Testmethode verifiziert. Messungen der ISI Parameter an Antennensystemen mit unterschiedlichen Eigenschaften bieten einen Anhaltspunkt für die in der Praxis auftretenden ISI Parameter. Mit dem präsentierten Testaufbau ist es nun möglich Kartenempfangstests unter dem Einfluss von ISI mit genau definierten Parametern durchzuführen. Darüber hinaus können die von Lesegeräten erzeugten Signale überprüft werden.

**Schlagnworte:** RFID, VHD, VHBR, PSK Signalanalyse, Kontakloser Transponder Prüfstand, ISI, NFC, ISO/IEC

# Acknowledgement

I would like to thank NXP Semiconductors for the opportunity to write this thesis. This thesis was accomplished in cooperation with NXP Semiconductors and I would therefore like to thank for this opportunity. Furthermore I would like to express my gratitude to my supervisors at NXP Michael Gebhart and Michael Stark for sharing their experience and knowledge in the area of HF engineering and signal processing with me, as well as for supporting me in any matter.

Special thanks goes to my supervisor at the TU Graz Erich Leitgeb, who agreed to supervise this thesis and supported me with many useful advice.

Also important to mention is the relaxed and welcoming employee attitude at NXP. I also appreciated the support from all colleagues in the laboratory whenever required. Moreover I would like to thank Martin Gossar and Walter Winkler for not only sharing the office, but also their long lasting experience within the VHD project with me.

I would also like to thank Ulrich Mühlmann for his explanations of the preequalizer and many fruitful discussions, as well as Christian Scherabon for his support regarding the FPGA box.

The members of the P40 team that accepted my limited availability during this time and supported me in many other belongings should not remain unmentioned.

Last but not least I want to say thanks to my family and all my friends supporting me during my studies.

# Contents

<b>1</b>	<b>Introduction</b>	<b>1</b>
<b>2</b>	<b>RFID Basics</b>	<b>3</b>
2.1	Fundamental Principles . . . . .	3
2.1.1	Components of a Contactless RFID System . . . . .	3
2.1.2	Classification of RFID Systems . . . . .	4
2.1.3	Card Architectures . . . . .	5
2.1.4	Card Interface . . . . .	5
2.2	Physical Principles . . . . .	6
2.2.1	Self Inductance . . . . .	6
2.2.2	Mutual Inductance . . . . .	7
2.2.3	Coupling Coefficient $k$ . . . . .	8
2.2.4	Resonant Circuit . . . . .	8
2.2.5	Induced Voltage . . . . .	10
2.2.6	Near/Far Field . . . . .	10
2.3	Properties of the Transponder . . . . .	12
2.3.1	Voltage Regulation . . . . .	12
2.3.2	Minimum Field Strength $H_{min}$ . . . . .	12
2.3.3	Detuning . . . . .	13
2.3.4	Load Modulation . . . . .	14
2.4	Digital Communication . . . . .	16
2.4.1	Digital Modulation Schemes . . . . .	16
2.4.2	Baseband Coding . . . . .	17
2.4.3	Forward Error Correction . . . . .	18
<b>3</b>	<b>Standards</b>	<b>20</b>
3.1	Life Cycle of a Standard . . . . .	20
3.2	ISO/IEC 14443 without VHBR . . . . .	21
3.2.1	Physical Characteristics . . . . .	21
3.2.2	Radio Frequency Power and Signal Interface . . . . .	22
3.2.3	Initialization and Anticollision . . . . .	23
3.2.4	Transmission Protocol . . . . .	26
3.3	ISO/IEC 14443 VHBR Amendments . . . . .	28
3.3.1	Radio Frequency Power and Signal Interface . . . . .	28
3.3.2	Initialization and Anticollision . . . . .	31
3.3.3	Transmission Protocol . . . . .	31
3.4	ISO/IEC 10373-6 . . . . .	31
<b>4</b>	<b>Measurement Instruments</b>	<b>34</b>
4.1	Signal Generation . . . . .	34
4.1.1	Performance . . . . .	35

4.1.2	Conclusion . . . . .	36
4.2	Signal Analysis . . . . .	37
4.2.1	Phase Noise . . . . .	37
4.2.2	Signal Processing Chain . . . . .	38
4.2.3	Synchronization . . . . .	40
4.2.4	Analysis Bandwidth and Effects . . . . .	41
4.2.5	Sampling Position Influence . . . . .	43
4.2.6	Measurement Results . . . . .	44
4.2.7	Final Considerations . . . . .	46
<b>5</b>	<b>Test Setup</b>	<b>47</b>
5.1	Transmission Channel . . . . .	47
5.1.1	Antenna Influence . . . . .	48
5.1.2	Preequalizer . . . . .	49
5.2	ISI Generation . . . . .	50
5.3	ISI Analysis . . . . .	52
5.3.1	Sampling Time Determination . . . . .	52
5.3.2	ISI Parameter Evaluation Algorithm . . . . .	55
5.4	Test System Performance . . . . .	59
5.4.1	Channel and Demodulation Filter Influence . . . . .	59
5.5	Phase Noise . . . . .	62
5.5.1	Noise Measurement . . . . .	62
5.5.2	Noise Generation . . . . .	64
5.6	Summary . . . . .	65
<b>6</b>	<b>Test Method Verification</b>	<b>66</b>
6.1	Automatisation . . . . .	66
6.2	PICC Reception Tests . . . . .	67
6.3	PCD Transmission Tests . . . . .	68
<b>7</b>	<b>Conclusion</b>	<b>70</b>
	<b>Bibliography</b>	<b>72</b>
	<b>List of Figures</b>	<b>75</b>
	<b>List of Tables</b>	<b>77</b>
	<b>List of Abbreviations</b>	<b>78</b>

# 1. Introduction

The increasing demand for higher data rates by new applications cannot be covered anymore by the existing Radio Frequency Identification (RFID) systems. In the ISO/IEC 14443 standard [1, 2, 3, 4], which regulates the communication of contactless transponders operating in the 13.56 MHz frequency band, data rates of up to 848 kbit/s are currently defined. The introduction of Very High Bit Rates (VHBR) based on multiple Phase Shift Keying (mPSK) enables data rates of up to 6.76 Mbit/s. For the currently defined data rates based on Amplitude Shift Keying (ASK) a well established test methodology exists, but the introduction of VHBR based on mPSK requires a new test methodology to ensure interoperability between different reader and card manufacturers.

The development of VHBR was done within the framework of the Very High Data Rates (VHD) project<sup>1</sup> that involves NXP semiconductors<sup>2</sup>, as well as several universities. The VHD project is focused on research to increase the data rates for contactless smart cards and Near Field Communication (NFC). The result of this research was used as input for the standardization process for the VHBR amendments to ISO/IEC 14443. Following these amendments the test methods according to ISO/IEC 10373-6 [5] have to be updated respectively. To assure interoperability two main measures are defined, that have to be within certain limits. The short symbol durations used for VHBR in combination with the properties of the transmission channel introduce Inter Symbol Interference (ISI). Therefore parameters describing the ISI are the first measure. Beside ISI the phase noise has a major influence on the stable communication and hence it is the second measure.

The purpose of this thesis is to develop a test methodology based on the amendment to the test standard [5] and to verify this method on a real setup. This includes the signal generation at the air interface with well defined ISI parameters and the measurement of these signals. In the generation of the test signals with well defined ISI parameters, software calculating these signals, as well as a signal generator are involved. For the signal analysis it was required to select an appropriate measurement instrument capable of measuring the mPSK signal and to develop sophisticated signal processing in software to measure the ISI parameters.

The second chapter starts out with the basics of RFID systems. It includes the fundamental principles of RFID, physical principles, properties of transponders and digital communication in general, laying a general groundwork for understanding the requirements for the test setup.

Chapter three then discusses the specifications governed by the ISO/IEC 14443 standard with its amendments. In detail the thesis covers the specifications on physical characteristics, RF power and signal interface, initialization and anticollision, as well as specifications on transmission protocols. The thesis furthermore strives ISO/IEC 10373-6 governing the current test method.

The main part firstly describes the selection of the appropriate measurement instruments, including the signal generator and the measurement instrument to analyze the signals at the air interface in chapter 4. In this context the different properties of two state of the art signal analyzers and one state of the art oscilloscope regarding the analysis of a Phase Shift Keying (PSK) signal on a 13.56 MHz carrier are pointed out.

---

<sup>1</sup>vhd.nfc-research.at

<sup>2</sup>www.nxp.com

Chapter five then describes the test setup itself. The main focus is set to the generation and analysis of signals with ISI. The influence of the Q-factor of the antenna on the signal shape and the mitigation of these effects using a preequalizer is shown. Different methods for the generation of signals with well defined ISI parameters will be compared. Additionally problems occurring when measuring the ISI parameters are outlined. The overall system performance is evaluated and finally verified by running Proximity Card (PICC) reception tests, as well as measuring the ISI parameters of various antenna combinations.

In the last part of this thesis the application of the test setup in a real life situation is documented. This part includes the automatisisation, a PICC reception test and the PCD test. Finally the conclusion sums up the comparison of the different applications, methods and recommendations on how the contactless test setup should look like.

## 2. RFID Basics

This section is dedicated to provide the basics about RFID system. The fundamental, as well as physical principles will be treated. But also the the properties of a transponder and digital communication in general will be explained.

### 2.1 Fundamental Principles

The fundamental components and principles of a Radio Frequency Identification (RFID) system will be introduced in this section. As this thesis deals with the contactless proximity air interface for smart cards and readers according to ISO/IEC 14443 [1, 2, 3, 4], operating in the 13.56 MHz band, the focus is set to this frequency. The 13.56 MHz band is a subset out of the available Industrial Scientific and Medical (ISM) bands. To provide a complete overview of RFID systems, also systems operating at 125/134 kHz (LF), 840-960 MHz and 2.4 GHz (UHF) are described in this section [6]. A general overview of the components of such a system, as well as their properties is given. Different card architectures as well as possible classifications of RFID systems are also treated in the following sections.

#### 2.1.1 Components of a Contactless RFID System

In figure 2.1 a basic RFID system working at 13.56 MHz is shown, consisting of the following main components:

- **Reader:** The reader supplies the card with an alternating magnetic field, powering the transponder and providing the time reference for the communication.
- **Transponder:** The transponder is the functional part in a card or a label. It consist of the transponder chip, the antenna and the assembly and is powered by the alternating magnetic field. The transponder responds to commands of the reader, processes the received data or sends data to the reader.
- **Application:** The application makes use of the data stored in the transponder, which can be used for a variety of purposes, such as access control (eg.: public transport) or identification (eg.: passport).

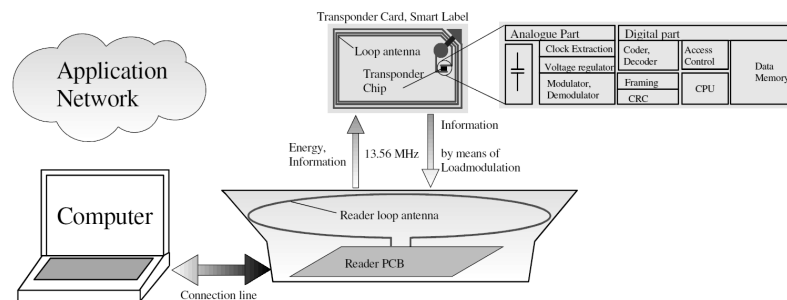


Figure 2.1: Components of a contactless RFID system [6]

## 2.1.2 Classification of RFID Systems

One possibility to classify RFID systems is to group them according to their properties from low-end to high end systems. An overview of different systems and their functionality and memory size can be seen in figure 2.2. Low end systems such as Electronic Article Surveillance (EAS) provide only basic functionality. Fixed code transponders offer a larger memory size, but are in general read only. With increasing functionality also the demand for memory size grows. Transponders supporting anticollision and eventually authentication procedures are located in the mid-range. These systems are normally based on simple state machines. Smart cards with and without cryptographic co-processor represent the high-end systems.

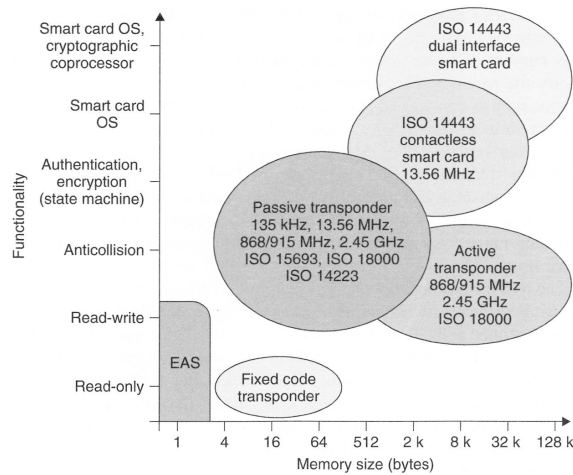


Figure 2.2: Classification of a RFID system [7]

Another possibility is to differentiate cards based on their interface, operating range and architecture. In figure 2.3 such a classification can be seen. On the left-hand side the class of contact interface cards according to ISO/IEC 7816 [8] and on the right-hand side contactless cards are shown. The contactless cards are further classified according to their spatial operating range from Close Coupled Card (CICC) defined by ISO/IEC 10536 [9] (meanwhile obsolete) over Proximity Card (PICC) defined by ISO/IEC 14443 [1, 2, 3, 4] and Vicinity Card (VICC) defined by ISO/IEC 15693 [10] to Remote Coupled Card (RICC). All cards are then further subdivided according to their architecture.

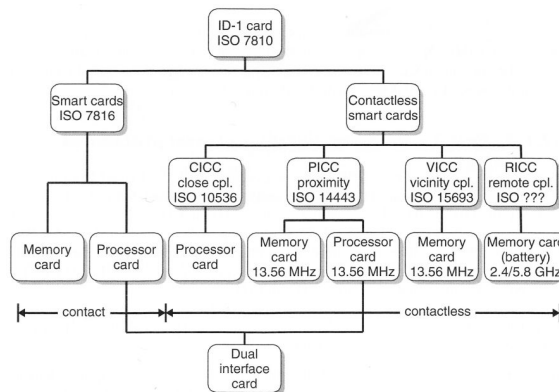


Figure 2.3: Contact(less) IC cards and applicable standards [7]

### 2.1.3 Card Architectures

There are basically two different types of card architectures, memory cards and microprocessor cards. Memory cards are based on a simple state machine and are optimized for a specific purpose. They store the data in a Electrically Erasable and Programmable Read Only Memory (EEPROM) and may also offer simple security features for access and for encryption and decryption. Memory cards have the advantage of very low power consumption and a simple architecture, which makes them very feasible for large scale low cost production. On the other hand they are not very flexible due to their hard-coded state machine. In figure 2.4 the architecture of such a memory card can be seen.

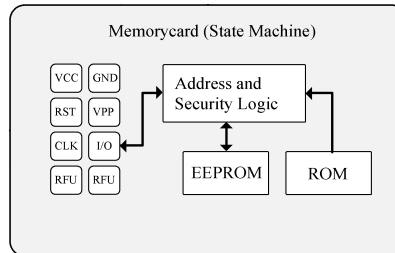


Figure 2.4: Architecture of a memory card [6]

Microprocessor based cards offer higher flexibility than the simple memory cards. They are based on a microprocessor, on which an Operating System (OS) is running. In figure 2.5 the basic architecture of such a microprocessor based card is shown. They have several memory areas: a Read Only Memory (ROM) containing the operating system, a Random Access Memory (RAM), which is used by the operating system, and an EEPROM, which is used for data storage. The EEPROM may also contain multiple customer build operating systems. Microprocessor based cards often additionally contain a *crypto coprocessor* to simplify cryptographic calculations.

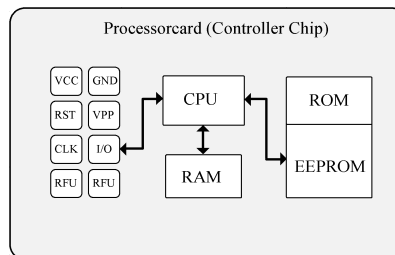


Figure 2.5: Architecture of a microprocessor card [6]

### 2.1.4 Card Interface

There are two different types of card interfaces, contact cards and contactless cards. These two can also be combined resulting in a dual interface card.

The specification of the contact interface is done by ISO/IEC 7816 [8]. In figure 2.4 and in figure 2.5 card architectures with contact interfaces can be seen. Contactless cards do not have a contact interface, the communication is based on the Contactless Interface Unit (CIU) only. In figure 2.6 a contactless microprocessor based architecture including the High Frequency (HF)-interface, the Central Processing Unit (CPU) and the memories, as described in section 2.1.3, can be seen.

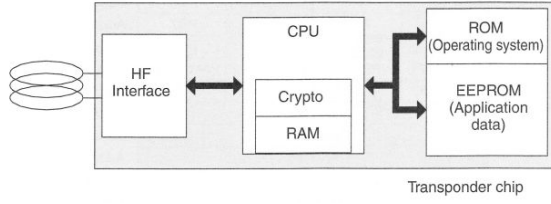


Figure 2.6: Contactless card architecture [7]

There is also the possibility of combining both interface methods in a single card architecture, as can be seen in figure 2.7. The communication with a dual interface card can be based either on the contact or the contactless interface.

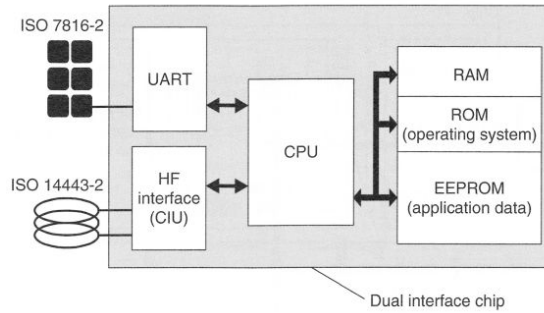


Figure 2.7: Dual interface card architecture [7]

## 2.2 Physical Principles

The physical principles describing the power supply and data exchange are of major importance for the understanding of RFID. Firstly the basics of the magnetic field including self and mutual inductance are outlined. The magnetic coupling between two conductors and the resulting induced voltage is also explained in this section, as well as the near and far magnetic field.

### 2.2.1 Self Inductance

Any current carrying conductor produces a magnetic field  $H$ , which is connected to the magnetic flux density  $B$  via  $\mu$  as shown in equation (2.1)

$$B = \mu \cdot H, \quad (2.1)$$

where  $\mu$  denotes the permeability. The magnetic flux  $\Phi$  itself for a homogeneous magnetic flux density  $B$  can then be calculated by using (2.2).

$$\Phi = B \cdot A \quad (2.2)$$

The generalization of equation (2.2) can be seen below:, where  $\vec{n}$  denotes the surface normal of to the conductor enclosed area  $A$ .

$$\Phi = \oint_A \langle \vec{B}, \vec{n} \rangle \cdot dA \quad (2.3)$$

Furthermore the total magnetic flux  $\Psi$  can be calculated as follows:

$$\Psi = \sum_N \Phi_N = N \cdot \Phi = N \cdot \mu \cdot \langle \vec{H}, \vec{n} \rangle \cdot A \quad (2.4)$$

The inductance is linked with the total magnetic flux  $\Psi$  and via the electric current  $I$  through the conductor, as stated in equation (2.5).

$$L = \frac{\Psi}{I} = \frac{N \cdot \mu \cdot \langle \vec{H}, \vec{n} \rangle \cdot A}{I} \quad (2.5)$$

A graphical interpretation of the above given formulas can be seen in figure 2.8, where the inductance of loop  $L$  can be calculated by its current, the resulting magnetic flux  $\Phi$  inside its area  $A$ .

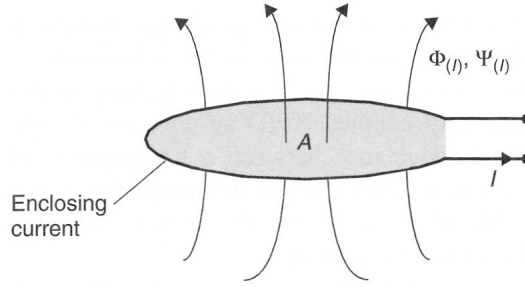


Figure 2.8: Illustration of the definition of inductance [7]

## 2.2.2 Mutual Inductance

The mutual inductance is defined by the total magnetic flux through the area  $A_2$  due to  $B_2$  and furthermore due to the electric current  $I_1$ , as can be seen in figure 2.9. Thus the mutual inductance describes the coupling between two loops, as it depends on the magnetic field in the second loop due to the current through the first loop.

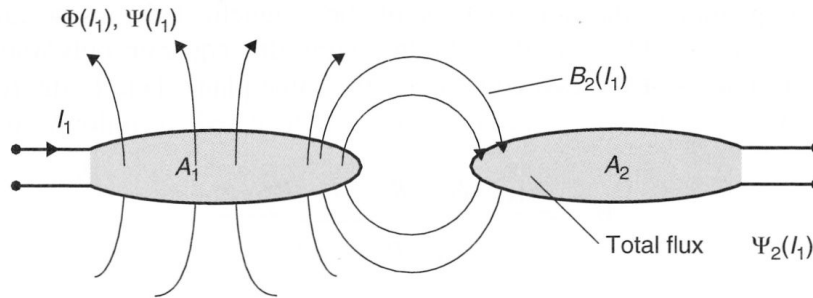


Figure 2.9: Illustration of the definition of mutual inductance [7]

The mutual inductance heavily depends on the location and dimension of the second loop, as it depends on the magnetic field of the first loop and the area of the second loop. The definition of the mutual inductance can be seen in equation (2.6).

$$M_{21} = \frac{\Psi_2(I_1)}{I_1} = \oint_{A_2} \frac{\langle \vec{B}_2(I_1), \vec{n} \rangle}{I_1} \cdot dA_2 \quad (2.6)$$

The definition above is also valid for  $M_{12}$ , when exchanging the current through the first loop by the current through the second loop  $I_2$  and substituting  $\Psi_2(I_1)$  by  $\Psi_1(I_2)$ . This yields:

$$M_{12} = \frac{\Psi_1(I_2)}{I_2} = \oint_{A_1} \frac{\langle \vec{B}_1(I_2), \vec{n} \rangle}{I_1} \cdot dA_1 \quad (2.7)$$

Therefore it can be concluded that the mutual inductance shows symmetric behavior and the following relationship applies:

$$M = M_{21} = M_{12} \quad (2.8)$$

The mutual inductance basically describes the (magnetic) coupling between two circuits, which is always present to a certain extent. The mutual inductance has the same unit as the inductance. The mutual inductance depends, as described above, on the dimensions and positions of the two loops. In figure 2.10 this dependence for different sizes of the first loop (reader antenna) can be seen. For the calculation of  $M_1$  a diameter of  $R_1 = 50$  cm, for  $M_2$  a diameter of  $R_2 = 7.5$  cm and for  $M_3$  a diameter of  $R_3 = 3.1$  cm was considered. It is assumed that the second loop (transponder antenna) remains constant, with  $R = 3.1$  cm and  $N = 1$  for all antennas.

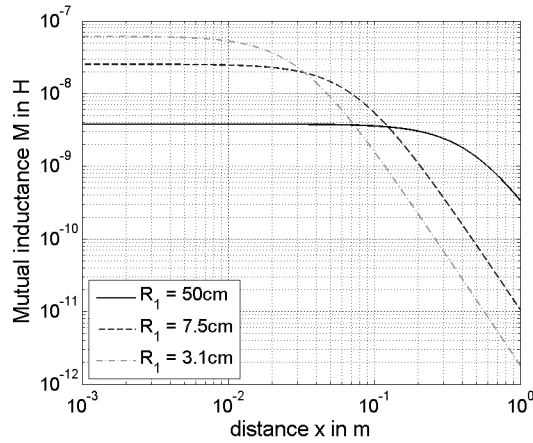


Figure 2.10: Mutual inductance of two loops

### 2.2.3 Coupling Coefficient $k$

While the mutual inductance is an absolute description of the coupling between two conductor loops, the coupling coefficient  $k$  describes the coupling between two conductors in a relative way, independent of their geometric dimensions. The coupling coefficient is defined as follows:

$$k = \frac{M_{12}}{\sqrt{L_{11} \cdot L_{22}}} \quad (2.9)$$

The coupling range for the coupling coefficient is therefore limited by  $0 \leq k \leq 1$ . For  $k = 0$  the two conductors are fully decoupled, due to shielding or sufficiently large distance between each other. At the second extreme  $k = 1$  the two conductors are fully coupled. This would apply to a transformer, when neglecting the fringe fields. The coupling coefficient for RFID systems in practical applications varies between 0.01 and 0.9 [6].

### 2.2.4 Resonant Circuit

The reader as well as the transponder antenna can be described as a first approximation by a simple resonant circuit. The antenna itself has an impedance which is mainly induc-

tive, but also to some certain extent resistive, due to the resistance of the wire, as well as radiation losses and losses caused by eddy currents. To obtain a resonant circuit it is necessary to add a parallel capacitance. For the transponder antenna some capacitance is already added by the chip itself, as the chip already contains an integrated input capacitance. This input capacitance of the chip is in some cases sufficient to get the desired resonant frequency. The resonant frequency of such a simple resonant circuit with the inductance  $L$  and the capacitance  $C$  can be calculated as given in equation (2.10).

$$f_{res} = \frac{1}{2 \cdot \pi \cdot \sqrt{L \cdot C}} \quad (2.10)$$

Every resonant circuit has a certain bandwidth determined by the (resistive) losses. This bandwidth is normally defined with the help of the Q-factor, which gives a dimensionless relation between the resonant frequency and the bandwidth. One definition of the Q-factor is given in equation (2.11), where the bandwidth is defined by the -3 dB points of the resonance peak.

$$Q = \frac{f_{res}}{\Delta f} = \frac{\omega_{res}}{\Delta \omega} \quad (2.11)$$

The general definition of the Q-factor is given in equation (2.12). It can be seen clearly that the higher the losses are, the lower is the Q-factor.

$$Q = 2 \cdot \pi \cdot \frac{\text{Energy stored}}{\text{Energy dissipated per cycle}} = 2 \cdot \pi \cdot f_{res} \cdot \frac{\text{Energy stored}}{\text{Power Loss}} \quad (2.12)$$

The Q-factor is a very important measure when considering the data rate, as the Q-factor is a limitation for higher data rates. As high Q-factor means a small bandwidth, which only allows slow modulation as otherwise the sidebands would be attenuated too much. Therefore the Q-factor is limited by the line coding and the data rates used. But on the other hand a high Q-factor is desirable, as less input power than for a low Q-factor is required to generate a specific field strength.

For most reader antennas the losses are very low and the resulting Q-factor is relatively high, for example in the order of 30. To achieve a lower Q-factor and a larger bandwidth an external resistor is added in this cases. The Q-factor ( $Q_0$ ) is usually given for the unloaded case, meaning that the circuit is not influenced (loaded) by it's connection line. However in practice the circuit is influenced by it's connection line and the external Q-factor  $Q_{ext}$  considers this coupling. The relationship between the loaded Q-factor  $Q_l$ , which is the resulting Q-factor when considering the influence of the connection is given in equation 2.13 below [11].

$$Q_l = \frac{Q_0 \cdot Q_{ext}}{Q_0 + Q_{ext}} \quad (2.13)$$

When assuming perfect matching the relation between  $Q_0$  and  $Q_{ext}$  is exactly 1, meaning that the external losses are equal to the internal losses of the resonant circuit. Calculating the result of equation 2.13 above for equal  $Q_0$  and  $Q_{ext}$  yields a loaded Q-factor that is only half of the unloaded Q-factor  $Q_0$ . This situation is valid for the reader antennas as well, when matched to the output impedance of the driving amplifier. Thus the operational (loaded) Q-factor of a reader antenna will only be half of the unloaded Q-factor  $Q_0$ , which is the measure that is referred to when talking about the Q-factor of an antenna.

### 2.2.5 Induced Voltage

The induced voltage in an unloaded antenna can be calculated by applying the law of induction, which is given in equation (2.14) below.

$$u_i(t) = -\frac{d\Phi(t)}{dt} \quad (2.14)$$

Applying the formula under the assumption of a sinusoidal input signal with a certain angular frequency  $\omega$  yields:

$$U_i = \Phi \cdot \omega = B \cdot A_e \cdot \omega = \mu \cdot H \cdot N \cdot A \cdot \omega \quad (2.15)$$

$A_e$  is the effective antenna area, which can be calculated by multiplying the real area  $A$  with the number of windings  $N$ . If the magnetic field is not perpendicular to the antenna the angle  $\alpha$  between the antenna and the field has to be considered as shown in equation (2.16).

$$U_i = \mu \cdot H \cdot N \cdot A \cdot \omega \cdot \cos \alpha \quad (2.16)$$

As the antenna is a resonant circuit, also the quality factor plays an important role, causing a resonance rise of the voltage. The quality factor of the transponder  $Q_T$ , including the influence of the chip, has to be considered for the induced voltage as well:

$$U_c = \mu \cdot H \cdot N \cdot A \cdot \omega \cdot \cos \alpha \cdot Q_T \quad (2.17)$$

The equation above is only valid for transponders with a resonant frequency being equal to the transmission frequency  $f_{res} = f_{carrier}$ . If the resonant frequency of the transponder is not equal to the transmission frequency the deviation from the resonant frequency and the quality factor influence the induced voltage. When considering  $f_{res} \neq f_{carrier}$  the voltage on the chip can be calculated as follows:

$$U_c = U_i \cdot \frac{1}{j \cdot \frac{\omega}{\omega_{res}} \cdot Q_T + \left(1 + \frac{\omega^2}{\omega_{res}^2}\right)} \quad (2.18)$$

If the resonant frequency is equal to the transmission frequency equation (2.18) simplifies to  $U_c = U_i \cdot Q_T$ , which is the same as equation (2.17) for an angle  $\alpha$  of 0 degree.

### 2.2.6 Near/Far Field

In figure 2.11 the dependence of the H-field on the distance over a cylindric coil (antenna) can be seen. As in section 2.2.2 the calculation is done again for 3 different diameters, namely  $R_1 = 50$  cm,  $R_2 = 7.5$  cm and  $R_3 = 3.1$  cm. The current was set to 1 A and one winding was used. The field remains approximately constant in the proximity of the loop and then starts to decay with approximately 60 dB per decade. The larger the loop the longer the field strength remains constant, but on the other hand a larger loop produces a smaller field strength close to the antenna.

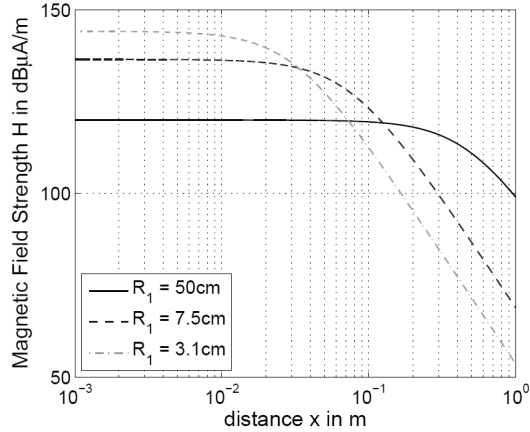


Figure 2.11: Magnetic field strength over a short cylinder coil

When reaching the far field the field strength furthermore heavily depends on the antenna orientation. In figure 2.12 the difference between the field strength in the coaxial and coplanar plane in dependence of the distance for a circular coil can be seen. In the vicinity of the antenna the field in the coaxial plane behaves as shown above and decays with 60 dB per decade, this is also true for the far field region.

Whereas the field in the coplanar plane has only in the vicinity of the antenna the same magnitude, when moving further away the field has a maximum and starts then to decay with 60 dB per decade as well. But when reaching the near to far field transition the behavior changes and the field starts to decay with only 20 dB per decade, due to free field propagation. The limit for the near to far field transition is given by the phase constant  $\beta$  which is defined as

$$\beta = \frac{\lambda}{2 \cdot \pi}, \quad (2.19)$$

where  $\lambda$  denotes the wavelength. For the carrier frequency of 13.56 MHz  $\beta$  is 3.52 m. As the transition between the near and the far field does not happen very rapidly a rule of thumb says that the following condition has to be met to be in the near field  $\beta \geq 3 \cdot \text{distance}$ . The equivalent condition for the far field is given by  $\beta \leq 0.3 \cdot \text{distance}$

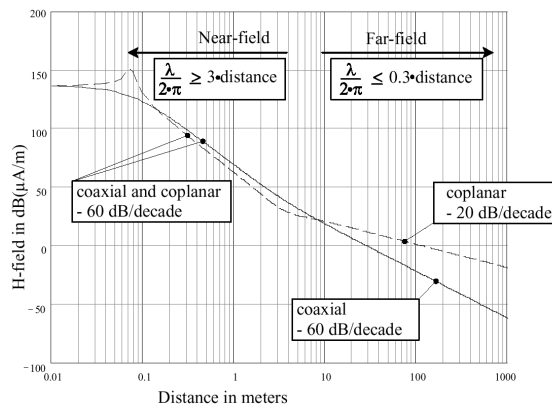


Figure 2.12: Magnetic field in the near/far field region for 13.56 MHz [6]

## 2.3 Properties of the Transponder

This section deals with the different properties of a transponder. Reaching from the power supply and its influence on the Q factor over the required minimum field strength to the load modulation generated by a transponder. Detuning effects between two stacked cards with relevant coupling are also included.

### 2.3.1 Voltage Regulation

As the digital part of the chip requires a constant voltage, the demand for voltage regulation arises. The power supply path usually consists of a rectifier, which is active in most cases, to achieve lower threshold voltages than with diodes for lower currents [6]. This enables to work at lower field strengths. The only drawback of using an active rectifier is the larger voltage drop for higher currents, which however does not really matter, as the current consumption grows with the field strength, once the regulation is necessary. Following the rectifier a transistor is placed, which acts as a shunt resistor, drawing current and causing a voltage drop in the antenna. Due to the current through the antenna the magnetic field within the antenna area and furthermore the induced voltage is reduced. The limiter current increases linear with the field strength, and as the voltage is kept constant the losses also increase only linear with the field strength. After the coarse regulation by the shunt resistor, a fine regulation is done by a low drop series regulator. The shunt resistor causes losses, and those losses directly influence the transponder Q-factor. This effect can be seen in figure 2.13. The Q-factor remains constant until the maximum supply voltage is reached and the limiter starts to work. This causes losses and the Q-factor decays with increasing field strength.

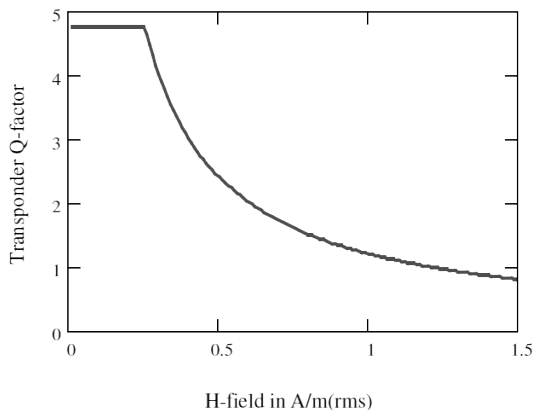


Figure 2.13: Transponder Q-factor in dependence of the magnetic field [6]

### 2.3.2 Minimum Field Strength $H_{min}$

The digital part requires a minimum voltage and furthermore a minimum field strength to operate, this defines the lower limit for the field strength. The internal supply voltage depends on the field strength, as well as the resonant frequency of the transponder antenna and the Q-factor, if not tuned to the transmission frequency. In figure 2.14 the required minimum field strength to reach 5 V on a 1.5 k $\Omega$  resistor, when tuning the resonant frequency  $f_{res}$  from 10 MHz to 20 MHz, is plotted. If the resonant frequency deviates from the transmission frequency of 13.56 MHz an increasingly higher field strength is required. The higher the Q-factor of the transponder and hence the lower the power losses, the faster the minimum field strength will increase when going away from the transmission

frequency. The minimum field strength increases more rapidly for lower than for higher resonant frequencies. It can be seen that the optimum value for the resonant frequency is the transmission frequency of 13.56 MHz, where the required field strength  $H_{min}$  has its minimum.

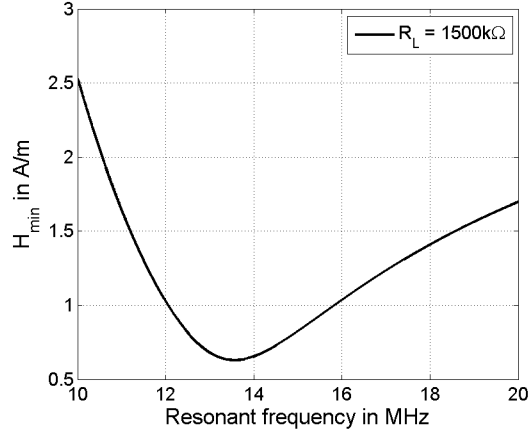


Figure 2.14:  $H_{min}$  in dependence of  $f_{res}$  of the transponder antenna

### 2.3.3 Detuning

Detuning of the resonance frequency occurs, when the coupling between two transponder antennas is significantly high. The resonant frequency is split into two resonances, one above and one below the original resonant frequency. For the limit case of  $k = 1$  the lower resonance is at a finite value below the original one while the upper resonance approaches infinity. For  $k = 1$  the lower resonant frequency can be calculated as stated in 2.20 according to [6].

$$f_{res,min} = \frac{1}{2 \cdot \pi \cdot \sqrt{\sum_{i=1}^n \left( \frac{1}{2 \cdot \pi \cdot f_{res,i}} \right)^2}} \quad (2.20)$$

When assuming that the resonant frequency of the transponder is set to 13.56 MHz, the two stacked cards would detune each other to a lower system resonant frequency of 9.59 MHz. For all coupling coefficients between 0 and 1 the resonant frequencies will lie within the above given limits and the original frequency. In figure 2.15 this effect is illustrated for different coupling coefficients.

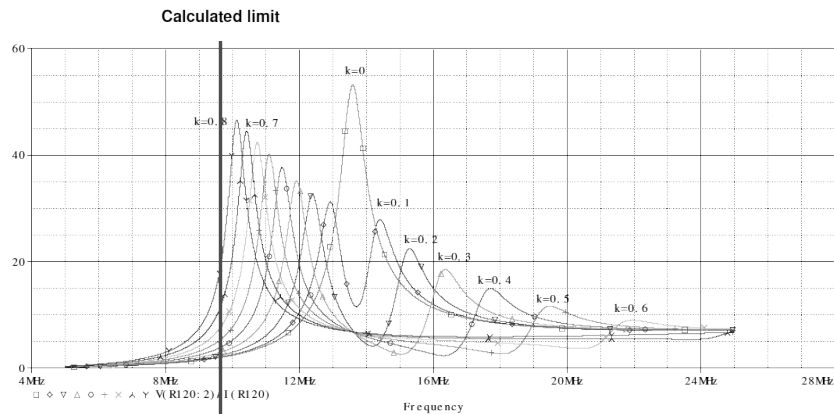


Figure 2.15: Detuning in dependence of coupling coefficient [6]

When the transponder circuit is tuned to 13.56 MHz the transponder circuit is detuned as described above, which would lead to a very high minimum field strength, as can be seen in figure 2.14. Therefore the resonant frequency of the transponder is usually set above the transmission frequency, so that for multiple cards the minimum field strength is not too high. A  $H_{min}$  as given in figure 2.14 and a single card tuned at 16.5 MHz will have approximately the same  $H_{min}$  for two stacked cards, which together have a resonant frequency of 11.67 MHz.

### 2.3.4 Load Modulation

The data transfer from the transponder to the card is usually done by means of load modulation. The load is either resistive or capacitive. A resistive load causes a lower Q-factor of the transponder during modulation, which can be detected by the reader. A capacitive load causes a shift of the resonant frequency. In most cases the modulation of the transponders response is done with a resistive load. In figure 2.16 a basic schematic overview for load modulation including the reader and the card can be seen. The receiver path in the reader is separated via a bandpass, which selects one of the two subcarriers.

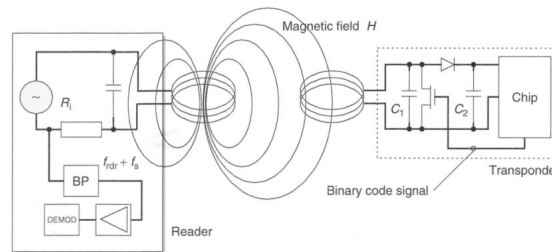


Figure 2.16: Basic load modulation schematic [7]

The generation of the modulation including the subcarriers can be seen in figure 2.17. The basis for the modulation is the subcarrier, which can be seen at the top of the figure. The subcarrier is usually derived from the supply field. In this case a 848 kHz subcarrier is generated by dividing the frequency of the supplying field of 13.56 MHz by 16. This division can be easily implemented in the hardware by using frequency dividers. The subcarrier is then multiplied with the baseband coded signal by using a logical AND resulting in the modulated subcarrier signal. In this case the baseband signal is Non Return to Zero (NRZ) coded. The modulated subcarrier is then applied to the switched load modulating the carrier signal of 13.56 MHz, resulting in the modulated signal with subcarrier, whose time domain representation can be seen at the bottom of the figure.

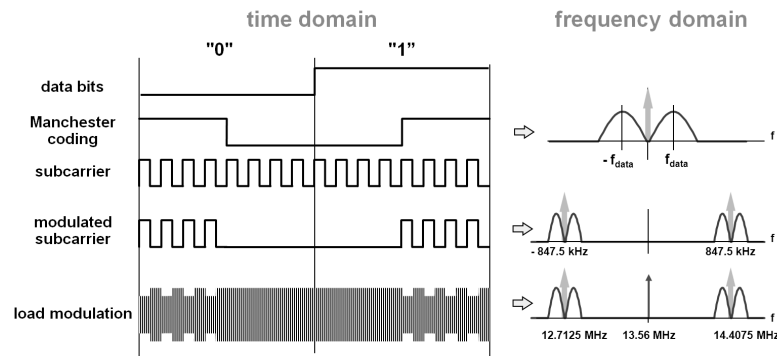


Figure 2.17: Generation of the subcarrier modulated signal [6]

In figure 2.18 the impedance of the transponder circuit with load ( $Q=15$ ) and without load ( $Q=60$ ) are shown. Additionally the frequency domain representation of the modulation signal from figure 2.17 can be seen, as well as the resulting subcarriers at  $\pm 212$  kHz including their sidebands at a  $Q$  of 30.

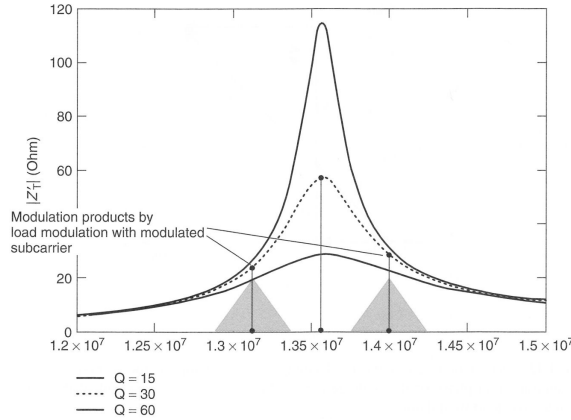


Figure 2.18: Load modulation with  $f_{carrier} = f_{res}$  [7]

In figure 2.18 the transponder is tuned to the transmission frequency of 13.56 MHz. In figure 2.19 the same as above is plotted with a resonant frequency of the transponder higher than the transmission frequency. It can be seen that in this case the sidebands have different levels. The resulting modulation is therefore a mixture of Amplitude Modulation (AM) and Phase Modulation (PM), not a pure AM. To properly detect the PM contribution to the modulation as well, it is necessary to perform Inphase Quadrature (IQ) demodulation [12]. Using an IQ demodulator gives also information about the phase, not only the amplitude of the signal.

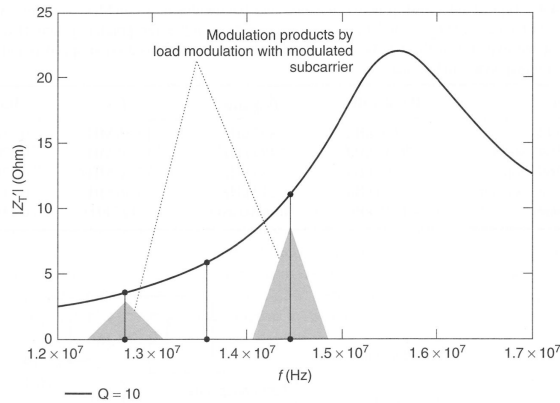


Figure 2.19: Load modulation with  $f_{carrier} < f_{res}$  [7]

The sideband level depends on the load that modulates the  $Q$ -factor, which also depends on the field strength and the current power consumption of the Integrated Circuit (IC) itself. To ensure stable communication the sideband level has to exceed a certain limit. For transponders according to ISO/IEC 14443-2 the limits for the load modulation can be seen in figure 2.20. The minimum sideband level is smaller for larger field strengths due to the lower  $Q$ -factor. This property as well as the therefore reduced influence of the load on the  $Q$ -factor can be seen in figure 2.13. The limits for the PICC are larger to provide a margin and assure interoperability. The sideband level has to be measured according to ISO/IEC 10373-6 [13], which describes the measurement methods for proximity cards and is treated in more detail in section 3.4.

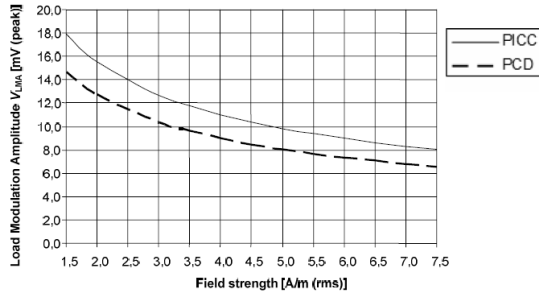


Figure 2.20: Load modulation amplitude minimum limits for a class 1 antenna [2]

## 2.4 Digital Communication

Different basic modulation schemes of relevance for RFID applications are discussed in this section. Furthermore different possibilities for baseband codings are included as well as Forward Error Correction (FEC) focusing on the Hamming code, which is used in the context of VHBR.

### 2.4.1 Digital Modulation Schemes

Digital communication means transmitting information from a sender to a receiver. This is done by transforming the digital symbol into a signal suitable for the transfer channel used. Information is usually transmitted using a sinusoidal carrier. A sine wave has three different properties, amplitude, phase and frequency, therefore all of those can be used to transfer information. The basic modulation schemes exclusively change one of the three parameters. In the lower part of figure 2.21 the three basic modulation schemes Amplitude Shift Keying (ASK), Phase Shift Keying (PSK) and Frequency Shift Keying (FSK) can be seen, whereas the upper part of the picture shows the data that is transmitted and the unmodulated carrier.

ASK is based on modifying the amplitude of the carrier. Whenever the data is zero in binary code, the carrier is completely attenuated, while when the data is one the plain carrier is sent. PSK changes the phase of the carrier. In this example a Binary Phase Shift Keying (BPSK) is plotted. For data bits equal to one the carrier's phase is set to  $180^\circ$ , having the exact opposite shape to the plain carrier. For data bits equal to zero the carrier remains unchanged. FSK uses a totally different approach. The information is transferred by using different carrier frequencies, varying the frequency according to the data sent.

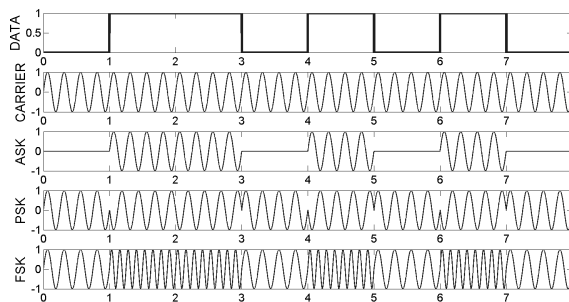


Figure 2.21: Basic modulation schemes

By combining the basic modulation schemes more advanced modulation schemes can be created. The above described basic schemes can also be enhanced by not only using binary but multiple states. For ASK this means that besides the amplitudes 0 % and 100 % states inbetween according to the modulation order exists. In case of FSK a set of different frequencies is used to represent more than two states for a symbol. Therefore it is possible to code more than one bit into one symbol. The modulation order usually corresponds to the power of two, so that the symbol can be directly mapped to a number of bits. For PSK different phase states are used to represent a symbol. In figure 2.22 the constellation diagrams for PSK with the order from 2 up to 16 can be seen. The constellation points are equally distributed around the circle for all orders to obtain a maximum distance between the points.

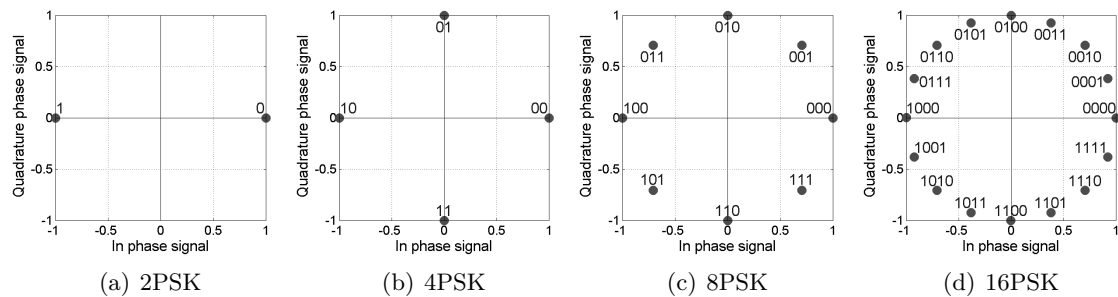


Figure 2.22: PSK symbol constellation diagrams

## 2.4.2 Baseband Coding

There are different methods for coding information in the baseband. The simplest one is the Non Return to Zero (NRZ) coding, where the level of the line simply corresponds to the logical level. In figure 2.23 the NRZ coding can be seen topmost.

The Manchester coding has a different translation. The information is contained in the edges of a signal at the middle of the bit duration. A positive edge corresponds to a logical one and a negative edge to a logical zero. At the beginning of the bit duration the level on the line changes accordingly to enable the right transition in the middle of the bit duration. This means that for a logical one the first half of the bit duration is set and otherwise the second half.

Whereas the signal returns to zero at the middle of each bit duration for the Return to Zero (RZ) coding, where the NRZ coding remains its level during the whole bit duration. For the Differential Biphas Coding (DBP) coding the signal changes at the beginning of each bit. If the bit is a logical one the signal level remains unchanged during the whole bit period. If the bit is zero there is a transition after the first half of the bit duration.

On the other hand a logical one is represented as an edge in the middle of the bit duration for the Miller coding. For a logical zero the signal remains unchanged, except if the previous bit was a zero, the signal level changes at the beginning of the bit duration.

The modified Miller coding is quite similar to the Miller coding. Whenever an edge would occur in the Miller coding, the signal is low for a certain time for the modified Miller coding. The rest of the time the signal remains high. The differential coding changes for each logical one the signal level at the beginning of the bit duration and remains unchanged for logical zeros.

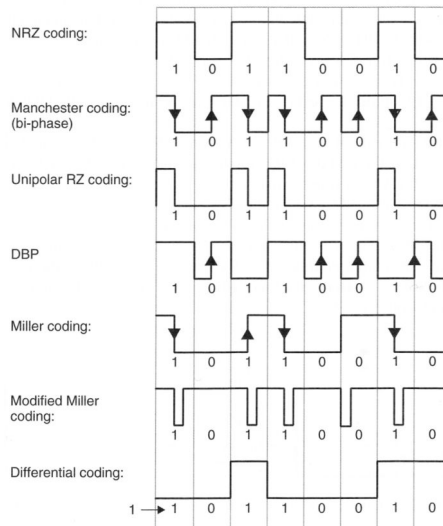


Figure 2.23: Different line codes [7]

### 2.4.3 Forward Error Correction

To reduce the demand for retransmissions of data due to errors during the reception Forward Error Correction (FEC) is used [12]. FEC systematically adds redundancy to the transmitted data, which is removed at the receiver again, to enable the detection and correction of an error during transmission. The detection and correction capabilities depend on the redundancy added to the data. Mainly two different groups of FEC exist, block codes and convolutional codes [12]. Block codes add redundancy to a block of a certain length, based on the bits within this block. Convolutional codes on the other hand add redundancy to a data stream, where the added bits depend on the subsequent bits and the coding is done in a continuous manner. Convolutional codes have good error correction capabilities, but with increased computational complexity during coding and decoding. As the complexity has to be kept low for RFID applications, as power and chip area consumption are a limitation, the use of block codes is favored.

One possible FEC is the Hamming code. The Hamming code is capable of detecting and correcting one and to detect two erroneous bits. A simple parity bit on the other hand is only able to detect a single error and fails to detect two erroneous bits. By using a parity a detected error results in a retransmission, whereas when using FEC the original sent bit can be restored and no retransmission is required. The hamming code is a block code, using parity bits to protect the data. The notation of the code is Hamming(m,n), where m defines the block length in bits and n the number of data bits.

The number of parities is simply the difference between them and depends on the number of bits to protect and can be calculated by  $N_{par} = \text{ceil}(\text{ld}(N_{data}))$ . The region over which a parity is calculated is defined by its number. When looking at the index of bit position in binary representation, the number of the parity indicates the significance of the bit considered for the calculation of parity. Whenever this significant bit of the index is set, the parity is calculated over this data.

In table 2.1 a Hamming(7,4) code is presented. It can be seen that the parity 0 is calculated for each position where the Least Significant Bit (LSB) is set in the bit position. For the second parity it is the bit with the next significance and so on. If the parity bits would be simply added to the block the parity bits themselves would be prone to errors. Therefore the parity bits are included into the block and placed at each bit position that corresponds to a value of the power of 2. This means the parities are placed at the positions 1, 2, 4 and

so on, as can be read out of table 2.1. A parity is denoted with  $P$  and the data over which it is calculated with  $D$ . At this position only one parity covers the data and therefore the parity itself is placed at this location. At position zero no parity would cover the data at all. Therefore this position is skipped and the overall length of the block including the parity bits is limited according to  $N = 2^k - 1$ , where  $k$  is the number of parities used.

If a block length equal to the limit is chosen the code is optimal according to its detection and correction capabilities. The total amount of data bits in a frame can then be calculated by subtracting the number of parities from the maximum frame size, as given by  $N = 2^k - 1 - k$ . By locating the data and parities according to the scheme in table 2.1 the position of an erroneous bit can be exactly determined by looking at the incorrect parities. Any data bit is protected by at least two parities and none of the data bits is protected with the same combinations of parities. Therefore the combination of wrong parities reveals the bit position. If only one parity is wrong it can be concluded that the parity itself was corrupted and not the data. When adding an overall parity ( $bit_0$ ) to the data the parity gives information about the number of errors (even or odd). The use of this information together with the other parity information gives the possibility to detect a double error but not correct it.

bit position	dec	1	2	3	4	5	6	7
	bin	001	010	011	100	101	110	111
parity 0		P		D		D		D
parity 1			P	D			D	D
parity 2					P	D	D	D

Table 2.1: Hamming(7,4) code

# 3. Standards

In this chapter the relevant standards for RFID products in the 13.56 MHz band will be discussed. A short introduction about the life cycle of a standard eases the understanding of the development of such a standard. The product standard ISO/IEC 14443 and its amendments for VHBR will be introduced and furthermore the corresponding test standard ISO/IEC 10373-6 will be presented.

## 3.1 Life Cycle of a Standard

The development of an International Standard can be divided into several steps, reaching from a first draft to the final standard. The sequence of the procedure is as follows:

- **Working Draft:** First draft in form of a structured document, created by one of the members of the committee.
- **Committee Draft:** Consulted document including all parts. Technical and editorial comments are still possible.
- **Final Committee Draft:** From this stage onwards only editorial changes are possible.
- **Final Draft International Standard:** Identical version of the International Standard, which is used for the final balloting.
- **International Standard:** Legally binding version of the standard.

Figure 3.1 shows the life cycle of an International Standard and all transitions between the different states. Based on the working draft, the committee draft is created. The committee draft is edited until all technical questions are detached. In the stage of the final committee draft all editorial issues are clarified. The final draft of the International Standard can not be changed anymore. If the final draft international standard is accepted it reaches the state of a legally binding standard. If the standard is not accepted it falls back to the working draft stage.

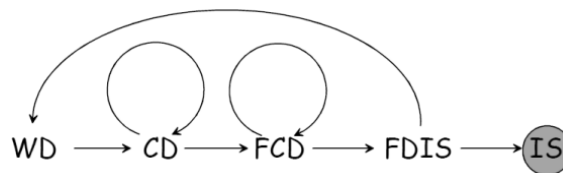


Figure 3.1: Life cycle of an international standard [6]

During the lifetime of a standard it may be extended by amendments. An amendment only includes the changes in a standard, not the modified version. Approximately every 5 years there is a new standard released including all amendments. The life cycle of such a amendment can be divided into the following parts:

- **Preliminary Draft Amendment:** First draft in form of a structured document, created by one of the members of the committee.
- **Final Preliminary Draft Amendment:** Consulted document including all parts. Technical and editorial comments are still possible.
- **Final Draft Amendment:** Amendment which is used for the final balloting.
- **Amendment:** Legally binding version of the amendment.

In figure 3.2 the life cycle of an amendment is plotted. The working basis is as for the International Standard a draft created by one of the members of the committee, which then becomes a final preliminary draft of the amendment. In this stage technical and editorial changes are still possible. The next stage is the final draft amendment, which is the identical version of the amendment used for balloting. The last state is the legally binding amendment.

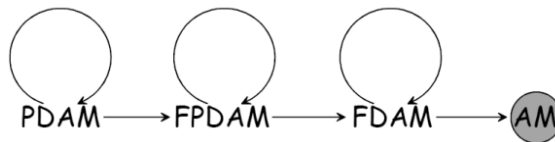


Figure 3.2: Life cycle of an amendment [6]

## 3.2 ISO/IEC 14443 without VHBR

This section will describe in greater detail the ISO/IEC 14443 standard without the amendments for VHBR, published by the International Organization for Standardization (ISO) and International Electrotechnical Commission (IEC). The standard is divided into 4 Layers. Layer 1 deals with the physical characteristics of a transponder card. Layer 2 describes the radio frequency power and signal interface. The initialization and anticollision is defined in layer 3. The transmission protocol is treated in layer 4.

### 3.2.1 Physical Characteristics

Part 1 of the ISO/IEC 14443 standard [1] defines the physical characteristics of a card. Different geometries for the transponder antenna are defined, ranging from class 1 to class 6 [14]. In figure 3.3 the definitions of the dimensions of a class 1 compliant to ISO/IEC 14443-1 are given. Furthermore this standard defines the exposure limits of the maximum field strengths.

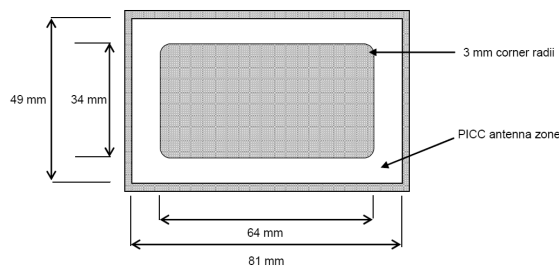


Figure 3.3: Class 1 antenna size [1]

### 3.2.2 Radio Frequency Power and Signal Interface

Part two [2] describes the RF-interface including modulation patterns. One distinguishes between Proximity Coupling Devices (PCD) to PICC and PICC to PCD communication direction. The PCD to PICC communication is based on AM. The standard supports two different types, namely type A and type B, with different properties. In figure 3.4 the used coding for the PCD to PICC communication can be seen. Type A uses a modified Miller coding and type B is based on NRZ coding. Both base band coding schemes are described in section 2.4.2. The following picture shows the coding of the PCD to PICC communication.

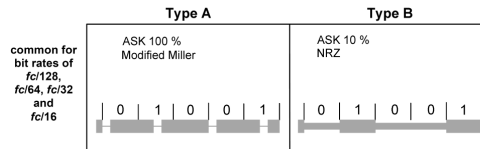


Figure 3.4: Coding PCD to PICC [2]

The coding described above is used for all defined data rates. All available data rates for both directions PCD to PICC and PICC to PCD are given in table 3.1.

Carrier divisor	Bit Rate
$fc/128$	$\sim 106$ kbit/s
$fc/64$	$\sim 212$ kbit/s
$fc/32$	$\sim 424$ kbit/s
$fc/16$	$\sim 848$ kbit/s

Table 3.1: Data rates PCD to PICC and PICC to PCD [2]

The communication direction PICC to PCD is a bit more complex due to the load modulation using subcarriers, as described in section 2.3.4. For the base data rate of 106 kbit/s the two different types use a different modulation and coding. Type A uses On Off Keying (OOK) of the subcarrier based on Manchester coding, whereas type B uses BPSK based on NRZ coding.

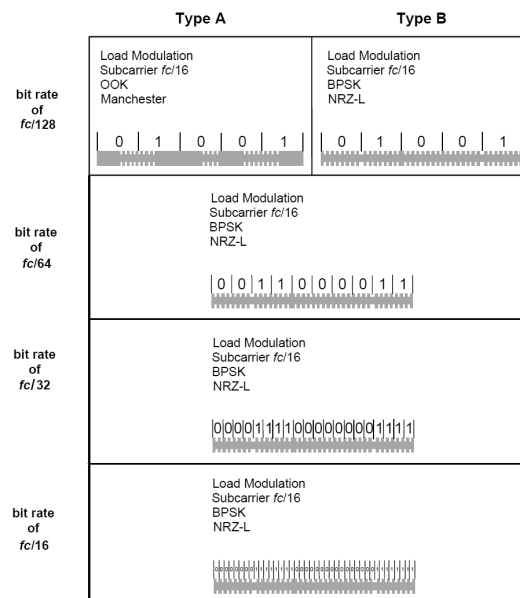


Figure 3.5: Coding PICC to PCD [2]

The coding for the base data rate is of major importance to the anticollision sequence described in section 3.2.3. For higher data rates there is no difference in the channel/line code between type A and type B anymore. Also the same coding as for type B in the base data rate is used for type A.

Also the limits for the deviation from the optimum modulation characteristics are defined in this part. This includes the specification of limits for the timing and the amplitude of the envelope signal. Due to the band limited transmission channel, especially for antennas with high Q-factors the modulation signal may be distorted. Therefore the envelope of the modulation pattern is of major interest for error free information decoding. In figure 3.6 the definition of the timing parameters for the PCD to PICC communication for type A is plotted. The definition for a data rate of 106 kbit/s can be seen in (a).

Each of the timing parameters has to be within certain limits. The limits for the signal generated by a PCD are lower than the limits for which a PICC has to be able to correctly receive the sent signal. The margin between these two limits is to ensure interoperability. Additionally an overshoot of maximum 10 % is allowed. For higher data rates the nominal modulation index of 100 % can not be achieved anymore due to the band pass character of the transmission channel. Therefore the definition of the timing parameters is different for higher data rates. In (b) the parameter definition for higher data rates from 212 kbit/s to 848 kbit/s is given.

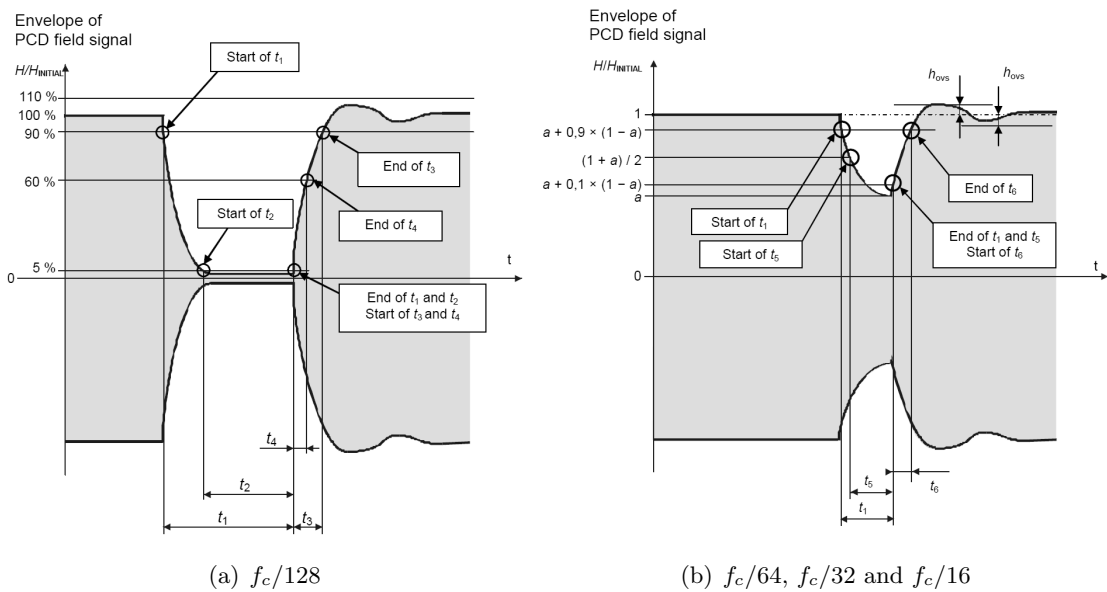


Figure 3.6: Pause A for PCD to PICC transmission [2]

### 3.2.3 Initialization and Anticollision

This part of the ISO/IEC 14443 [3] defines the initialization and anticollision procedure of a transponder are described in this section. Furthermore this part describes the different states of the transponder and the transitions between them including the timing, as well as the selection of one out of multiple cards in the field.

The state diagram of a transponder for type A can be seen in figure 3.7. Once a card is powered it is in the IDLE state. The PCD polls for new cards in it's operational volume by using the Request Command Type A (REQA) or Wake Up Command Type A (WUPA), which brings the transponder into the READY state. All other commands are ignored and the transponder remains in the IDLE state. Each transponder has a Unique

Identifier (UID), which is used for identification. The UID may be 4 (single), 7 (double) or 10 bytes (triple) long. In the READY state it is decided according to the UID whether the transponder is of interest or not.

If there is more than one transponder in the field, a collision in the response to the REQA or WUPA occurs and has to be resolved by using the Anticollision Command (AC). The anticollision is described in more detail later in this section. A positive AC command does not change the state of the transponder. Once all UIDs are available one transponder is selected by using the SELECT command, which brings the transponder into the ACTIVE state.

All other commands except the AC command cause the transponder to be reset to the IDLE state. From the ACTIVE state the ISO/IEC 14443-4 mode can be entered by using the Request for Answer To Select (RATS), defined in ISO/IEC 14443-4 [4], but any other proprietary protocol may also be entered. Any error or illegal command causes the transponder to be reset to the IDLE state. By sending a Halt Command Type A (HLTA) in the ACTIVE state or by deselecting the transponder from a higher level protocol, the transponder reaches the HALT state. The HALT state is similar to the IDLE state, except this state can only be reached once the transponder was activated. In this state the transponder only responds to a WUPA, that is how this state can be distinguished from the IDLE state.

The states READY\* and ACTIVE\* are similar to the READY and ACTIVE states, with the exception that they can only be reached from the HALT state. Any error that causes a reset to the IDLE state in READY and ACTIVE states causes a reset to the HALT state for the READY\* and ACTIVE\* states.

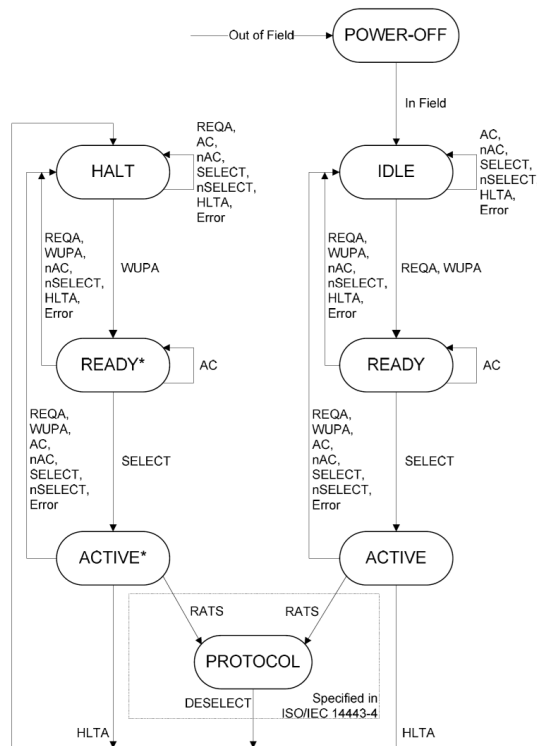


Figure 3.7: Type A state diagram [3]

The activation of a transponder will now be described in more detail. To enter the READY state from the IDLE state a REQA or WUPA command is sent. The answer to both commands is the Answer to Request Type A (ATQA). The ATQA contains information about the used anticollision procedure, the UID length, some proprietary and Reserved

for Future Use (RFU) bits. The ATQA is sent simultaneously by all transponders in the field. To ensure that all transponders respond simultaneously the definition of the Frame Delay Time (FDT) is very stringent for these commands. The FDT defines the time from the end of the PCD command to the beginning of the PICC response.

If there are multiple cards in the field and not all of them have the same ATQA, respectively UID, a collision will occur. This collision has to be detected by the PCD in order to resolve it. In figure 3.8 the responses of two transponders sending different data for NRZ and Manchester coding can be seen. The fourth and fifth bit in the data stream differs in the responses and a collision occurs. In the upper part of the figure the responses of the two transponders using NRZ can be seen. Below them there is the combined signal at the reader and the decoded version of it. In the decoded data stream the dominant state (the "1") is selected and the collision is not detected.

In the lower part of the picture the same situation using Manchester coding is plotted. Again there are the responses of the transponders and their combined signal at the reader. The Manchester coding uses either the first or the second half of the bit duration to code the bit. The resulting signal at the reader is then modulated in the first or the second half of the bit. If a collision occurs and the two received bits are different, as for the fourth and fifth one, the collision can be detected. As for two different received bits the modulation lasts the whole bit duration the coding is invalid. Therefore the collision can be detected. The whole selection procedure is done at the base data rate of 106 kbit/s. To be able to detect a collision the coding (described in section 3.2.2) for type A at the base data rate is different from all the other data rates.

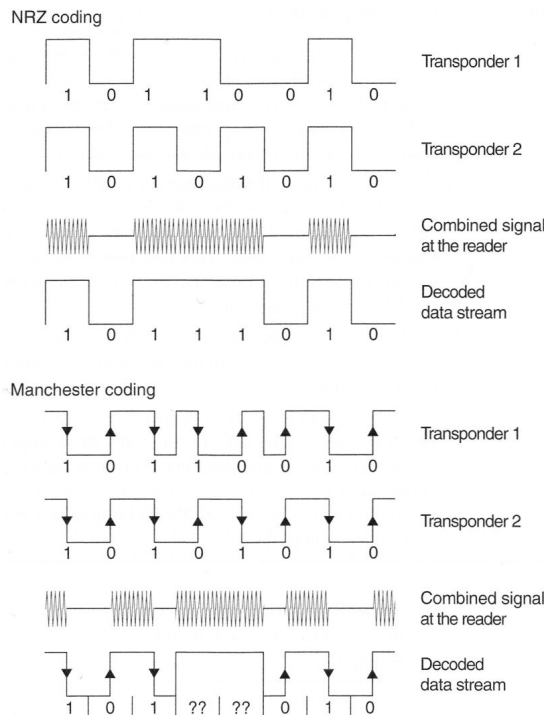


Figure 3.8: Collision detection for NRZ and Manchester coding [7]

After the ATQA was received, the selection of the transponder and the anticollision sequence is started by using the Selection code (SEL) followed by the Number of Valid Bits (NVB). The SEL command defines the cascade level. The maximum cascade level necessary depends on the length of the UID. The NVB defines how many bits of the UID are valid. The PICC responds to the command with its UID from the number of valid bits onwards. If there is a collision detected the NVB is set to the point of collision and the

UID up to the point of collision of one of the two transponders is sent. Only the selected transponder responds then with the rest of its UID. This procedure is repeated, until no collision occurs anymore and the complete UID is known by the PCD.

Once the full UID is known, the so-called selection command, which is the same command as above with the entire UID including a Block Check Character (BCC) and a Cyclic Redundancy Check (CRC) at the end, is sent to the PICC. The PICC responds then with the Select Acknowledge (SAK), which gives information about whether the UID is complete or not. If the UID is not complete the procedure above is repeated for the next cascade level. If the UID is complete the SAK also reveals if the transponder is compliant to ISO/IEC 14443-4. If a collision occurred during the selection procedure the active transponder is sent to the HALT state and the procedure is repeated until all UIDs are known. Based on the UID or on any other (proprietary) selection criterion, the desired transponder is selected.

### 3.2.4 Transmission Protocol

In part 4 of the ISO/IEC 14443 standard the block transmission protocol, as well as the setting of different parameters, such as data rate are defined. In figure 3.9 the activation sequence of a PICC defined in part 3 and 4 of ISO/IEC 14443 can be seen. The first part including the anticollision and selection procedure was already described in section 3.2.3.

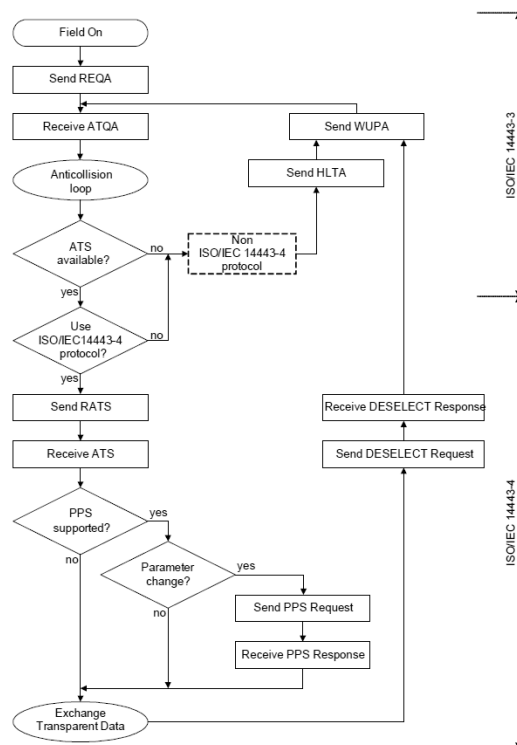


Figure 3.9: Activation sequence [4]

In the second part following the anticollision and the check of the availability of the Answer To Select (ATS), respectively compliance to ISO/IEC 14443-4, the Request for Answer To Select (RATS) is sent. The ATS is then returned by the PICC containing information about the different parameters supported by the transponder. The ATS contains information on whether and which parameters can be changed by using the Protocol and Parameter Selection (PPS) command.

If the PPS command is not supported or no parameters have to be changed, the application can start to exchange data. If parameters have to be changed this is done by using the PPS which will be described later in more detail. The transparent data exchange can be left by sending a deselect command to the PICC, which brings the transponder back into the HALT state as described in section 3.2.3.

The RATS command includes a start byte, followed by the maximum frame size the PCD is able to receive. Its size is defined by the Frame Size for proximity coupling Device Integer (FSDI) value, from which the maximum Frame Size for proximity coupling Device (FSD) can be calculated by:

$$FSD = 2^{FSDI} \quad (3.1)$$

The maximum value for FSDI is 256 bytes, defined in [4]. The RATS command also includes the Card IDentifier (CID), which is a logical address used for the further communication. At the end a 2 byte CRC is added to protect the data.

The structure of the ATS can be seen in figure 3.10. The first byte defines the length of the ATS. The second byte contains the Frame Size for proximity Card Integer (FSCI), which is the equivalent to the FSDI for the opposite direction, as well as the indication whether the following optional bytes TA - TC are included.

The interface byte TA defines which data rates are supported and if the same data rate has to be used for both directions. The Start-up Frame Guard Time (SFGT) and the Frame Waiting Time (FWT) are given by the interface byte TB. The SFGT defines the minimum waiting time after the ATS has been sent, until the PICC is able to process new frames. The FWT defines the maximum time for the response of the PICC to a PCD command.

The last interface byte TC defines whether the use of CID and Node Address (NAD) is supported. The optional historical bytes  $T_1$  to  $T_k$  provide general information. For the RATS a 2 byte CRC is added at the end.

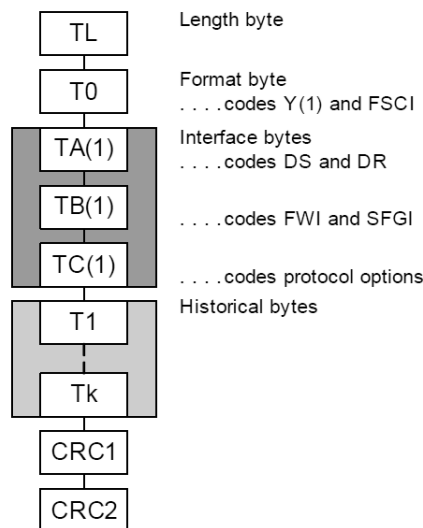


Figure 3.10: Structure of the ATS [4]

The data rate can be changed by using the PPS command, which furthermore contains the CID and the desired data rates, as given in the TB interface byte. Also the PPS command is protected with 2 bytes CRC.

### 3.3 ISO/IEC 14443 VHBR Amendments

In this section the amendments to the ISO/IEC 14443 standard for VHBR operation are given. The changes mainly affect part 2, in which the radio frequency power and the signal interface is defined. Changes in part 3 and 4 were also required to increase the maximum frame size, as well as to define the activation of VHBR.

#### 3.3.1 Radio Frequency Power and Signal Interface

As part 1 of the ISO/IEC 14443 [1] describes the general physical characteristics of a transponder, there were no changes necessary. Whereas part 2 [2] is of major importance for VHBR as it describes the radio frequency power and signal interface. In the amendment for part 2 [15] data rates up to 13,56 Mbit/s ( $f_c$ ) for the PCD to PICC and up to 6,78 Mbit/s ( $f_c/2$ ) for the PICC to PCD communication direction are defined. In the original standard [2] the subcarrier frequency is defined as  $f_c/16$ , this would mean that for data rates higher than 848 kbits/s the bit rate would be higher than the subcarrier frequency. Therefore the subcarrier frequency is increased for higher data rates as can be seen in table 3.2.

Subcarrier frequency	Bit Rate
$f_c/8$	1,695 Mbit/s
$f_c/4$	3,39 Mbit/s
$f_c/2$	6,78 Mbit/s

Table 3.2: Subcarrier frequencies for VHBR, PICC to PCD communication [15]

For the PCD to PICC communication data rates up to 848 kbit/s ( $f_c/16$ ) ASK, as defined in the existing standard [2], are used. For data rates above 848 kbit/s mPSK ranging from 2PSK to 16PSK can be used. Figure 3.11 shows the symbol constellations in the IQ-plane for the different mPSK types used. It can be seen that only a segment out of the full  $360^\circ$  is used.

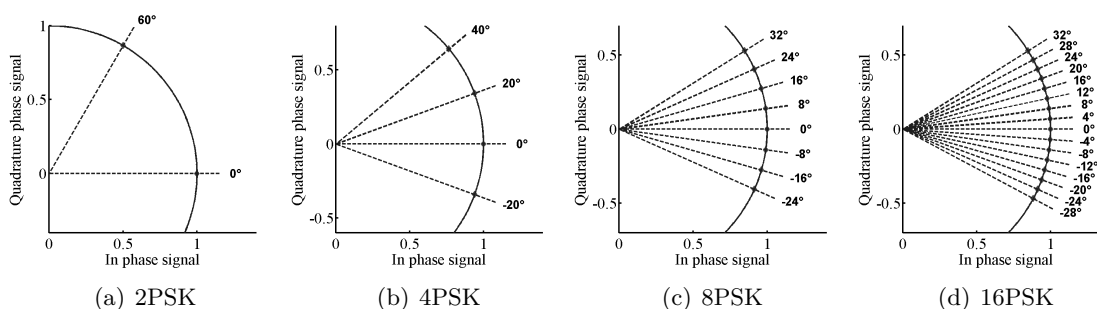


Figure 3.11: PSK symbol constellations for PCD to PICC communication [15]

The symbol duration, also called Elementary Time Unit (ETU), is also varied and ranges from  $2/f_c$  to  $16/f_c$ . This offers two degrees of freedom, which have to be restricted to a certain range. In table 3.3 all defined combinations of symbol durations and bits per symbol as well as the resulting data rate can be seen. The nomenclature for the different data rates is mPSKn, where m denotes the used modulation order and n represents the symbol duration as a fraction of one carrier period ( $\tau_c = \frac{1}{f_c}$ ).

Phase N Unitary $\Phi_{Seg}$	2PSK $2 = 2^1$ $\Phi_{Seg} = 60^\circ$	4PSK $4 = 2^2$ $\Phi_{Seg} = 60^\circ$	8PSK $8 = 2^3$ $\Phi_{Seg} = 56^\circ$	16PSK $16 = 2^4$ $\Phi_{Seg} = 60^\circ$
1 ETU = $16/f_c$ ( $\sim 1180$ ns)		4PSK16: $f_c/8$ ( $\sim 1,695$ Mbit/s)	8PSK16: $f_c/(16/3)$ ( $\sim 2,54$ Mbit/s)	16PSK16: $f_c/4$ ( $\sim 3,39$ Mbit/s)
1 ETU = $8/f_c$ ( $\sim 590$ ns)	2PSK8: $f_c/8$ ( $\sim 1,695$ Mbit/s)	4PSK8: $f_c/4$ ( $\sim 3,39$ Mbit/s)	8PSK8: $f_c/(8/3)$ ( $\sim 5,09$ Mbit/s)	16PSK8: $f_c/2$ ( $\sim 6,78$ Mbit/s)
1 ETU = $4/f_c$ ( $\sim 295$ ns)	2PSK4: $f_c/4$ ( $\sim 3,39$ Mbit/s)	4PSK4: $f_c/2$ ( $\sim 6,78$ Mbit/s)	8PSK4: $f_c/(4/3)$ ( $\sim 10,17$ Mbit/s)	
1 ETU = $2/f_c$ ( $\sim 147$ ns)	2PSK2: $f_c/2$ ( $\sim 6,78$ Mbit/s)	4PSK2: $f_c$ ( $\sim 13,56$ Mbit/s)		

Table 3.3: mPSKn bit rates for VHBR [15]

As for the ASK timing certain parameters are defined for the PSK. In figure 3.12 (a) the IQ plane including the definition for  $\Phi_{Seg}$  and  $\Phi_{SI}$  are plotted. Where  $\Phi_{Seg}$  is the segment used for the mPSK modulation.  $\Phi_{Seg}$  is defined as the angle between the two utmost constellation points. The symbol interval  $\Phi_{SI}$  is the angle between two adjacent symbol constellations.

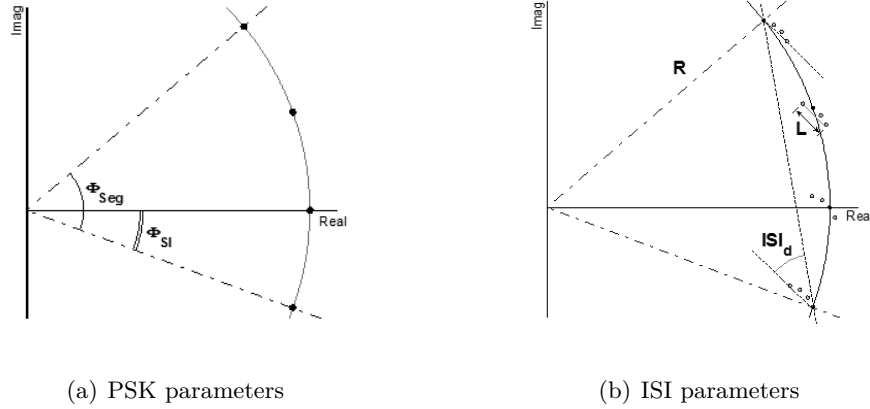


Figure 3.12: PSK and ISI parameter definition [15]

For 2PSK, 4PSK and 16PSK a IQ segment  $\Phi_{Seg}$  of  $60^\circ$  is used. Only 8PSK is an exception with a  $\Phi_{Seg}$  of  $56^\circ$ . A small  $\Phi_{Seg}$  of only  $60^\circ$  is chosen to keep the sideband level and the out of band emissions low. The symbol interval  $\Phi_{SI}$  is related to the used segment  $\Phi_{Seg}$  by the order  $m$  of the mPSK as given in the equation (3.2). This results in symbol intervals  $\Phi_{SI}$  ranging from  $4^\circ$  for 16PSK over  $8^\circ$  and  $20^\circ$  for 8PSK and 4PSK to a  $\Phi_{SI}$  of  $60^\circ$  for 2PSK.

$$\Phi_{SI} = \frac{\Phi_{Seg}}{m - 1} \quad (3.2)$$

For the PSK as well as the ASK the limits for the allowed deviation from the optimum are more stringent for the PCD than for the PICC. This is to ensure stable communication under all conditions. For higher data rates the symbol is not only distorted, but also ISI occurs, due to the band limited channel. The band limitation is generally caused by the reader antenna or by any other limitation such as the Electromagnetic Compatibility (EMC) filters, which are a necessary part of any reader antenna matching network. ISI is visible as the so called ISI cloud around the optimum constellation point. To characterize the influence of the ISI two measures were introduced. These measures are the ISI magnitude ( $ISI_m$ ) normalized by the symbol interval  $\Phi_{SI}$  and the ISI rotation ( $ISI_d$ ). In figure 3.12 (b) the definitions of the ISI measures in the IQ constellation diagram can be seen.

The ISI rotation ( $ISI_d$ ) can be observed directly, whereas the normalized ISI magnitude ( $ISI_m$ ) has to be calculated using the amplitude  $R$  of the modulation, the distance  $L$  between the two utmost points of the ISI cloud and the symbol interval  $\Phi_{SI}$ . The calculation of  $ISI_m$  is given in equation (3.3).

$$ISI_m = \frac{\arcsin\left(\frac{L}{R}\right)}{\Phi_{SI}} \quad (3.3)$$

To ensure interoperability between different PCDs and PICCs signals within the parameters given in table 3.4 have to be generated by the PCD. The ISI parameter limits for the signal, a PICC has to be able to receive, are larger than for the PCD in order to have some margin to ensure interoperability.

Parameter	PSK order m	Condition	Min	Max
$ISI_m$	2	-	0	0.50 (PCD); 0.52 (PICC)
	4,8,16	$abs(ISI_d) > ISI_{d,lim}$		
		$abs(ISI_d) \leq ISI_{d,lim}$	0	1.8 (PCD); 1.9 (PICC)
$ISI_{d,lim}$	2	-	N/A	N/A
	4, 8, 16	-	20° (PCD); 21° (PICC)	

Table 3.4: ISI limits for PCD and PICC [15]

In a real channel the signal is not only influenced by ISI, but also by noise. This noise results in phase noise when doing phase detection. To ensure that phase noise does not influence the proper symbol detection, limits with respect to the symbol interval  $\Phi_{SI}$  are defined. A PCD is not allowed to produce more Root Mean Square (RMS) phase noise than  $0.03 \cdot \Phi_{SI}$  and a PICC shall be able to receive signals with a maximum RMS phase noise of  $0.032 \cdot \Phi_{SI}$  [15].

In figure 3.13 all coding blocks involved in a VHBR transmission are plotted. Firstly the source data is fed into a gray decoder, so that all neighboring symbol constellations of an mPSK symbol differ only by one bit. Then the gray coded data passes the cumsum block, which performs differential encoding of the symbols. The data is mapped to the according PSK constellation and transferred over the channel. The channel consists of the proximity air interface in this case. At the receiver the input data is first processed by the PSK detector. Then the differential coding is removed and the gray coding is reverted. The final result is a replica of the input data.

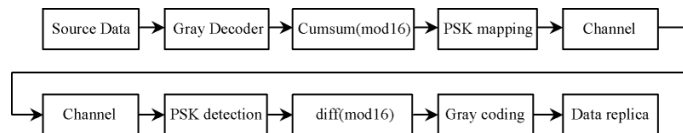


Figure 3.13: VHBR coding chain [15]

The Start Of Frame (SOF) for VHBR is defined as in table 3.5. The SOF consists of a calibration sequence (CAL) with a length of 44 ETU, a synchronization sequence (SYNC) of 4 ETU followed by a training sequence (TSC) for all modulation orders, except 2PSK.

CAL	SYNC	TSC
44 ETU	4 ETU	92 ETU

Table 3.5: SOF for VHBR [15]

### 3.3.2 Initialization and Anticollision

For very high data rates the use of larger frame sizes makes sense, especially due to the long prologue containing the calibration, synchronization and training sequence. Therefore the maximum frame size for the PCD to PICC as well as for the PICC to PCD communication is increased from 256 bytes to 4096 bytes. For type A this is done in the amendment to layer 4 [16] and for type B in the amendment to layer 3 [17]. The negotiation of the maximum frame size is done by the RATS and the ATS for type A in part 4 [4]. For type B this is done by the PICC selection command Type B (ATTRIB) and Answer to Request Type B (ATQB) command.

In this part of the standard also the framing and error detection using parities and CRC is defined. Analyzing the bandwidth efficiency of VHBR for smart cards, as done in [18], leads to the demand for a larger frame size, as well as for including error correction. A larger frame size was already introduced by [17] and [16]. The error correction is proposed in [19], by introducing a Hamming(63,57) coding for very high data rates. This offers the possibility to detect and remove one corrupted bit, as described in more detail in section 2.4.3. By making use of CRC calculated over the whole frame, a double error can also be detected, but not corrected. The choice for a Hamming(63,57) code was done considering an identical amount of overhead as if a parity would be used. Therefore the Hamming(63,57) code with 6 parity bits was chosen, resulting in an overhead of 10.53 %, which is close to the overhead of 12.5 % for a single parity after each byte [18].

### 3.3.3 Transmission Protocol

In this layer also the negotiation of data rates higher than  $f_c/16$  for type A is done. The negotiation is done by using the additional option to exchange parameters via S-blocks, as introduced by [20]. I-blocks are used beside S-blocks, to convey information used by the application layer. Whereas R-blocks are used for positive and negative acknowledgments. To negotiate the bit rate for VHBR 4 commands are available. The VHBR request command is used to check the support of VHBR. If VHBR is supported the VHBR indication command is used to get a list of supported PCD to PICC and PICC to PCD data rates. To activate one of the supported combinations of both data rates the VHBR activation command is used. The PICC then responds with an VHBR acknowledgment.

## 3.4 ISO/IEC 10373-6

The test standard ISO/IEC 10373-6 [13] describes the measurement methods for PCD and PICC devices according to ISO/IEC 14443 [1, 2, 3, 4]. This standard includes the definition of the test setup and also test cases. In this section only the test setup according to ISO/IEC 10373-6 [13] and the additional test cases defined in the amendment for VHBR [5] will be described.

In figure 3.14 the coaxial antenna arrangement can be seen. In the center the PCD antenna is situated, which emits the RF carrier by means of an alternating 13.56 MHz H-field. Commands for the PCD to PICC communication link are modulated on this RF carrier. The PCD antenna has a diameter of approximately 150 mm and consists of two windings. Also the matching network and the Q-factor are well defined [21] [22]. The PCD antenna is surrounded by two rectangularly shaped sense coils, which are used to sense the response from the PICC in a differential way. They are connected by twisted pair cables to keep unwanted induced voltage low. The output signal is set to zero for the unloaded PCD antenna. This is done by tuning the potentiometer, like shown in the

right part of the figure. Any detuning by the card and the load modulation is now clearly visible at the output, sensed by a probe connected to a oscilloscope.

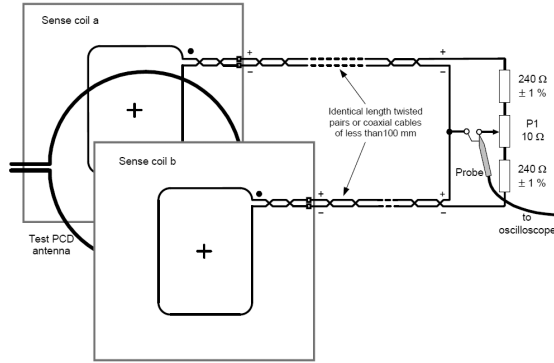


Figure 3.14: Coaxial antenna arrangement according to ISO/IEC 10373-6 [13]

On one side of the setup the Device Under Test (DUT) is placed and on the opposite side the calibration coil is located. The geometry of the coaxial arrangement can be seen in figure 3.15. The calibration coil is used to measure the H-field strength, as well as to evaluate the PCD signal applied to the PICC. The distances between the coils are well defined and can also be seen in figure 3.15. The PCD antenna and the sense coils are referred as active conductors as they are used during communication. All copper conductors of the antenna and the sense coils are located on the opposite side of the DUT.

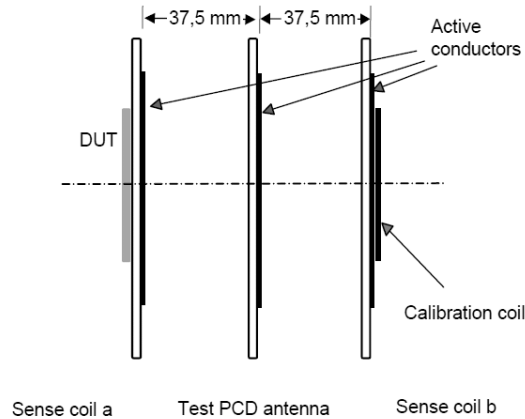


Figure 3.15: Antenna assembly profile [13]

For the lower data rates the timing parameters, as described in section 3.2.2 are of importance. It has to be tested whether the PICC is capable of demodulating any envelope shape that is within the specification. For the base data rate and higher data rates (up to 848 kbit/s) a set of envelope shapes with different timing and amplitude characteristics is used to verify the standard compliance of the PICC. A similar approach is made for VHBR, with the difference that for the proper symbol detection other parameters are of importance. These parameters have been described in section 3.3.1. This includes static parameters such as the used IQ segment  $\Phi_{Seg}$  and the resulting symbol interval  $\Phi_{SI}$  according to the modulation order. Dynamic parameters such as the ISI rotation and magnitude and the maximum acceptable amount of phase noise are also considered.

The measurement procedures are described in detail in [5]. The variation of  $\Phi_{Seg}$  and furthermore  $\Phi_{SI}$  can simply be accomplished by modifying the symbol mapping. The phase noise is digitally generated by adding a random sequence with the desired variation

to the sent data. Generating the ISI is however not as straightforward. One possibility is to tune the PCD to higher Q-factors and thus introduce ISI, which would mean that the PCD antenna and the matching circuitry has to be adjusted for each ISI constellation. Therefore it is preferable to introduce the band limitation and thus ISI by filtering the signal in the baseband, as proposed in [5].

In figure 3.16 both systems are visualized. In the left picture a real system without baseband filtering can be seen. It consists of the symbol source on the left followed by a Cartesian upconverter and the antenna resonator with a frequency response of  $H_{RF}$ . In the right picture the same transmit path including a baseband filter with the frequency response  $H_{bb}$  is shown. By modifying the transfer function of  $H_{bb}$  the behavior of the overall systems can be influenced in such a way that any antenna band pass system can be emulated. If the filter  $H_{bb}$  is digitally implemented it is rather easy to change its behavior. Thus enabling the easy generation of signals with a defined amount of ISI.

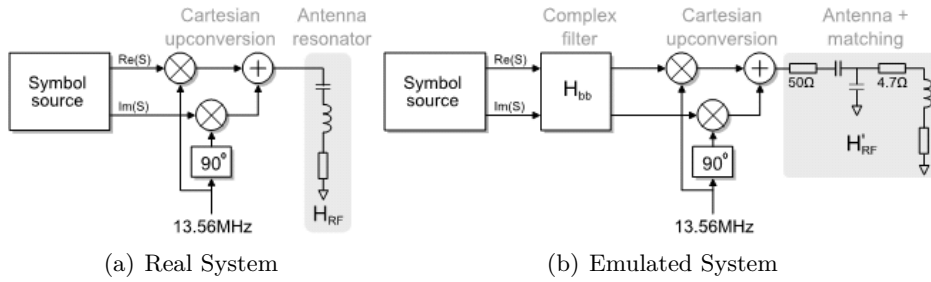


Figure 3.16: Antenna resonator modelling [5]

# 4. Measurement Instruments

This chapter is dedicated to comparing the different available instruments for signal generation and analysis.

## 4.1 Signal Generation

Two different instruments and their properties were analyzed. The first instrument is an Arbitrary Waveform Generator (AWG) from Tabor Electronics<sup>1</sup>. The AWG is capable of generating arbitrary patterns with a sample rate of up to 250 MS/s with a resolution of 16 bit [23]. The second instrument is the FPGA box, developed by NXP [21] and used for testing products that conform to the ISO/IEC 14443 standard. A picture of both instruments can be seen in figure 4.1.



Figure 4.1: Generators

The FPGA box is basically a reader with extended measurement functionality and the possibility to modify many parameters of the air interface layer, needed for contactless transponder system testing. The main part is a Field Programmable Gate Array (FPGA), that controls a Digital to Analog Converter (DAC) to generate the waveforms sent to the PICC. The FPGA box also includes two reader ICs to be able to analyze the inphase and quadrature channels in the receive path separately. One of this two readers also controls the data sent by the FPGA. The FPGA follows a predefined pattern according to the readers output. These patterns are calculated on the PC and loaded into the FPGA's memory.

The memory can hold 8 different patterns. The patterns 1 to 4 are dedicated to the standard data rates (106 to 848 kbit/s). The last pattern, called sequence 8, offers special functionalities. An arbitrary waveform with a duration of up to 2.3ms can be loaded into this memory. By using this sequence 8 any waveform calculated on the PC can be generated by the FPGA box. This method also offers the possibility to use a preequalizer to compensate the transfer function of the antenna. This is a very useful feature for the precise generation of waveforms with different timing parameters, as described in section 3.2.2. In the context of VHBR the preequalizer is vital to generate ISI free waveforms on the air interface using the resonant antenna and matching network, as defined in ISO/IEC 10373-6 [5].

---

<sup>1</sup>[www.taborelec.com](http://www.taborelec.com)

### 4.1.1 Performance

In order to determine the best suited instrument for the VHBR test-set up, measurements were performed with both mentioned signal generation devices. The results were then compared and evaluated. To exclude any influence of the antenna and the amplifier on the signal the generators were directly connected to the analyzer for the first measurements.

To generate PSK patterns with small symbol intervals  $\Phi_{SI}$  it is very important to have low phase noise. This is necessary in order to avoid an overlap of symbols in the constellation diagram due to such noise. The phase noise has two main origins, a white gaussian noise component and phase noise of any clock involved in the transmission and reception of the signal. Therefore the spectrum of the two generators is compared. In figure 4.2 the spectrum of the AWG (a) and the FPGA box (b) around the carrier of 13.56 MHz for a span of 4 MHz can be plotted.

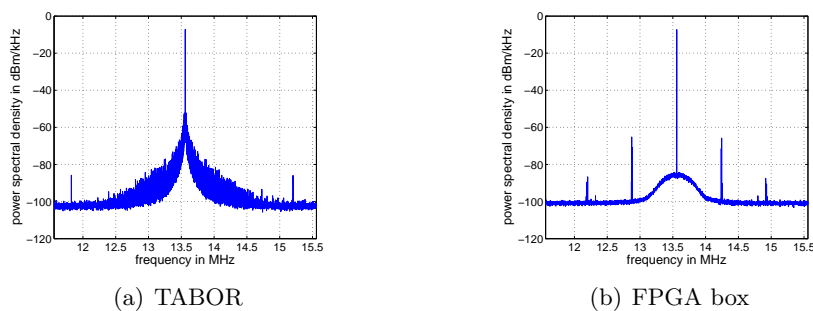


Figure 4.2: Spectrum of signal generators at a span of 4 MHz.

The output power of both signal generators was set to -7.2 dBm, which corresponds to the highest output power of the FPGA box. Both spectra were recorded using the same resolution bandwidth. The noise floor of the AWG is around -103 dBm for a resolution bandwidth of 1 kHz. Around the carrier the spectrum shows a very broad peak and as the noise floor increases in the vicinity of the carrier, it indicates mainly phase noise. This phase noise around the carrier consist of both, the phase noise of the signal analyzer and the generator.

The influence of the phase noise of the signal analyzer is described in section 4.2.1. The specification of the phase noise of the signal generator with respect to the carrier (dBc) of the AWG can be seen in table 4.1. The given values are with respect to 1 Hz resolution bandwidth. To recalculate the power spectral density to another resolution bandwidth equation 4.1 can be used [25]. Where  $\Delta PSD$  denotes the change of the power spectral density in dB when changing the effective noise bandwidth from  $B_{R,ZF1}$  to  $B_{R,ZF2}$ .

The effective noise bandwidth is the bandwidth of ideal rectangular filter in the frequency domain, through whom the same amount of white noise power passes than through the original filter. If the ratio between the effective noise bandwidth and the resolution bandwidth is the same for the old and the new settings also the values of the -3 dB bandwidths can be used.

$$\Delta PSD = 10 \cdot \log_{10} \left( \frac{B_{R,ZF2}}{B_{R,ZF1}} \right) \quad (4.1)$$

Since the spectrum is measured with 1 kHz resolution bandwidth, 30 dB have to be subtracted according to equation 4.1 from the measured values to get the corresponding values for 1 Hz resolution bandwidth. After this correction and also considering the additional noise due to the signal analyzer the measured spectrum is within the specification. The

noise floor of the FPGA box is around -101 dBm/kHz and shows a single sharp peak at the carrier frequency. Beside the phase noise around the carrier only a few spurious emissions are visible, but those do not contribute much to the overall noise energy, as they are only single peaks.

Frequency Offset	Phase Noise [dBc/Hz]	Phase Noise [dBc/kHz]
100 Hz	-70	-40
1 kHz	-85	-55
10 kHz	-92	-62
100 kHz	-112	-81
1 MHz	-140	-110

Table 4.1: Phase noise Tabor WW2572A [23]

To analyze the performance of the generators' mPSK<sub>n</sub> signals with frames including a calibration, synchronization and training sequence according to [17] followed by 256 random symbols were generated for both instruments. The signals were generated for the set of combinations given in table 3.3 in section 3.3.1. To be able to easily process the data automatically and to get additional information signals for 2PSK16, 8PSK2, 16PSK8 and 16PSK16 were also generated and analyzed.

In figure 4.3 the demodulated 2PSK8 frame of both generators is plotted. When taking a closer look to the signal of the AWG (a) it can be seen that the phase of a symbol does not remain constant during the frame. The phase of the AWG varies in the order of the smallest symbol interval  $\Phi_{SI}$  of  $4^\circ$  for the 16PSK<sub>n</sub> modulation scheme. This large deviation can cause severe problems when increasing the modulation order. The signal of the FPGA box (b) does not show this kind of behavior. The phase position of a symbol remains constant over the frame. This fact corresponds well to the spectra of both generators. The AWG shows a high amount of phase noise in its spectrum, which results in this large variation of the phase within a frame. Whereas the FPGA box does not show phase noise in its spectrum, nor does the phase constellation of a symbol vary within a frame.

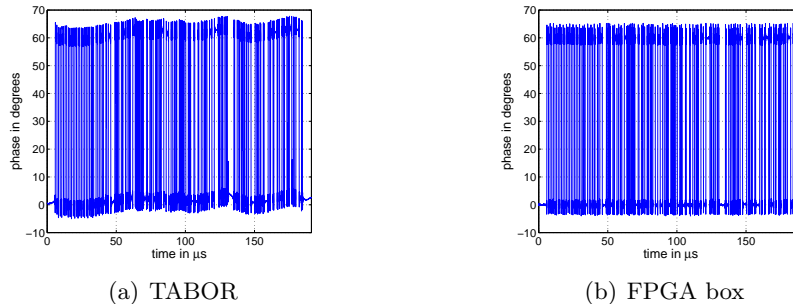


Figure 4.3: Generators 2PSK8 frame

#### 4.1.2 Conclusion

Both generators are able to generate the desired signals for all modulation orders  $m$  and symbol durations  $n$ . The AWG is capable of producing a larger output power, but on the other hand has a significantly higher phase noise. The FPGA box has a very clear spectrum and therefore also generates very stable signals with low noise. Also does the FPGA box support easy communication with the lower data rates defined in [2] and for the AWG also each frame for the standard data rates would have to be calculated accordingly. To ensure that no phase jump occurs between the beginning, respectively the end, of a frame and the plain carrier is not so easy for the AWG but already automatically done

in the FPGA box. The FPGA box also offers the possibility to use a preequalizer to compensate the antenna's transfer function. This is an important feature to generate test signals of more or less arbitrary shape. The lower output power of the FPGA box is not a limiting factor as the output can be easily amplified. Due to the better performance of the FPGA box regarding phase noise, standard data rates, the preequalizer and the fact that the FPGA box is already extensively used in the laboratory for other product compliance tests, the FPGA box was selected as the signal generator to be used. Therefore, all following measurements were performed, using the FPGA box.

## 4.2 Signal Analysis

Additionally to the generators a suitable analyzer had to be identified for the test set up. For the analysis of the signal, 3 different instruments were compared, two vector signal analyzers and one oscilloscope. For all tests of the analyzers the same frames as in section 4.1 were used. The first signal analyzer is a FSV 7 from Rohde&Schwarz with a frequency range of 9 kHz up to 7 GHz and a maximum analysis bandwidth of 40 MHz. The FSV also has the possibility to use the Vector Signal Analyzer (VSA) software option that is installed on the instrument.

The second analyzer is a MXA N9020 from Agilent with a frequency range of 20 Hz to 26.5 GHz. The MXA also offers a maximum analysis bandwidth of 40 MHz. When using the 40 MHz analysis bandwidth option an ADC with 12 bits resolution is used [26]. No information about the ADC resolution of the FSV could be found.

The third and last instrument is a WaveRunner 64Xi-A oscilloscope from LeCroy. It has a maximum analog input frequency of 600 MHz and a maximum sampling rate of 5 GS/s with a resolution of 8 bit. The oscilloscope offers an enhanced resolution mode that low pass filters the data to increase the amplitude resolution. A maximum of +3 bits is possible, but at tradeoff between oversampling and recording length has to be found as the memory is limited. For the measurements with a sampling frequency of 2.5 GS/s an enhanced resolution filter with +2 bits and a resulting cut-off frequency of 72.5 MHz was used. Figure 4.4 shows all three instruments.

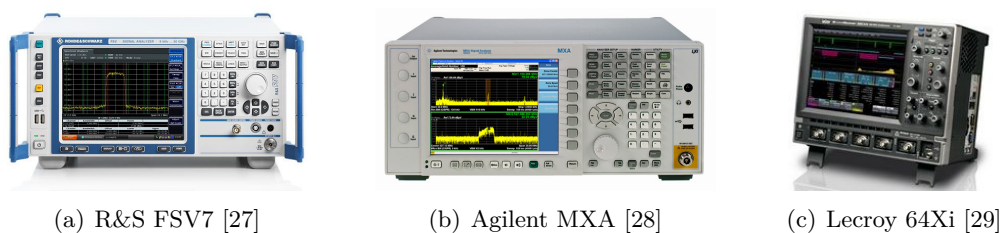


Figure 4.4: Analyzers

### 4.2.1 Phase Noise

As for the generators also for the analyzers the phase noise is an important measure. The Displayed Average Noise Level (DANL) of the R&S FSV7 is  $-152$  dBm/Hz ( $1$  MHz  $< f < 1$  GHz) [30] for a reference plane of  $-10$  dBm. With the same settings the Agilent MXA [26] has a DANL of  $-151$  dBm/Hz ( $10$  MHz to  $2.1$  GHz). For the oscilloscope a noise floor of  $-136.15$  dBm/Hz with a horizontal resolution of  $50$  mV/Div was measured [31]. When considering the 8 divisions of the oscilloscope and assuming a full scale sine wave as input signal the reference plane would be at  $-3.97$  dBm. This results in a dynamical range

of 132.19 dB for the oscilloscope and 142 dB respectively 141 dB for the analyzers for a resolution bandwidth of 1 Hz. So the DANL of the analyzers is around 10 dB better than the one of the oscilloscope.

Table 4.2 gives the phase noise specifications of the two analyzers. The values are for a carrier frequency of 500 MHz (R&S FSV7) and 1 GHz (Agilent MXA). For the LeCroy 64Xi no information about phase noise of the sampling clock could be found. But it can be assumed that it has excellent phase noise properties, such that the sampling clock jitter is not the main limitation for the effective resolution of the scope. The values given in table 4.2 are above the DANL so an increase of the phase noise around the carrier can be expected. This increase of the phase noise in the vicinity of the carrier is due the operational principle involving a Phase Locked Loop (PLL) to generate the Local Oscillator (LO) signal.

Frequency Offset	FSV Phase Noise [dBc/Hz]	MXA Phase Noise [dBc/Hz]
100 Hz	-84	-84
1 kHz	-101	-101
10 kHz	-106	-103
100 kHz	-115	-115
1 MHz	-134	-135
10 MHz	-150	-148

Table 4.2: Phase noise of the analyzers [30][26]

For all measurements an internal attenuator of 10 dB (0 dBm reference) was used. Taking this into account and recalculating the values for a resolution bandwidth of 1 kHz the DANL will be at -112 dBm, respectively -111 dBm. The measured noise floor of the FPGA box is at -100.85 dB for a resolution bandwidth of 1 kHz, which is around 10 dB above the noise floor of the instrument. So the measured signal mainly consists of the instrument's internal noise and the noise of the generator. The influence ( $\Delta MEAS$ ) of the DANL on the measured signal power  $S$  can be calculated with equation 4.2 [25].

$$\Delta MEAS = 10 \cdot \log_{10} \left( \frac{S + DANL}{S} \right) \quad (4.2)$$

The measurement of the noise floor of the FPGA box was done with the R&S FSV7 signal analyzer, so the measured signal is influenced by 0.35 dB which gives a corrected noise floor of the FPGA box of -101.2 dBm/kHz, respectively -131.2 dBm/Hz. The measured noise floor is by 0.43 dB for the MXA signal analyzer and already by 1.2 dB too high for the oscilloscope for the used settings. By setting the reference plane closer to the signals power the influence of the DANL on the measurement result can be reduced. On the other hand is setting the reference plane close to the signal power not very good, as the margin to the maximum input signal of the DAC is decreased and any spike in the signal may lead to saturation and furthermore distortion.

## 4.2.2 Signal Processing Chain

Signal analyzers and oscilloscopes have two different basic principles. A signal analyzer is designed to measure signals in the spectral domain in the GHz range. Therefore the input signal is mixed down or up and passes several Intermediate Frequency (IF) and amplifier stages before being at the final IF. This is necessary to cover the large frequency range of interest. At the final IF the signal is bandpass filtered and sampled. This sampling is usually not done in the first Nyquist band from 0 to  $f_s/2$ , but rather at higher input frequencies by using the aliasing properties of the sampling process. As long as the input signals bandwidth is not larger than  $f_s/2$  and the sample and hold is fast enough to capture the input signal, the input signal can be perfectly reconstructed. This technique is also often referred to as IF sampling.

In figure 4.5 the signal processing chain of the R&S FSV7 can be seen. The input RF signal is mixed with the LO in order to reach the IF. This is done in several stages, but for simplicity only one stage is drawn in the figure. After the mixer the signal passes an analogue band-pass filter with a bandwidth of 40 MHz. The signal is then sampled and all further processing is done in the digital domain. This includes the equalization of the transfer function of the analogue filter, in order to get an ideal frequency response, as well as the IQ-demodulation with the help of a Numerical Controlled Oscillator (NCO). After that stage the downconverted signal is low pass filtered and resampled to the desired sampling frequency. The data is then stored in the IQ memory for further processing and analysis.

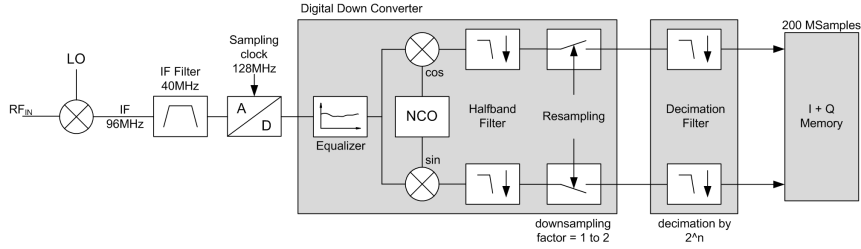


Figure 4.5: Signal processing chain FSV, modified [32]

An oscilloscope is not capable of operating in the higher GHz-range. Modern oscilloscopes are able to capture signals up to 1 GHz and more. Oscilloscopes simply sample and display the input signal. They have the disadvantage of the lower ADC resolution compared to signal analyzers, however they do offer a larger bandwidth. This drawback can be compensated to a certain extent by oversampling and low pass filtering the signal.

In figure 4.6 the signal processing chain of the oscilloscope including the postprocessing of the data in MATLAB<sup>2</sup> can be seen. The input signal passes an Anti Aliasing Filter (AAF) before being directly sampled without any mixing process involved. The sampled signal is then (optionally) low pass filtered on the oscilloscope in order to enhance the resolution.

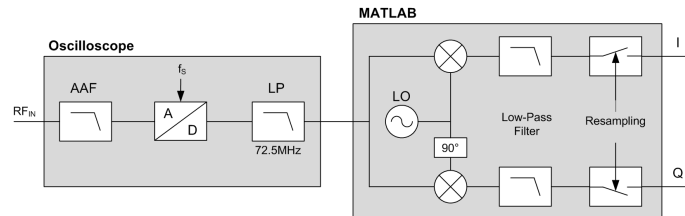


Figure 4.6: Signal processing chain oscilloscope

For the measurements done in this section this filter was set to 72.5 MHz, which resulted in 2 bits additional resolution. The two additional bits are gained by oversampling and low pass filtering the signal. The theoretical gain in resolution can be calculated by equation 4.3 [33][34]. Where  $\Delta Res$  denotes the gain in amplitude resolution in bits and  $OSR$  is the oversampling ratio with respect to the Nyquist frequency of the input signal.

$$\Delta Res = \frac{1}{2} \cdot \log_2(OSR) \quad (4.3)$$

The signal is furthermore transferred to the PC and postprocessed in MATLAB. At first the signal is IQ demodulated and low pass filtered. Finally the signal is downsampled to 500 MS/s and the final IQ samples are stored. Both instruments, the signal analyzer and the oscilloscope, do provide the same information at that stage.

<sup>2</sup>www.mathworks.com

### 4.2.3 Synchronization

Synchronization between the generator and the analyzer is important to demodulate the right signals. The signal generated is based on the oscillator in the generator, this signal is then analyzed with respect to the LO of the measurement device. As both oscillators have a limited accuracy the two frequencies are not exactly the same. There are two possibilities to synchronize the instruments. The first possibility is to use a PLL to either synchronize the generator with the analyzer or vice versa. The other possibility is to estimate the frequency error between the two clocks and to correct the difference numerically.

The FPGA box offers a reference frequency of 13.56 MHz, which is used to synchronize the analyzers. The FSV accepts a reference frequency from 1 to 20 MHz in 100 kHz steps [30]. As the provided reference does not lie on the required 100 kHz grid, the lock-in range of the PLL was extended to 40 kHz with the help of the R&S support using the analyzer's service mode. The MXA's external reference can reach from 1 MHz to 50 MHz with a locking range of  $\pm 678$  Hz for a reference frequency of 13.56 MHz [26]. Both instruments accept external frequency references differing to the 'standard' 10 MHz reference. The oscilloscope does not provide the possibility to synchronize to an external reference clock. Furthermore the phase at the analyzer is not known, even if the generator and the analyzer are synchronized. This is due to the propagation delay over the line and the different filters. Therefore also the phase has to be corrected at the receiver. In order to properly demodulate the signal, the symbol timing has to be determined as well. In figure 4.7 the corrections performed in MATLAB are plotted.

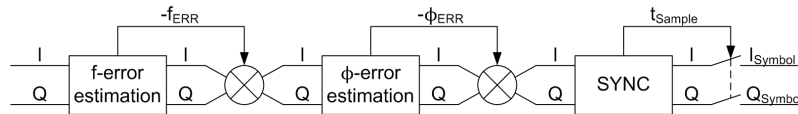


Figure 4.7: Synchronization chain MATLAB

In figure 4.8 a 2PSK8 signal containing 1 frame passing the correction chain is plotted. The input signal (a) shows a frequency and phase error. At first the frequency error is estimated. The differing frequencies of the generator and the analyzer result in a linear phase drift over time. Therefore the frequency error is determined by making a first order polynomial fit to the phase's time trace. The frame with the sent data is excluded, as it cannot be guaranteed that the signal is ISI-free and has therefore well defined states.

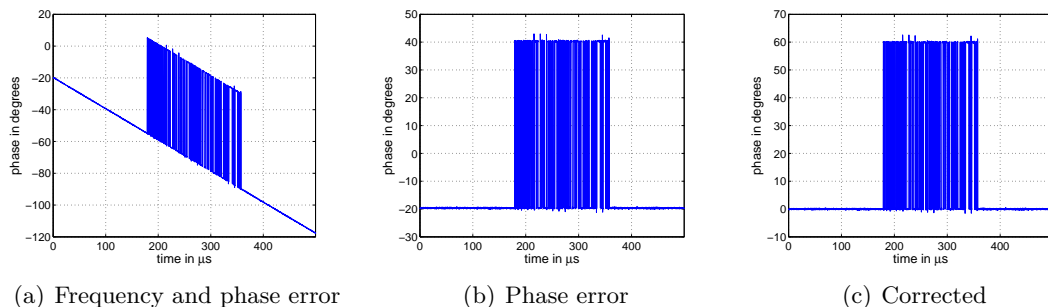


Figure 4.8: Frequency and phase error correction

The signal is then correct by the estimated frequency with the help of a complex mixer. In (b) the output of the frequency correction can be seen. The signal has still a phase error, that is estimated by taking the average phase before the frame. This principle is similar to locking the PLL of the receiver to the sent signal before receiving a frame. In

figure (c) the corrected frame is shown with the phase varying between  $0^\circ$  and  $60^\circ$ .

Both analyzers are able to synchronize on the 13.56 MHz reference signal without any influence on the phase noise. The results in free running mode using the frequency correction were as precise as the results with the analyzers clock locked to the generators clock. Therefore it can be concluded that locking the instruments is not necessary and does not bring any benefits. The oscilloscope does not offer the possibility to use an external clock, so the frequency error has to be corrected anyway.

#### 4.2.4 Analysis Bandwidth and Effects

The selection of the analysis bandwidth has a major influence on the measured signal. A large bandwidth means that the phase noise will increase, but on the other hand the measured signal is not distorted. A small bandwidth results in less phase noise, but heavily distorts the signal. As the signal present at the antenna is of interest the distortion caused in the measurement path has to be as low as possible. Therefore a large measurement bandwidth, including all the noise, is desirable to properly represent the signal at the air interface.

In figure 4.9 the IQ plot of the carrier for different sampling frequencies, respectively analysis bandwidth, can be seen. The measurements were performed on the FSV synchronized with the FPGA box. The MXA shows similar results.

In figure (a) a sample frequency of 13.56 MHz was used. The carrier visualizes as a single dot, that slightly varies due to noise. When increasing the sampling frequency to 25 MHz the noise increases and the displayed dot gets larger. By increasing the sampling frequency to 32 MHz the display significantly changes and is not a single dot anymore. Therefore it is not possible to assign the measured IQ-vector to any data point in the constellation diagram anymore.

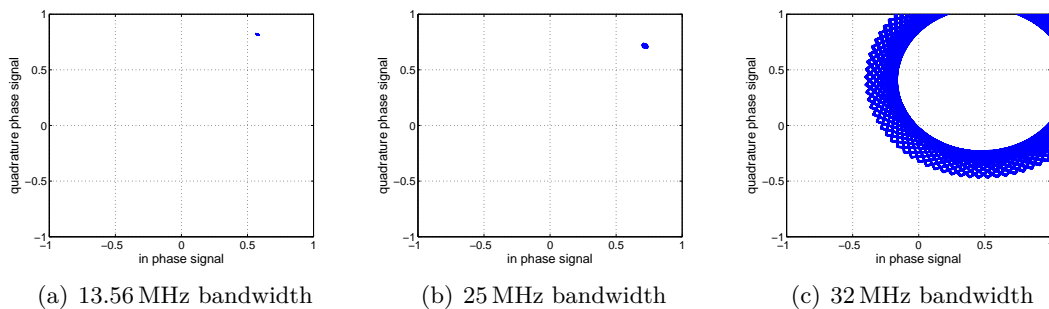


Figure 4.9: FSV sampling frequency IQ vector

This behavior is quite unexpected but can be understood when looking at the spectrum of the different measurements. Figure 4.10 shows the corresponding spectra to the IQ plots in figure 4.9. The spectrum for the sampling frequency of 13.56 MHz shows nothing extraordinary. The carrier at 13.56 MHz can be seen in the middle including the increased noise floor around the carrier due the PLL and some spurious emissions.

When looking at the spectrum recorded at 25 MHz sampling frequency a peak at 25 MHz can be observed. The root cause of this peak can be understood when analyzing the analyzers signal processing chain. The input signal is mixed several times to the final IF frequency. Each of these mixing processes includes a certain amount of LO feed through. This LO feed through then results in a DC-component of the signal, that is also the reason why signal analyzers do not work down until DC. The IF signal is then sampled and the DC signal occurs as an aliasing component at 25 MHz ( $26.06 \text{ MHz} - 1.06 \text{ MHz}$ ). This effect

becomes more visible when further increasing the sampling frequency to 32 MHz.

In figure (c) the corresponding spectrum including LO feed through at DC can be seen clearly. Also the first harmonic of the carrier is visible at 27.12 MHz. This two components cause the undesired behavior of the IQ vector.

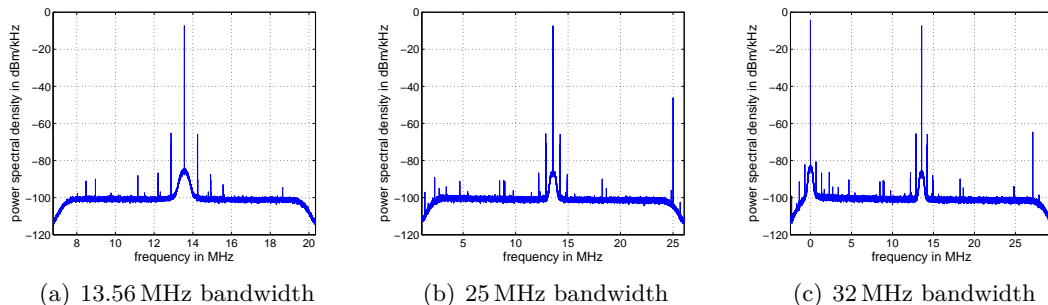


Figure 4.10: FSV sampling frequency spectrum

Therefore the analysis bandwidth of the signal analyzers is limited due to their operational principle. It was found that a sampling frequency of 20.34 MHz ( $1.5 \cdot f_c$ ) is a good trade off to avoid this problem and to still keep the analysis bandwidth as large as possible. The oscilloscope does not suffer from such problems as it works also at DC and the mixing process is performed in the digital domain under ideal conditions.

In figure 4.11 the effects of the band limitation in the receive path on a 16PSK8 signal can be seen for all instruments. The figures show the evolution of the phase in the time domain over 20 symbols including the end of the CAL sequence, the SYNC in the middle and the beginning of the training sequence. It appears that the signal recorded with the two analyzers (a) and (b) heavily suffer from ringing after and before each symbol transition. This is due to the band limitation in the receive path of the analyzers. The oscilloscope's larger analysis bandwidth has much less impact on the signal, as can be seen in (c).

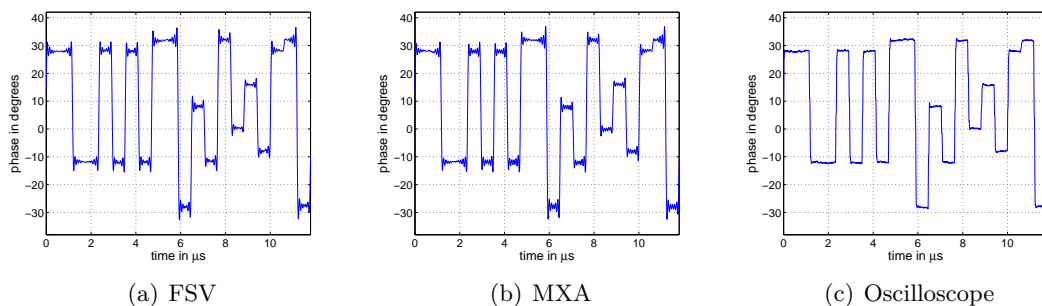


Figure 4.11: 16PSK8 demodulated signal

The negative effect of band limiting the signal can also be confirmed by running a simple simulation on MATLAB. In figure 4.12 the results of that simulation are plotted. For the analyzer a Finite Impulse Response (FIR) filter with a cut-off frequency of  $0.8 \cdot f_s$  using a Kaiser window was designed. The factor 0.8 is according to [32] and the same sampling frequency of 20.34 MHz ( $1.5 \cdot f_c$ ) as for the measurements was chosen. As the oscilloscope has a larger bandwidth the simulation was done with a sampling frequency of roughly 80 MHz ( $6 \cdot f_c$ ). For the oscilloscope a mean filter with a tap length equal to one carrier period was used.

Figure 4.12 (b) depicts the transfer functions of both filters. In figure 4.12 (a) and (c) the same frame as in figure 4.11 can be seen. The signal filtered with the low-pass filter is plotted in figure 4.12 (a) and shows similar ringing as the signals in figure 4.11 (a) and (b). The signal filtered with the mean filter is given in figure 4.12 (c), and clearly shows that it does not suffer from ringing at all.

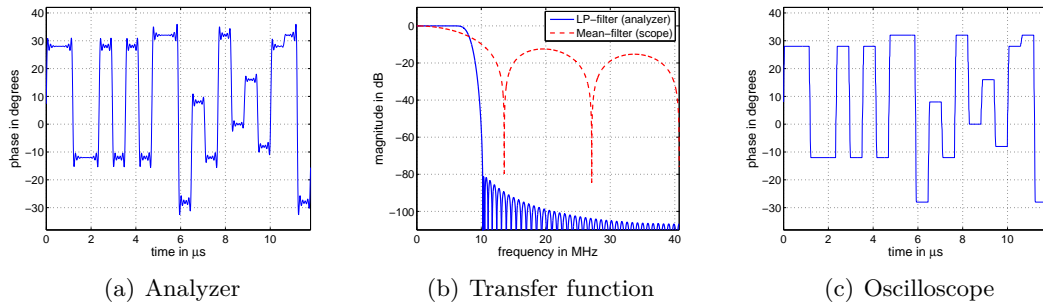


Figure 4.12: 16PSK8 simulated

### 4.2.5 Sampling Position Influence

Besides the right carrier frequency and the right phase the sampling position is very important for the proper demodulation of the signal. The determination of the right sampling position is done after the phase correction, as can be seen in figure 4.7. To determine the sampling position the received signal is aligned to the symbol grid. This is done by correlating the received signal with the sent data. After the alignment to the symbol grid the sampling position is set to the middle of the symbol duration. The middle of the symbol duration is chosen to give the signal time to settle and to still have some margin between the next edge of the signal.

In figure 4.13 the RMS phase error recorded with the oscilloscope is plotted in dependency of the sampling position. For a constant modulation order of 16PSK $n$  (a) it can be seen that the shorter the symbol duration gets, the longer the signal needs to settle with respect to symbol duration. The settlement time depends on the bandwidth and is independent of the symbol rate. By increasing the symbol duration by the factor of two the relative settlement time is as well decreased by the factor of two.

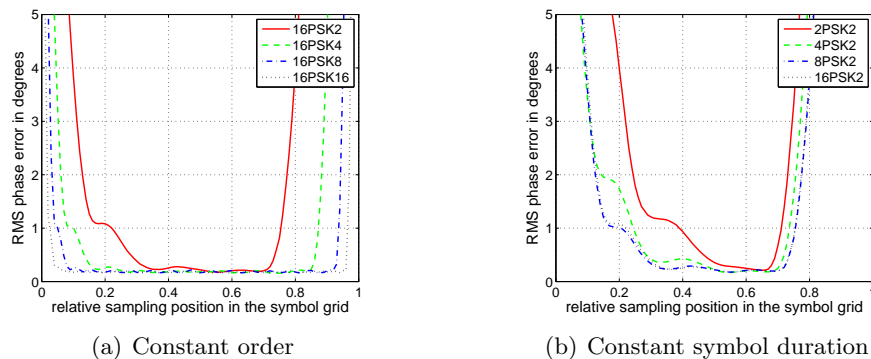


Figure 4.13: RMS phase error vs. relative symbol grid position, oscilloscope

In figure 4.13 (b) the same analysis is done for a constant symbol rate of mPSK2. The lower the modulation order is, the faster increases the RMS phase error and the closer

gets the sampling position to the beginning respectively the end of the symbol. For lower modulation orders the symbol interval is larger and the resulting average difference between two adjacent symbols is increased. Therefore the 2PSK2 signal shows the highest increase when deviating from the middle of the symbol duration. The RMS is only an average value for phase error and therefore gives no indication of a symbol error. A good indicator for symbol errors is the maximum phase error under the assumption that no equalization is done in the receiver.

Figure 4.14 shows the same plots for one signal analyzer as figure 4.13 does for the oscilloscope. The effect of the ringing can be seen quite well for the constant modulation order (a). The RMS phase error follows the shape of the ringing like in figure 4.11. The 16PSK2 signal shows the largest error as it suffers the most from the band limitation. For a constant symbol duration of mPSK2 (b) the phase error does not increase as much as for lower modulation orders shown in figure 4.13 (b). Generally speaking the average RMS error measured with the signal analyzer is significantly larger than the phase error measured with the oscilloscope.

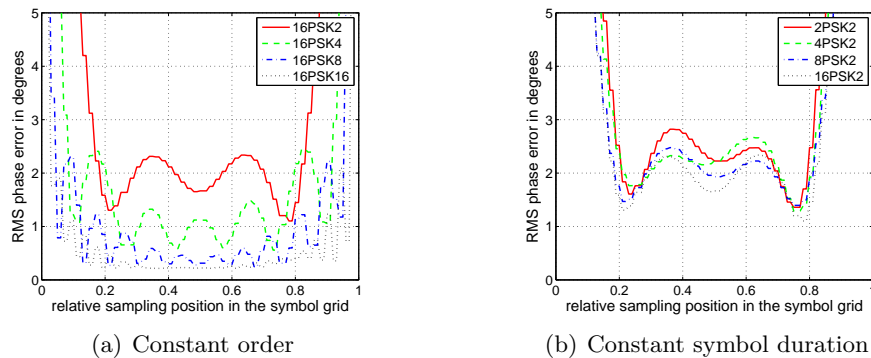


Figure 4.14: RMS phase error vs. relative symbol grid position, analyzer

## 4.2.6 Measurement Results

Overall 6 different methods to analyze the transmitted PSK signals were tested. This includes both analyzers in locked and free running mode, the VSA application of the FSV7 and the oscilloscope. The results for the analyzers with and without lock to the reference signal of the FPGA box did not differ significantly, therefore only one result is plotted for each of the analyzers.

In figure 4.15 the measured constellation diagrams for a 4PSK2 frame can be seen. The 4PSK2 signal is the signal with the highest data rate defined in [15] and was found to be the most critical for the analysis. The FSV7 (a) and the MXA (c) in combination with the MATLAB evaluation deliver with a phase error of  $2.3^\circ$  RMS and  $6.2^\circ$  maximum (16.28 MHz BW) identical results. The VSA application of the FSV7 delivers the worst results. It shows an RMS phase error of  $5.4^\circ$  and a maximum phase error of  $15^\circ$  (21.7 MHz BW). This is due to the fact that the minimum oversampling factor that can be set is 4. This results in a sampling rate of 27.12 MHz for the mPSK2 variants and the additional interference described in section 4.2.4.

Thus the performance of the VSA application is not very good for the highest symbol rate. For longer symbol durations (PSK4, PSK8 and PSK16) the results are comparable to those achieved with MATLAB. The oscilloscope (d) delivers the best results as it does not suffer from being band limited in the analysis path. This is also supported by RMS phase error of  $0.23^\circ$  and a maximum phase error of  $0.68^\circ$  (13.56 MHz BW).

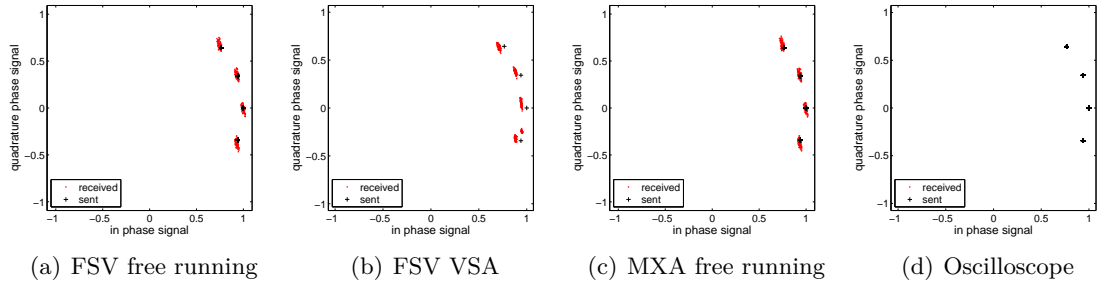


Figure 4.15: 4PSK2 constellation diagrams

The differences in figure 4.15 are even larger for a 16PSK2 signal as in figure 4.16. The 16PSK2 signal corresponds to a data rate of 27.12Mbits/s and is not defined in [15]. Therefore it is not of relevance. Nevertheless it shows very good the capabilities of the FPGA box and the oscilloscope (d) for the proper generation and analysis of this signal. The two analyzers (a) and (c) show a very large error and also show some symbol errors as the maximum phase error is larger than half of the symbol interval for both cases. The VSA application even completely fails to analyze the signal correctly due to the above described problems. Only the oscilloscope is capable to properly display the constellation diagram without introducing any distortion.

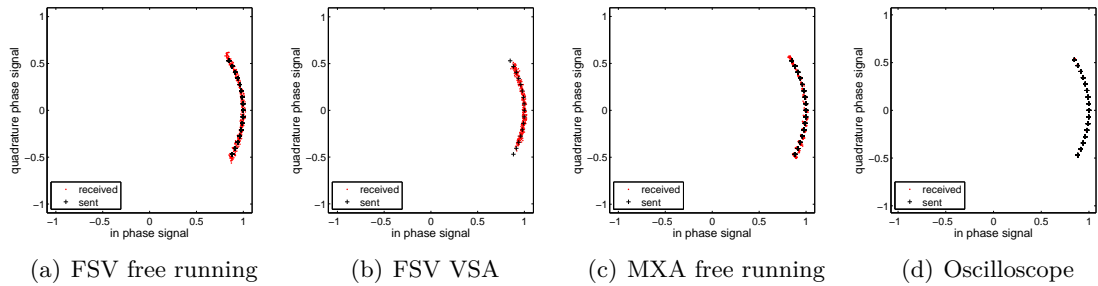


Figure 4.16: 16PSK2 constellation diagrams

In figure 4.17 the spectrum of the phase noise to the unmodulated carrier for all 3 instruments is given. The influence of the different filters used for demodulation can be seen. The phase noise floor of the two signal analyzers decreases rapidly above the cut-off frequency of their analysis filters at 8.14 MHz, whereas the phase noise floor measured with the oscilloscopes follows the transfer function of the mean filter. A spike at 672 kHz is due to spurious emissions of the signal generator.

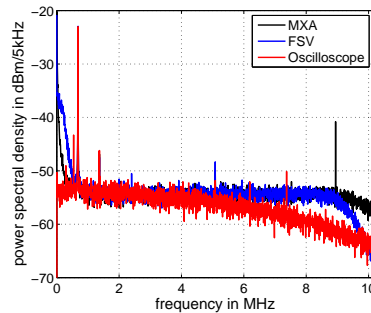


Figure 4.17: Phase noise spectrum of all instruments

The phase noise spectrum of the signal analyzers significantly increases towards zero. This is due to the phase noise of the LO, which is added to the signal during the mixing process [31]. The spectra correspond to a phase noise in the time domain of  $0.174^\circ$  RMS for the oscilloscope,  $0.231^\circ$  RMS for the FSV7 and  $0.259^\circ$  RMS for MXA. The phase noise of the analyzers is higher, as they use a larger analysis bandwidth.

The measured RMS phase errors for a 4PSK $n$  signal of different symbol duration are given in table 4.3. For all instruments it can be seen that the RMS phase error approaches the value of the RMS phase noise measured at the unmodulated carrier for the longest symbol duration of  $n = 16$ . But for shorter symbol durations the influence of ISI and ringing increases the RMS phase error significantly. The oscilloscope shows the best performance, as the RMS phase error is only slightly increased for the shortest symbol duration. Whereas the FSV VSA option shows the worst performance, as already pointed out above.

symbol duration n	FSV	FSV VSA	MXA	Oscilloscope
2	$2.287^\circ$	$5.36^\circ$	$2.258^\circ$	$0.231^\circ$
4	$1.177^\circ$	$0.94^\circ$	$1.219^\circ$	$0.176^\circ$
8	$0.290^\circ$	$0.39^\circ$	$0.435^\circ$	$0.160^\circ$
16	$0.227^\circ$	$0.24^\circ$	$0.214^\circ$	$0.173^\circ$

Table 4.3: RMS phase error 4PSK $n$  signal

#### 4.2.7 Final Considerations

A variety of instruments and different options have been tested in order to select the best method of analyzing the signal. The VSA option for the FSV7 signal analyzer is not suitable for the given task as the minimum useable oversampling is 4, which results in an analysis bandwidth that already includes the influence of the LO feedthrough at DC of the signal analyzer. Both signal analyzers in combination with MATLAB achieved similar results. But they suffer both from the LO feedthrough and the therefore limited bandwidth. The signal analyzers offer the possibility to synchronize to an external reference frequency, respectively the signal generator. It was found that estimating and correcting the frequency error has no impact on the measurement results and that therefore locking the clock of signal generator and signal analyzer is not necessary.

The noise floor of the measured signal is influenced less due to the better DANL of the signal analyzers, but the oscilloscope's DANL is not significantly worse. The oscilloscope achieves good measurement results using oversampling and postprocessing in MATLAB. As the signal processing chain of the oscilloscope does not involve any analogue mixing process it does not suffer from the LO feedthrough.

Also the whole signal processing chain can be influenced as this is not the case for the signal analyzers. The signals measured with the oscilloscope do not suffer from ringing as the signals measured with the signal analyzers do. The oscilloscope is capable of properly displaying the constellation diagram, where the signal analyzers already fail (16PSK2). Therefore, and due to the fact that the oscilloscope is already available at the existing test benches including a FPGA box in the laboratory, the oscilloscope was selected as measurement instrument. The possibility of using a higher analysis bandwidth for the signal analyzers and removing the LO-feed-through at DC by a notch filter was not tested and could be a possibility to improve the performance of the analyzers.

# 5. Test Setup

In this chapter the test setup will be described in detail. This includes a study of the influence of the antenna properties on the signal shape as well as the use of a preequalizer to compensate these effects. Additionally different methods to generate a test signal containing ISI with defined parameters will be discussed. Furthermore the measurement of the ISI parameters and the resulting challenges are described. Thereafter the system performance including generation and analysis is evaluated. Finally the chapter discusses methods for the generation and analysis of phase noise.

## 5.1 Transmission Channel

For the measurements performed the *NXP ISO test setup* is used. This setup basically consists of the FPGA box to generate arbitrarily shaped waveforms, a broadband amplifier [35], an antenna arrangement according to [13] and described in section 3.4 and an oscilloscope to capture and analyze signals. In figure 5.1 a picture of the test setup can be seen. The left-hand side shows the amplifier with the FPGA box on top. The RF output of the FPGA box is connected to the amplifiers input, whose output is then fed into the PCD1 antenna in the antenna tower. The antenna tower can be seen on the right-hand side of the picture and consists of 4 antennas, the PCD antenna with a Q-factor of 8, the two sense coils to detect the load modulation and the calibration coil to measure and verify the signal of the PCD antenna.

As the correct signal generation for the PCD to PICC link is of interest the calibration coil is used to verify the generated signal. The output of the calibration coil, as well as several other reference and trigger signals are connected to the oscilloscope, which can be seen in the center of the picture.



Figure 5.1: NXP ISO test setup

The FPGA box and the oscilloscope were already described in the previous chapter. The amplifier has a high cut-off frequency of 250 MHz and a maximum average output power of 75 W. Its gain can be digitally adjusted. The setting of the gain has nonlinear control characteristics. Therefore the FPGA box also contains a digital attenuator showing linear behavior. The field strength is usually set by using different amplifier settings to define the coarse range and by doing the fine regulation with the digital attenuator of the FPGA box.

### 5.1.1 Antenna Influence

The selection of the antenna has a major influence on the signal shaping. Except for the resonance frequency the Q-factor of the antenna is the main measure for the antenna's transfer function and furthermore for its influence on the signal. The resonant frequency is for PCD antennas usually tuned to the carrier frequency of 13.56 MHz. If the resonance frequency corresponds to the carrier frequency less input power is required to create the same field strength as if the antennas resonance and the carrier frequency are different. Therefore the analysis was only performed for this single resonant frequency. Also the antenna's impedance was tuned to  $50 \Omega$  at the carrier frequency of 13.56 MHz. In figure 5.2 the influence of different Q-factors of the PCD antenna on the signal shape can be seen. The figures show the phase of a 16PSK8 frame in the time domain.

Figure 5.2 (a) shows the signal distorted by a Q8-antenna. The signal transition follows an exponential shape and lasts approximately half a symbol duration. This means that for a mPSK4 frame the signal needs the whole symbol duration to reach the desired state and for a mPSK2 frame the signal would already need 2 symbol durations to fully reach the desired state. So a Q8 antenna already leads to a non negligible signal distortion and ISI.

In (b) the signal of a Q12 antenna is visualized. The signal shows overshoots that decay towards the end of the symbol duration. The signal is even more distorted than the signal with the Q8 antenna.

An even higher distortion shows the signal of the Q30 antenna shown in (c). The signal transitions already last more than two symbols and the signals do not settle to their desired position, which leads to large ISI. For shorter symbol durations the impact is even worse.

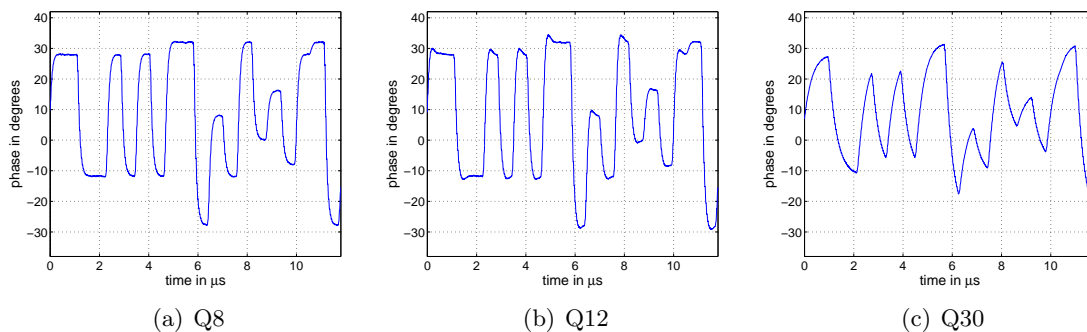


Figure 5.2: 16PSK8 time domain signal for different Q factors of antenna

It can be concluded that increasing the antenna Q-factor also increases signal distortion and consequently ISI. Depending on the Q-factor and the symbol duration the signal can also show overshoots. The Q8 antenna shows the best performance in terms of signal distortion, but mPSK2 signals are also already heavily distorted.

In general antennas with higher Q-factors are preferred as they do require less input power to achieve the same field strength. Thus a trade off between signal power and distortion has to be found. As a low output power is not of major importance for generating the test signals, the Q8-antenna with the lowest influence on the signal was chosen. All subsequent presented measurements were performed using a Q8-antenna.

### 5.1.2 Preequalizer

In order to compensate for the signal distortion due to the whole transmission chain including the antenna a preequalizer is used. A preequalizer is nothing else but an inverse filter of the channel for a maximal flat overall transfer function and for minimizing the signal distortions. The FPGA box used for the signal generation contains such a preequalizer, which is optimized for the standard data rates of up to 848 kbit/s. Nevertheless it can also be used for higher data rates.

The preequalizer is situated before the DAC and predistorts the signal in such a way that the signal at the air interface after the antenna has the desired shape. The coefficients of the inverse filter are determined based on a system model of the channel, which is derived from measurements. The main limiting factor for accuracy of the inverse filter is the determination of the channel model, which is one potential source of error.

But also the filter inversion may not deliver an exact solution if the zeros of the channel model are outside the unit-circle, which would then lead to poles outside the unit circle, resulting in instability [36]. In figure 5.3 (a) the transfer function of such a channel model of a Q8-antenna is plotted. The magnitude shows a peak at 13.56 MHz and decreases then for higher frequencies. The inverse of the channel model is plotted in (b). It shows exactly the inverse behavior of the channel model. The overall system (c) shows only a small attenuation for higher frequencies.

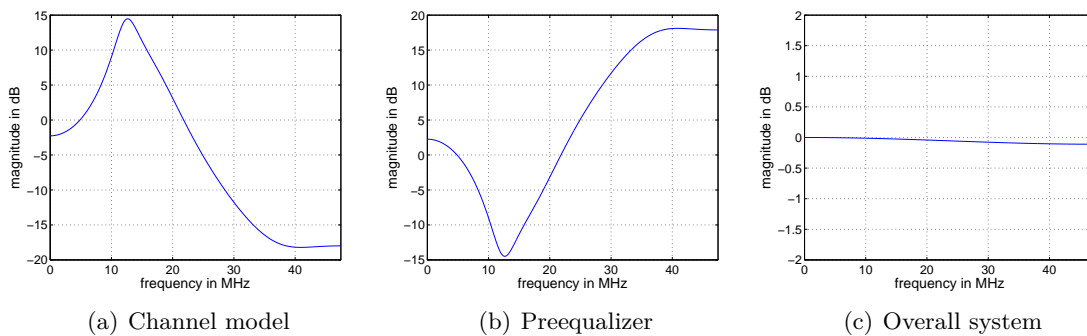


Figure 5.3: Preequalizer transfer functions

One problem that can occur when using a preequalizer is that the output signal after the inverse filter contains spikes in order to achieve very fast signal transitions. If these spikes get too high, exceeding the DAC range, the signal will be saturated leading to heavy signal distortion. In figure 5.4 (a) the output signal after the preequalizer is plotted, where an amplitude of  $\pm 1$  represents the DAC range.

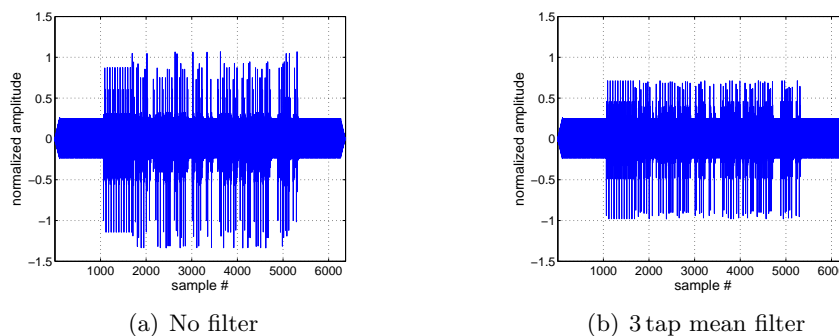


Figure 5.4: Signal after preequalizer

It can be observed that the signal contains large spikes exceeding the DAC range. In order to prevent this, the signal is filtered with a three tap mean filter reducing these spikes. The effect of this filter can be seen in figure 5.4 (b) where the spikes are within the DAC range.

In figure 5.5 the measured signals of an ideal 16PSK frame of different symbol durations transmitted over the antenna using a preequalizer are plotted. In figure 5.5 (a) the signal with the shortest symbol duration of 2 carrier periods is plotted. It can be seen that the signal transitions still last almost one symbol duration, but the desired state is reached. For longer symbol durations as depicted in figure 5.5 (b) (c) the relative transition time gets shorter and the signal shows a better quality. When comparing the signal of the 16PSK8 frame (c) using the preequalizer with the signal in figure 5.2 (a) it can be seen that the symbol transitions are much faster. The 16PSK16 signal is not plotted, but it shows even faster symbol transitions and is very close to an ideal rectangular signal.

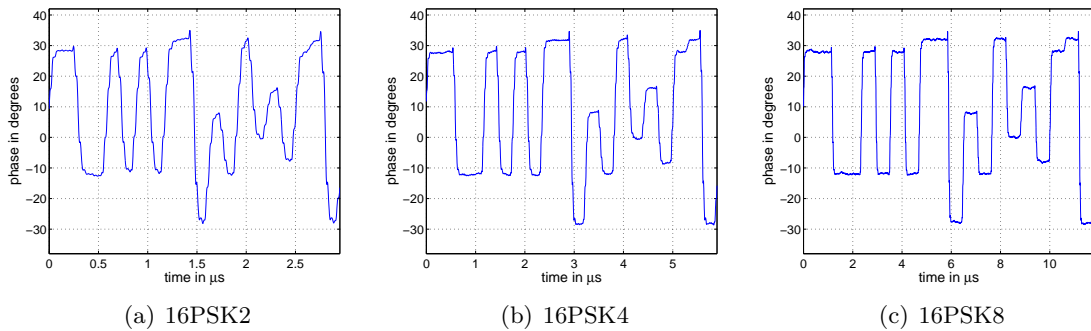


Figure 5.5: 16PSK $n$  time domain signals with preequalizer

## 5.2 ISI Generation

To generate ISI with the parameters ISI magnitude ( $ISI_m$ ) and ISI rotation ( $ISI_d$ ) defined in [15] and described in section 3.3.1 it is proposed by the test standard to use an IIR filter with one pole to emulate the base band equivalent system described in section 3.4. The transfer function of the base band filter in the z-domain can be seen in equation 5.1 [5]. The characteristic of this transfer function is parameterized by the complex pole  $p$  in the denominator. In the nominator  $p$  is used to normalize the baseband transfer function  $H_{bb}$ .

$$H_{bb} = \frac{(1 - p)}{1 - p \cdot z^{-1}} \quad (5.1)$$

The calculation of  $p$  was initially proposed to be done by equation 5.2 [5]. Where  $p$  is calculated in dependence of the two ISI parameters  $ISI_m$  and  $ISI_d$ . Also the symbol interval,  $\Phi_{SI}$  and the modulation segment  $\Phi_{SEG}$  influence the location of the pole.

$$p = \frac{\frac{1}{2} \cdot \sin (ISI_m \cdot \Phi_{SI}) \cdot e^{j \cdot ISI_d}}{\sin \left( \frac{1}{2} \cdot \Phi_{SEG} \right)} \quad (5.2)$$

The desired modulation signal is filtered by  $H_{bb}$ . Together with the pole calculated in equation 5.2 a signal at symbol rate  $f_{symbol}$  showing exactly the defined parameters is generated. As the output of the filter is running at symbol rate  $f_{symbol}$  and the signal has to be generated with the sampling rate  $f_{sample}$  the signal has to be upsampled. Upsampling

the signal such that it shows ideal rectangular pulses in the time domain would be the easiest way to generate the signal, but unfortunately does not reflect the physical reality. Using an exponential function as transition between two symbols comes close to reality but still does not emulate a real system. Modifying equation 5.2 by taking the symbol rate  $f_{symbol}$  and the sample rate  $f_{sample}$  into consideration yields equation 5.3 [5]. With this equation the pole location of a filter running at sample rate  $f_{sample}$  can be calculated.

$$p = \left( \frac{\frac{1}{2} \cdot \sin(ISI_m \cdot \Phi_{SI}) \cdot \exp^{j \cdot ISI_d}}{\sin\left(\frac{1}{2} \cdot \Phi_{SEG}\right)} \right)^{\frac{f_{symbol}}{f_{sample}}} \quad (5.3)$$

The filter  $H_{bb}$  is now fed with an ideal rectangular signal and the output signal shows ISI with the desired parameters.

In figure 5.6 (a) the output signal of the filter  $H_{bb}$  for a 16PSK8 frame with an  $ISI_m$  of 0.5 and an  $ISI_d$  of  $90^\circ$  can be seen. The continuous trace is the output of the filter running at sample rate  $f_{sample}$ , where the red square represents the output of the filter running at symbol rate  $f_{symbol}$ . It can be seen that the output of the filters corresponds to the last sample of one symbol.

Therefore the sampling of the signal for the analysis has to be done at the very end of one symbol. In figure 5.6 (b) different methods of interpolating between the desired ISI points at symbol rate  $f_{symbol}$  are shown. The output of the ISI filter at sample rate  $f_{sample}$  is plotted in blue. The green trace visualizes the signal generated by connecting the desired ISI constellation points at  $f_{symbol}$  with an exponential function. It can be seen that the signal looks quite similar to the signal generated by the output of the ISI filter running at  $f_{sample}$ . The red trace shows the result of upsampling the signal at symbol rate  $f_{symbol}$  using ideal rectangular pulses. It can be seen that generating such a waveform does not reflect the influence of a real antenna.

The difference between the exponential interpolated signal and the signal of the ISI filter at  $f_{sample}$  can be seen in (c), which shows the IQ-plane. The signal of the ISI filter (blue) at  $f_{sample}$  has an elliptical shape, whereas the exponential interpolated signal (green) moves on the direct link between the ISI constellation points at  $f_{symbol}$  (red). Consequently it is not possible to generate signals contag overshoots with the exponential interpolation method. Therefore the ISI filter working at the sample rate  $f_{sample}$  is chosen to generate the test signal.

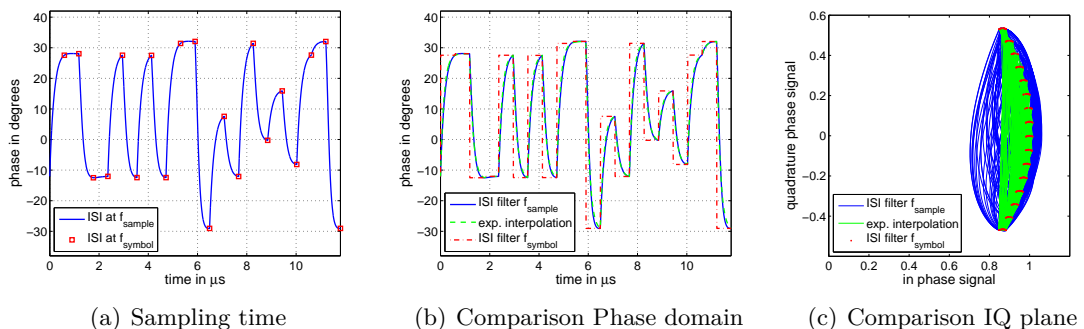


Figure 5.6: 16PSK8 ISI signals

## 5.3 ISI Analysis

In this section different algorithms for synchronizing to the received signal are analyzed. Also two different algorithms for analyzing the ISI parameters were investigated and their performance is presented.

### 5.3.1 Sampling Time Determination

It was found that the performance of the synchronization algorithm to determine the sample time is of utmost importance to measure the right ISI parameters. As visualized in figure 5.6 (a) the desired ISI parameters have to be measured at the very end of a symbol.

In figure 5.7 the influence of the sampling position on the constellation diagram of a 4PSK signal with an  $ISI_m$  of 0.5 and an  $ISI_d$  of  $90^\circ$  can be seen. In (a) the resulting constellation diagram for a sampling time at 60% of the symbol duration is visualized. The result of the sampling performed at 80% of the symbol duration is depicted in (b). Whereas (c) shows the desired constellation diagram showing the right ISI parameters at the very end of the symbol duration (100%). It can be seen that by sampling too early (a) and (b) the ISI cloud is larger and rotated, furthermore the measured parameters  $ISI_m$  and  $ISI_d$  will differ from the generated ones. Sampling too late (120%) has an even more severe effect on the measured ISI cloud, as can be seen in (d). It can be concluded that sampling at the end of the symbol duration is of utmost importance in order to measure the right parameters.

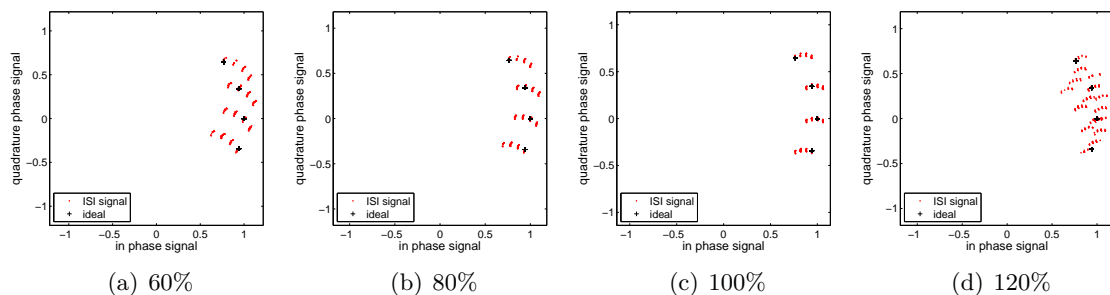


Figure 5.7: 4PSK ISI cloud in dependence of sampling position

In figure 4.13 the results of the algorithm based on the correlation with an ideal reference signal are plotted. It can be seen that the results of the synchronization are a more or less centered alignment of the received pulses to the symbol grid. The symbol transitions already take place before the end of the symbol duration depending on the data rate and the modulation order. Using this algorithm it is not possible to reliably sample at the very end of the symbol duration. Therefore the synchronization algorithm based on correlation used in chapter 4 had to be revised. Five different algorithms have been analyzed.

The first algorithm analyzed is proposed in [5] and based on maximizing the complex variance of the measured signal and will be denoted as max-var algorithm. A mathematical description of the algorithm is given by equation 5.4, where  $x_{MEAS}$  denotes the captured oversampled IQ signal at  $f_{sample}$  and  $T$  is the symbol duration with respect to  $f_{sample}$ . The symbol duration  $T$  is most likely a non integer number as  $f_{sample}$  is not a multiple of 13.56 MHz. This would result in non integer indices. This problem is solved by performing a nearest neighbor rounding for the calculated indices. In this context the variable  $n$  is a running index over all symbols and  $d$  is the delay. The optimum sampling instance is found by maximizing the variance with respect to the delay  $d$ .

$$\max_d (\text{var} (x_{MEAS}[n \cdot T + d])) \quad (5.4)$$

The results of this algorithm for different signals containing ISI and noise can be seen in figure 5.8. In (a) the determined sampling instance for an ideal signal with noise is visualized. It can be seen that the sampling does not take place at the end of the symbol due to the influence of the noise on the algorithm. In figure (b) the result for a signal with ISI showing exponential transitions is plotted. The algorithm properly determines the end of the symbol duration. But for a signal with overshoots the algorithm does not find the end of the symbol duration, it rather synchronizes to the overshoot as can be seen in (c). The end of the symbol duration can not be determined in this case and the measured ISI cloud will be wrong in this case. Therefore this algorithm is only well suited for exponentially shaped signals.

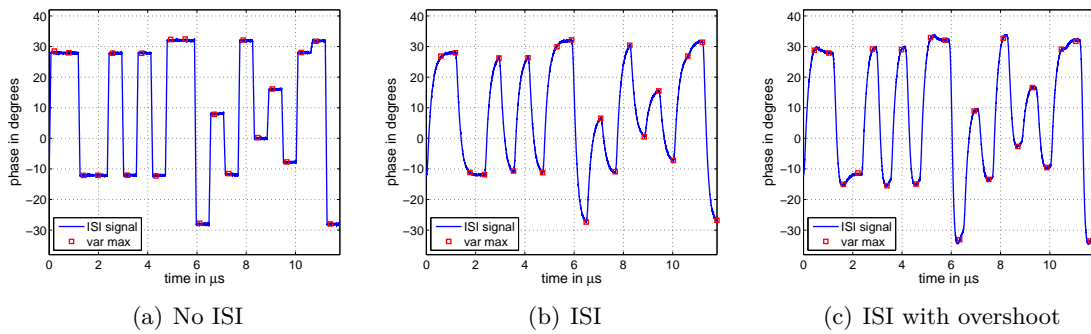


Figure 5.8: 16PSK8 frame with  $t_{sample}$  of max-var algorithm

The second algorithm is based on minimizing the RMS phase error with respect to the reference signal and will be referred to as the min-RMS algorithm. The mathematical description is given by equation 5.5. The ideal reference signal  $x_{REF,IDEAL}$  at symbol rate  $f_{symbol}$  in dependence of the index  $n$  is subtracted from the measured signal in order to build an error vector. The RMS value of this error vector in dependency of the delay  $d$  is then minimized in order to determine the best sampling time.

$$\min_d (RMS (x_{MEAS}[n \cdot T + d] - x_{REF,IDEAL}[n])) \quad (5.5)$$

The working principle of this algorithm is equivalent to determining the minimum in figure 4.13. The performance of this algorithm is similar to the max-var algorithm, except that the min-RMS algorithm is also capable of handling signals with overshoot. However the algorithm fails for signals with  $ISI_d$  values larger than  $90^\circ$ , as the minimum RMS error is more likely found during the symbol transition, when the signal is passing the ideal modulation angle, in this case. The min-RMS algorithm is influenced by noise and does not properly determine the sampling position for low ISI signals.

The third algorithm has already been used for the measurements in chapter 4 and is based on correlating the measured phase signal with the ideal reference phase signal. The corresponding formula is given in equation 5.6. By maximizing the correlation between the phase of the measured complex signal  $\angle(x_{MEAS}[n \cdot C + d])$  at  $f_{sample}$  and the phase of the reference signal  $\angle(x_{REF,IDEAL}[n])$  at  $f_{reference}$  the synchronization with the symbol grid is established.

The difference between the reference signal sampling frequency  $f_{reference}$  and the sampling frequency  $f_{sample}$  is corrected by the correction factor  $C$ . For the correction factor  $C$  the same principle as for the symbol duration  $T$  applies. Once the synchronization to the

symbol grid is established the sampling position can be set with respect to the symbol grid.

$$\max_d (\text{corr} (\angle(x_{MEAS}[n \cdot C + d]), \angle(x_{REF,IDEAL}[n]))) \quad (5.6)$$

This algorithm using the ideal reference signal synchronizes very well to the symbol grid for signals showing low ISI. If signals with very high ISI are generated the two signals differ too much, the symbols are not right aligned to the symbol grid anymore. It rather aligns the symbol pulses centered in the symbol grid. This makes it very difficult to sample at the very end of the symbol and therefore also does not qualify this algorithm.

To establish a better synchronization the next algorithm performs a complex correlation taking also the amplitude into account, as can be seen in equation 5.7. The algorithm uses a filtered version of the sent data as reference ( $x_{REF,FILT}[n]$ ). This includes the filter used for the ISI generation and the low-pass filters used to prevent the DAC from saturation and the filter used in the demodulator.

$$\max_d (\text{corr} (x_{MEAS}[n \cdot C + d], x_{REF,FILT}[n])) \quad (5.7)$$

Using the filtered version of the reference signal has the advantage that the received and the sent signal are quite similar and show therefore a very sharp correlation peak. It was found that this algorithm reliably determines the proper symbol grid and it is neither influenced by noise nor by the ISI shaping of the signal.

The result of the two correlation algorithms can be seen in figure 5.9. The algorithm using the ideal reference signal (a) finds the symbol grid with a delay of 17.86% with respect to the symbol grid in this particular case. Whereas the algorithm using the filtered reference signal perfectly aligns to the symbol grid.

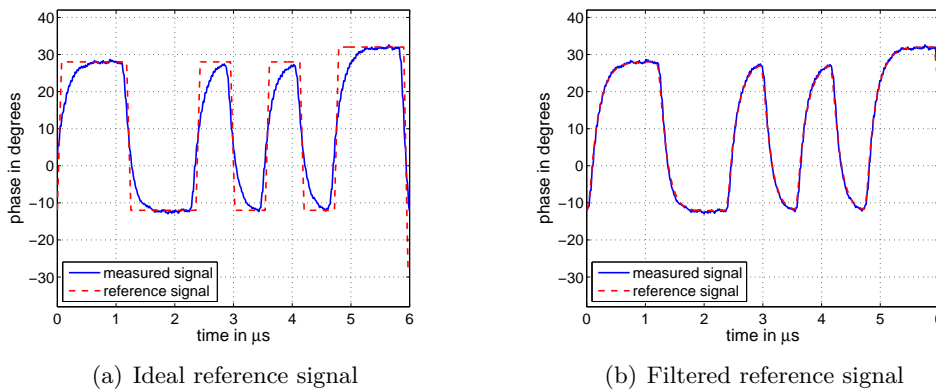


Figure 5.9: Correlation algorithms performance

The last algorithm considered is based on minimizing the absolute error signal of the lowest constellation point and will be referred to as the min-abs algorithm. The mathematical description is given in equation 5.8, where  $x_{MEAS}$  is the measured IQ and  $x_{REF,IDEAL}$  is the ideal reference IQ signal of the lowest constellation point only. The best sampling instance is determined by minimizing this equation with respect to the delay  $d$ . The algorithm delivers good results, but it is not able to determine the sampling instance as precisely as the correlation algorithm based on the filtered reference signal does.

$$\min_d \left( \text{abs} \left( \sum_{n=0}^{N-1} (x_{MEAS}[n \cdot C + d] - x_{REF,IDEAL}[n]) \right) \right) \quad (5.8)$$

Summing up, the first two algorithms fail due the influence of noise in some situations and the first algorithm is also not able to cope with signals containing overshoots. The correlation algorithm using an ideal reference signal also fails to reliably set the sampling time to the end of the symbol duration. Only the algorithm using the complex correlation with the filtered reference signal shows a good performance. The disadvantage of this algorithm is, that strong prior knowledge about the signal shape is required, which can not be provided when testing a reader with unknown properties.

However this algorithm is well suited for testing the proper generation of the test signals, as the filtered reference signal can be provided. Therefore this algorithm is selected to be used in all further measurements. For measurements of the ISI parameters of an unknown reader the min-abs algorithm is selected, as it also delivers good results and does not imply strong prior knowledge about the signal.

### 5.3.2 ISI Parameter Evaluation Algorithm

The final step in the analysis of the signal is the evaluation of the ISI parameters. Two different algorithms are evaluated. The first algorithm is based on graphically evaluating the ISI cloud of the lowest constellation point. This is done by determining the two outermost points of the ISI cloud [14] and calculating  $ISI_m$  according to equation 3.3. The ISI rotation  $ISI_d$  is determined by measuring the angle of the line between the two outermost points of the cloud and correcting it according to the overall rotation of the constellation diagram.

The second algorithm performs system identification on the transmission channel. In the case of the test system, this includes the filter generating the ISI as well as the actual transmission channel. The ISI parameters are calculated with the help of the determined filter coefficients [5].

In figure 5.10 the possible ISI parameter space is visualized. In (a) the ISI parameter space for the lowest constellation point of the 4PSK signal is plotted. In (b) the normalized ISI parameter space can be seen. Normalizing the ISI parameter space has the advantage of having the same display for all modulation orders as well as providing a better resolution. The rotation is corrected and the magnitude is normalized to the symbol interval  $\Phi_{SI}$ . The ISI parameter space for a 16PSK signal is in absolute values the smallest and visualized in (c).

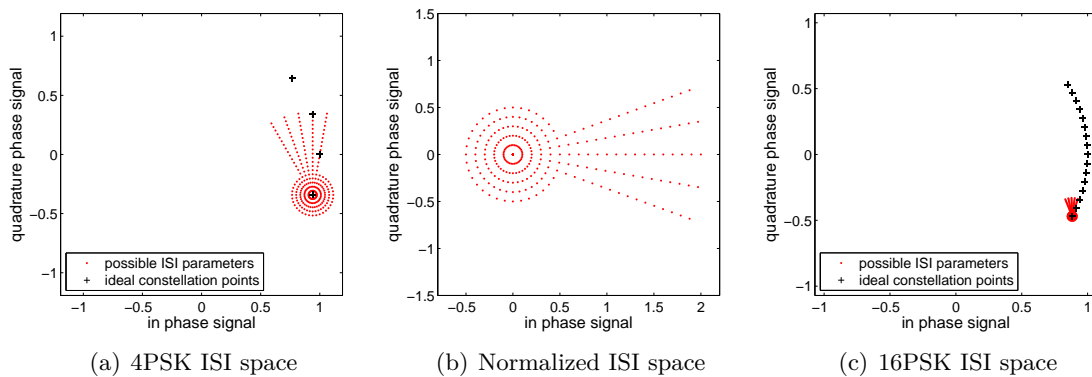


Figure 5.10: ISI parameter space

The operational range for this algorithms is limited by the range of possible  $ISI_m$  and  $ISI_d$  parameter combinations. The limits for  $ISI_m$  and  $ISI_d$  are defined in [15] and are given in table 3.4 and treated in section 3.3.1. For modulation orders higher than 2 the

values for  $ISI_m$  are limited to a maximum value of 0.50 (PCD) respectively 0.52 (PICC) if  $ISI_d$  is larger than  $\pm 20^\circ$  (PCD) respectively  $\pm 21^\circ$  (PICC). If  $ISI_d$  is smaller than these limits, the maximum value of  $ISI_m$  is limited to 1.8 (PCD) respectively 1.9 (PICC). For a modulation order of 2,  $ISI_m$  is limited to 0.50 (PCD) respectively 0.52 (PICC) for all conditions of  $ISI_d$ .

To test the ability of both algorithms to measure the correct ISI parameters a simulation under ideal conditions was performed. To exclude any influence of the channel or noise no modulation and demodulation has been performed. The output of the ISI filter  $H_{bb}$  operating at symbol rate  $f_{symbol}$ , described in section 5.2, for different ISI parameters was provided to the ISI parameter evaluation algorithms. Therefore an influence of the sampling time on the test result can be excluded.

Figure 5.11 depicts the results of this test, the blue dots are the ideal (set) parameters, whereas the red dots represent the determined (get) parameters. The results of the graphical evaluation algorithm are visualized in (a). It can be seen that the algorithm is not capable of determining the right parameters for  $ISI_d$  values larger than  $90^\circ$ . This results in a maximum error for  $ISI_d$  of  $9.65^\circ$ . Also for high  $ISI_m$  the results deviate with a maximum of 0.11 from the generated parameters. The summary of the results of the analysis of the algorithms can be seen in table 5.1.

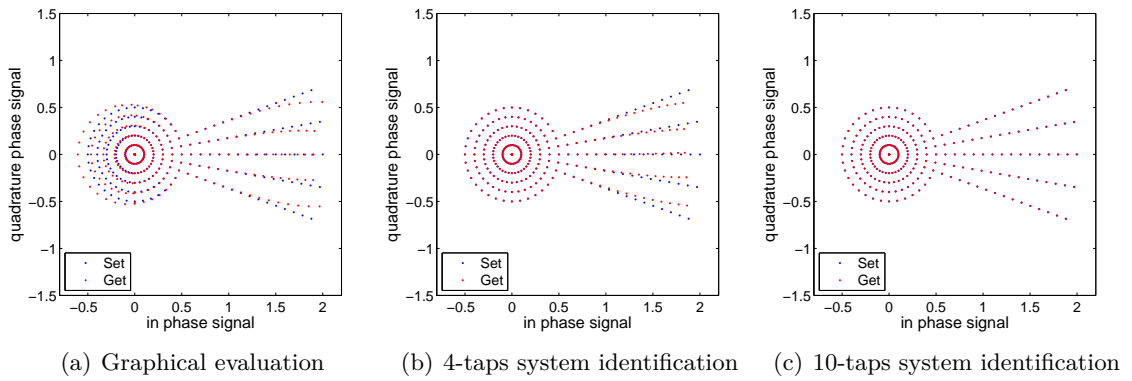


Figure 5.11: ISI evaluation algorithms performance 4PSK signal

In (b) the results of the system identification algorithm using a length of 4 taps can be seen. In the region of  $ISI_d$  around  $180^\circ$  the algorithm shows better performance than the graphical evaluation, but for very large values of  $ISI_m$  the algorithm shows similar errors. The RMS  $ISI_d$  error of  $0.7^\circ$  is lower than the RMS error of the graphical evaluation. With a maximum error of  $ISI_m$  of 0.16, the performance is again similar to the graphical evaluation. The results achieved with the system identification algorithm using 10 taps can be seen in (c). With a RMS  $ISI_d$  error of  $0.01^\circ$  and a maximum error of  $ISI_m$  of only 0.0048, this algorithm shows the best performance.

	Graphical		System identification		
			4-taps	10-taps	
Phase Noise	$0^\circ$	$0.25^\circ$	$0^\circ$	$0^\circ$	$0.25^\circ$
$ISI_m$ RMS	0.029	0.046	0.029	0.00066	0.0012
$ISI_m$ max	0.11	0.16	0.16	0.0048	0.0061
$ISI_d$ RMS	$2.55^\circ$	$3.85^\circ$	$0.70^\circ$	$0.11^\circ$	$0.18^\circ$
$ISI_d$ max	$9.65^\circ$	$15.4^\circ$	$3.75^\circ$	$0.01^\circ$	$0.73^\circ$

Table 5.1: ISI evaluation algorithms performance 4PSK signal

In a second step the graphical evaluation algorithm and the system identification algorithm using 10 filter taps were tested for their robustness under the influence of  $0.25^\circ$  RMS phase noise, which is approximately what can be expected under real conditions. For this experiment a frame containing the SOF as defined in [15] and 2048 random symbols was used.

In figure 5.12 the simulation results for the 4PSK signals are plotted. It can be seen that the graphical evaluation algorithm (a) is severely influenced by the noise as always the outermost constellation point is used and no averaging is performed. The error of  $ISI_m$  is relative high with a RMS value of 0.046 and a maximum error of 0.16. The performance for  $ISI_d$  is even worse, with a RMS error of  $3.85^\circ$  and a maximum of  $15.4^\circ$ . The algorithm based on system identification (b) shows a better performance with a RMS error of  $ISI_m$  of 0.0012 and a maximum of 0.0061. Also the error of  $ISI_d$  is with an RMS error of  $0.178^\circ$  and a maximum of  $0.73^\circ$  far below the error of the graphical evaluation algorithm. This is due to the fact that the system identification algorithm benefits from longer frames which result in an averaging of the noise components. For the 8PSK and the 16PSK signals the difference in performance of the two algorithms is even greater, as the noise with respect to the ISI space evaluated is larger.

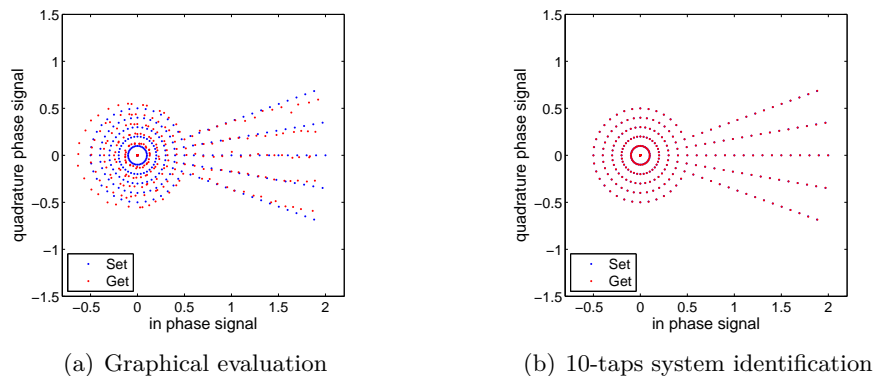


Figure 5.12: ISI evaluation algorithm 4PSK noise influence

In figure 5.13 a detailed analysis of the results presented above for  $ISI_m$  of 0.5 and  $ISI_d$  of  $90^\circ$  is visualized. The whole constellation diagram, including the ISI cloud (without noise) and the points considered for evaluation by the algorithms, is plotted in (b). An enlarged view of the lowest ISI cloud is depicted in (a). It can be seen that the two ISI points determined by the graphical evaluation and the system identification algorithm are at different locations.

The system identification algorithm exactly determines the set parameters of  $ISI_m$  and  $ISI_d$ , whereas the result of the graphical evaluation slightly differs with an  $ISI_m$  of 0.522 and an  $ISI_d$  of  $86.69^\circ$ . For other points within the ISI parameter space the difference can be even larger, as can be seen in figure 5.11. Therefore it can be concluded that the parameters cannot be evaluated by measuring the two outermost constellation points for all values of  $ISI_m$  and  $ISI_d$  even under ideal conditions.

In figure 5.13 the results of the measurement of the same ISI parameters under the influence of noise are plotted. The system identification algorithm is still able to deliver acceptable results with a value of 0.5007 for  $ISI_m$  and  $89.99^\circ$  for  $ISI_d$ . Whereas the graphical evaluation algorithm determines a value of 0.5456 for  $ISI_m$  and  $83.68^\circ$  for  $ISI_d$ .

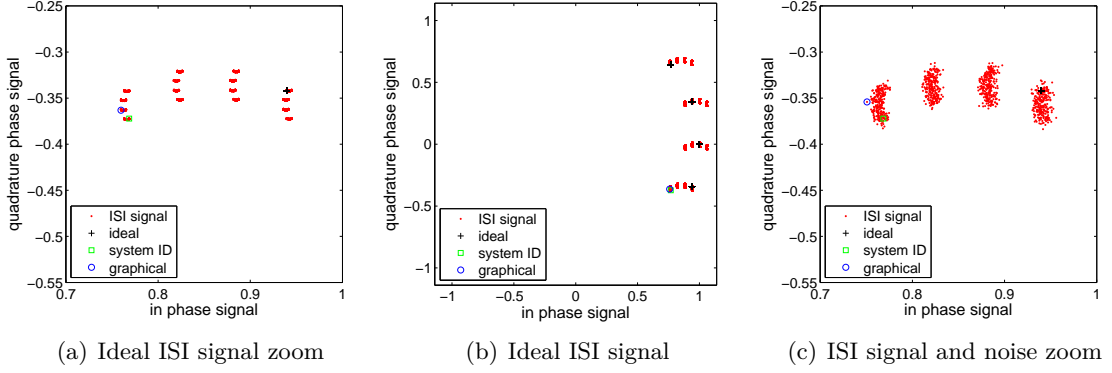


Figure 5.13: 4PSK ISI cloud evaluation points

The performance of the graphical evaluation algorithm under noisy conditions is not influenced by the length of the frame, whereas it does make a difference for the algorithm using system identification. The longer the frame is, the better the noise can be suppressed and the more accurate is the result. In figure 5.14 an analysis of the RMS error of  $ISI_m$  (a) and  $ISI_d$  (b) of the system identification algorithm using 10 taps under the influence of a RMS phase noise of  $0.25^\circ$  and for values of  $ISI_m$   $0.5$  and  $ISI_d$   $90^\circ$  in dependency of the number of symbols in the frame can be seen.

For longer frames the RMS error decreases as the influence of the noise is less due to an averaging during system identification. The frame length is limited in practice by the maximum payload size of 4096 kbyte, but with repeating the measurement and averaging the results the same accuracy as with longer frames can be achieved. The higher the modulation order, the higher the influence of the noise, as the noise with respect to the symbol interval  $\Phi_{SI}$  gets larger.

The detection error due to noise is more severe for the  $ISI_d$  than for the  $ISI_m$  parameter. For smaller values of  $ISI_m$  or larger phase noise the detection error increases. When decreasing  $ISI_m$  the proper measurement of  $ISI_d$  gets more difficult and the error significantly increases. But this is not a problem, as the measured values are within the allowed ISI parameter space and the accurate measurement of  $ISI_d$  and  $ISI_m$  is not so important in the region close to the ideal parameters.

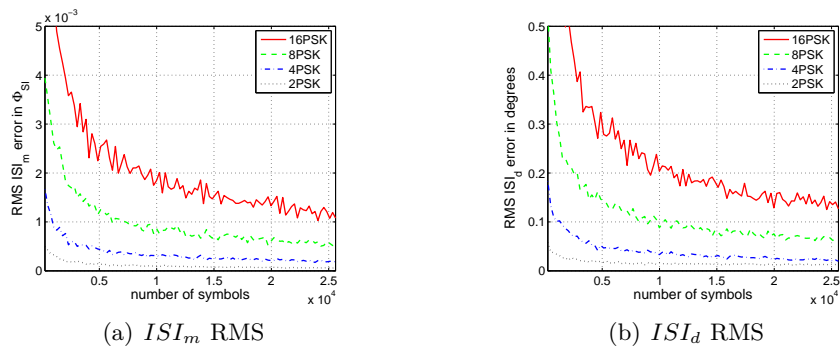


Figure 5.14: ISI parameter RMS error in dependence of frame length

Summing up, the system identification algorithm using 10 filter taps delivers better results and is less influenced by noise than the graphical evaluation algorithm. The graphical algorithm, as well as the system identification algorithm using 4 filter taps fail even under ideal conditions to measure the correct ISI parameters for some combinations of  $ISI_m$  and  $ISI_d$ . Therefore the system identification algorithm using 10 filter taps was selected for

the evaluation of the ISI parameters and all further analysis is done using this algorithm. The accuracy of the system identification algorithm can be enhanced by repeating the measurement and averaging the results.

## 5.4 Test System Performance

Up to now all components of the test system have been selected and their individual performance has been analyzed. In this section the performance of the whole measurement chain involving the ISI signal generation, the transmission over the channel using the FPGA box with the preequalizer and the analysis chain including the oscilloscope will be evaluated.

### 5.4.1 Channel and Demodulation Filter Influence

Measurements performed on the setup indicated that the ISI parameters set for the signal generation are distorted as the measured parameters differ for some situations significantly from the set ones. Therefore a simulation has been performed involving the signal generation and analysis including the mean filter used after the IQ demodulation. The modulation, transmission over the channel and demodulation have been excluded to determine the influence of the demodulation filter.

The results of the simulation for a 4PSK $n$  signal in the ISI parameter domain can be seen in figure 5.15. The values set for the ISI filter in the signal generation within the defined parameters space are visualized in blue. The values determined by the evaluation algorithm after the demodulation are visualized in red. It can be seen that the region of  $ISI_d$   $180^\circ$  cannot be reached by any settings of the ISI filter parameters, especially for shorter symbol durations (a). Also for large values of  $ISI_m$  around 2 and an  $ISI_d$  within the range of  $\pm 20^\circ$  the measured values deviate from the set ones.

For longer symbol durations the influence of the filters within the signal processing chain is reduced, as the occupied bandwidth is lower. The 4PSK16 (d) signal shows smallest errors due to the longest symbol duration. Using a higher bandwidth to reduce the influence of the filter is unfortunately no option as due to the low carrier frequency of 13.56 MHz the bandwidth until DC is a hard limit.

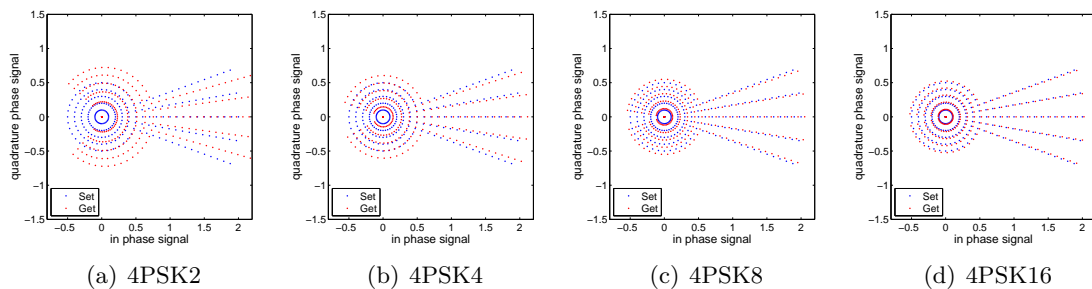


Figure 5.15: Demodulation filter influence on ISI parameters

In figure 5.16 a detailed analysis of the influence of the demodulation for a 4PSK2 signal with an  $ISI_m$  of 0.5 for two different values of  $ISI_d$  is performed. In (a) the original unfiltered ISI signal at the sampling rate  $f_{sample}$  with an  $ISI_d$  of  $90^\circ$  can be seen in the IQ plane. Additionally the signal sampled at the symbol rate  $f_{symbol}$  is plotted to visualize the shape of the ISI cloud. The same signal after passing the mean filter is plotted in (b).

It can be seen that the elliptical curve of the oversampled signal is slightly smaller and the ISI cloud is enlarged and rotated.

For the signal generated with an  $ISI_d$  of  $180^\circ$  the impact on the ISI parameter is even stronger. In (c) the desired ISI cloud as well as the oversampled signal are visualized. The effects of the filter on this signal can be seen in (d). As for the signal with an  $ISI_d$  of  $90^\circ$  the trace of the oversampled signal has changed and the elliptical curve of the signal is smaller. The resulting ISI cloud is significantly rotated and does not show the desired  $ISI_d$  value. This large difference between the set and the measured values can be explained by the short time duration over which the ideal signal remains at the desired position, which is then severely influenced by the mean filtering process.

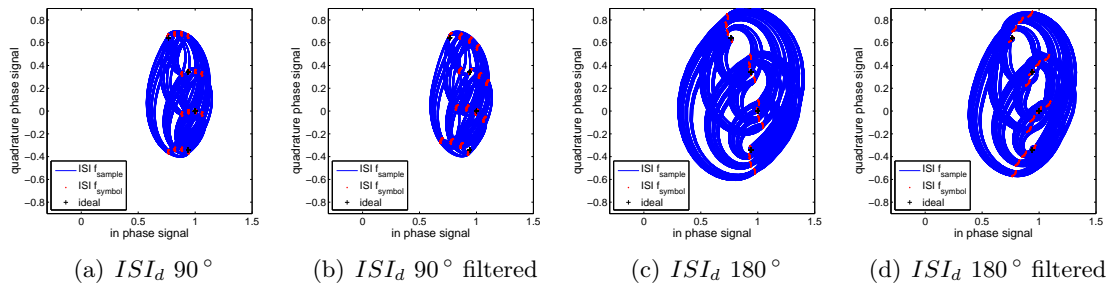


Figure 5.16: Demodulation filter influence 4PSK2  $ISI_m$  0.5

To solve this problem an optimization algorithm that iteratively changes the parameters of the filter in order to approach the desired parameters after demodulation has been developed. The  $ISI_m$  and  $ISI_d$  parameter of the filter are determined based on the according error signals. Based on this error signals and a multiplication factor smaller than one the two parameters are optimized independently. After reaching a desired accuracy or a total number of iterations the algorithm terminates. The algorithm is running the optimization procedure based on simulating the transmission over the channel including inverse filter and the channel model described in section 5.1.2.

The optimization procedure is done based on simulation due to a significant lower execution time. Generating the pattern and saving it, lasts about one second, downloading the pattern to the FPGA box takes up to 20 seconds depending on the frame length and symbol duration, furthermore storing and evaluating the oscilloscope's trace consumes another 8 seconds. This results in an overall time of up to 29 seconds for one iteration step. Assuming 10 iterations, this would already take five minutes to set the desired parameters for one test sequence only. Running the optimization procedure using the simulation can be done within two to three seconds. In figure 5.17 the initial conditions and the final results of this algorithm are presented. The algorithm was set to achieve an accuracy of 1% of  $ISI_m$  and  $0.5^\circ$  for  $ISI_d$ .

In (a) the initial conditions for a 4PSK2 signal can be seen. The measured values differ by far from the desired ones. The outcome of the optimization procedure can be seen in (b). It was found that the optimization algorithm works well for values of  $ISI_d$  within  $\pm 100^\circ$ , but fails to set the values outside this region. This can be easily understood as this region cannot be reached, as can be seen in figure 5.15.

In figure 5.17 (c) and (d) the initial conditions and the measured values of a 4PSK16 signal using the optimized parameters are visualized. It can be seen in (c) that the influence of the channel and the demodulation filter is significantly less for signals with longer symbol durations. The algorithm only fails in the vicinity of  $ISI_d$   $180^\circ$  and converges for a larger parameter space than for the 4PSK2 signal.

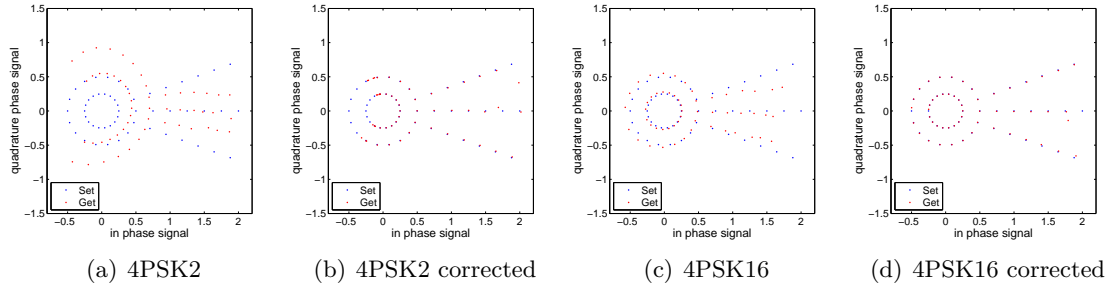


Figure 5.17: Initial and corrected parameters for a 4PSKn signal simulation

To verify the functionality of the algorithm the results of the simulation were cross checked with measurements. The measurement has been carried out for parameters of  $ISI_d$  lower than  $100^\circ$  and on a wider grid than the simulations were performed in order to reduce the measurement time. In figure 5.18 the results of the measurements with the corrected signals using the optimization algorithm are visualized. In (a) the measured parameters of a 4PSK2 signal using the initial (ideal) ISI parameters for the signal generation are plotted. It can be seen that the signal is distorted similar as for the simulation results presented in figure 5.15. The result of using the by simulation optimized parameters can be seen in figure 5.18 (b). The difference between the desired parameters and the measured parameters is even larger than when using the ideal filter coefficients. In (c) the measurement result for the initial conditions and in (d) for the optimized parameters of a 4PSK16 signal are plotted. No significant increase in accuracy can be observed.

It is assumed that the mismatch between the real channel and the channel model used as well as the influence of the reconstruction filter used in the FPGA box contribute to the difference of the simulation and the measurement. The optimization procedure based on simulation does not deliver satisfying measurement results. Performing the optimization procedure involving the real channel is due to the very long optimization time no practical option and can therefore not be used.

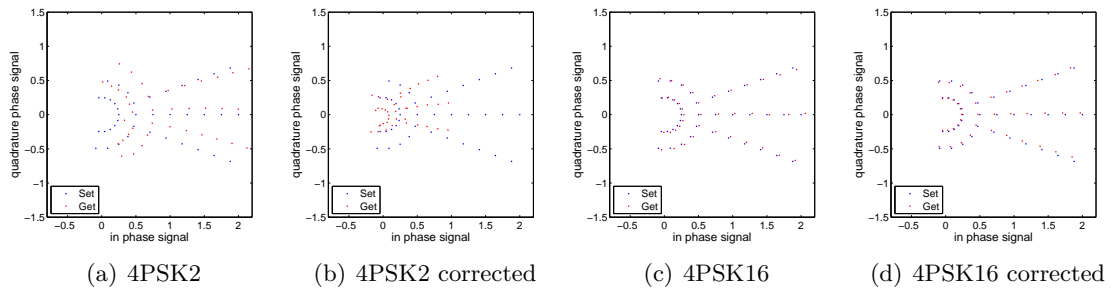


Figure 5.18: Initial and corrected parameters measured for a 4PSKn signal

To verify the proper functionality of the signal generation and analysis chain measurements, the ISI signals using the exponential interpolation method (described in section 5.2) have been performed. Figure 5.19 depicts the measurement results for 4PSK signals of different symbol durations. It can be seen that signals covering the whole parameter space can be generated and measured. The signal for the shortest symbol duration (a) shows small distortion. The accuracy of  $ISI_m$  shows with an RMS error of 0.053 and a maximum of 0.085 acceptable values. The performance of  $ISI_d$  is with an RMS error of  $6.1^\circ$  and a maximum of  $16.47^\circ$  not as good as the performance of  $ISI_m$ .

Generally speaking, the accuracy of  $ISI_m$  is not a problem for all symbol durations. But the achieved measurement accuracy of  $ISI_d$  strongly depends on the symbol duration. The longer the symbol duration is, the more accurate results are achieved. The  $ISI_d$  parameters have an RMS error of  $2.29^\circ$  ( $7.33^\circ$  max.) for 4PSK4,  $0.67^\circ$  ( $1.66^\circ$  max.) for 4PSK8 and  $0.61^\circ$  ( $1.82^\circ$  max.) for 4PSK16.

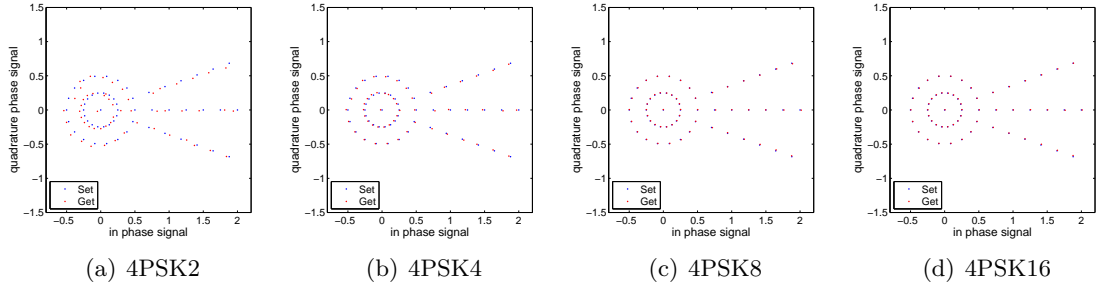


Figure 5.19: Measured ISI parameters using exponential interpolation method

The measurements have been performed with an payload of 2048 symbols. A RMS phase noise of  $0.32^\circ$  was measured. Keeping the slightly increased measured phase noise in mind, the resulting accuracy corresponds well to the results of the simulation of the influence of noise in section 5.3.2. Repeating the measurement would reduce the variance of the measured parameters, but it has been proven that signals within the required ISI parameters combination can be generated and analyzed based on the exponential interpolation method. Whereas the signal generation based on the ISI filter running at sample rate is not capable of covering the whole parameter space and the measured values differ from the desired ones.

## 5.5 Phase Noise

The phase noise of the signal is the third parameter to characterize the signal quality. Generally, the lower the phase noise contribution to the signal, the better the receiver can detect the right phase states. Therefore limits for the RMS phase noise with respect to the symbol interval  $\Phi_{SI}$  are defined in the standard. These limits are defined as  $0.03 \cdot \Phi_{SI}$  for the PCD and  $0.032 \cdot \Phi_{SI}$  for the PICC [15].

### 5.5.1 Noise Measurement

For the measurement of the phase noise four methods have been evaluated. The first method is measuring the phase noise on the unmodulated carrier, as done in section 4.2.1. The RMS phase noise is calculated by using equation 5.9. Where  $\Phi_{ERRRMS}$  is the RMS phase error,  $N$  is the number of samples and  $n$  is the index used for summation,  $\Phi_M$  is the measured and  $\Phi_{REF}$  is the reference phase signal.

$$\Phi_{ERRRMS} = \sqrt{\frac{1}{N} \sum_{n=0}^{N-1} (\Phi_M[n] - \Phi_{REF}[n])^2} \quad (5.9)$$

When evaluating the unmodulated carrier the reference signal  $\Phi_{REF}$  is set to zero. The measured phase error corresponds to the phase noise of the carrier for the unmodulated carrier, as not other components such as ISI contribute to the phase error.

The second possibility is to evaluate the phase noise in a differential manner, as suggested by [5], in order to consider the differential coding. The corresponding equation for the differential calculation is given in equation 5.10.

$$\Phi_{ERRRMS,D} = \sqrt{\frac{1}{N-1} \sum_{n=1}^{N-1} (\Phi_M[n] - \Phi_{REF}[n] - (\Phi_M[n-1] - \Phi_{REF}[n-1]))^2} \quad (5.10)$$

When measuring the unmodulated carrier the reference signal is always zero and equation 5.10 simplifies to

$$\Phi_{ERRRMS,D} = \sqrt{\frac{1}{N-1} \sum_{n=1}^{N-1} (\Phi_M[n] - \Phi_M[n-1])^2}. \quad (5.11)$$

For the evaluation of the phase noise the signal is sampled at the symbol rate  $f_{symbol}$  in order to measure the noise for each symbol. Under the assumption of independent and identically distributed (iid) zero mean white noise the differential evaluation according to equation 5.11 of the samples delivers an RMS value, which is by the factor of  $\sqrt{2}$  higher than the RMS value evaluated normally according to equation 5.9. Calculating the difference between two noise samples in this case is equal to subtracting two iid zero mean noise signals with the same variance from each other, which results in a signal with twice the variance of the original signal. Measurements have shown that the factor between the two different methods is slightly below the theoretical value, especially for shorter symbol durations. Therefore it can be concluded that the phase error is not completely iid white noise or has a residual mean component. The noise not being iid can be easily explained by the antennas transfer function, which influences the spectral shaping of the noise. And this shaping is not compensated by the preequalizer. Evaluating the noise differential is therefore depending on the symbol duration and the antennas influence on the spectral shaping of the noise to some extent.

The third possibility is to evaluate the noise within the frame. This implies the proper generation of the reference signal  $\Phi_{REF}$ . If the ideal signal is used as the reference signal, as done for the measurements presented in section 4.2.5, the phase error signal ( $\Phi_M - \Phi_{REF}$ ) also contains the influence of ISI. The larger the ISI, the more the RMS phase error will be increased. To exclude the this influence, the reference signal is calculated based on the channel model. The channel model derived by the system identification for the measurement of the ISI parameters is used for that purpose. The calculation of the reference signal is given in equation 5.12, which describes the convolution of the complex ideal reference signal  $x_{REF IDEAL}$  with the impulse response  $h$  derived from the system identification. The phase reference signal  $\Phi_{REF}$  is the argument of the result of the convolution.

$$\Phi_{REF}[n] = \angle \left( \sum_{k=0}^{M-1} (h^*[k] \cdot x_{REF IDEAL}[n-k]) \right) \quad (5.12)$$

This phase reference signal is then finally for the calculation of the RMS phase error according to equation 5.9. The measurement results for the evaluation of the modulated carrier differ strongly from the results for the unmodulated carrier if the channel model is not precise enough. This is due to the different lengths of the impulse response of the ISI filter and the one used for system identification. If the filter length used for system identification is too short, the system under observation cannot be identified correctly. But on the other hand if the filter length is longer the taps that are not required are mainly

determined by noise and therefore cause the reference signal to be distorted. Therefore the measured RMS phase error is increased for some disadvantageous situations. Using an algorithm that optimizes the filter length according to the phase noise might solve this problem. The differential evaluation of the RMS phase error during modulation suffers from the same problems as the absolute measurement.

As the phase noise measured during data transmission is influenced by ISI and the accuracy of the reference filter coefficients, the results are not reliable. Therefore the evaluation of the phase noise is done on the unmodulated carrier in the differential manner in order to consider the differential coding.

### 5.5.2 Noise Generation

To achieve a defined RMS phase noise for test purposes additional noise has to be artificially added to the system for test purposes. In [5] this is proposed by adding digitally generated Pseudorandom Noise (PRN) to the phase of the carrier in order to generate the desired amount of noise. The basic noise level present in the system has to be considered when doing so. For the current test setup this is a rather impractical method as the patterns of the FPGA box would have to be recalculated for each transmission, as otherwise the same 'noise' would always be present during transmission. However, the recomputation of a frame with different PN would take around 21 seconds on the used test setup. Thus, this solution is impractical in reality. Using this method is also not possible to generate noise during time where no data is transmitted. For the generation of the unmodulated carrier a predefined ideal sine is used and thus makes the generation of additional phase noise impossible.

Another approach is to generate noise with an AWG and to add this noise to the signal using a combiner. With this approach the noise generation and the signal generation would be independent. The level of the additional noise would have to be set accordingly. As the measured phase noise levels are anyhow borderline this method has not been applied and verified.

## 5.6 Summary

In this chapter the whole test setup and its properties were presented. The influence of the antenna on the signal shape and the mitigation of these effects using a preequalizer have been outlined. The different options for generating a test signal with defined ISI parameters have been investigated and a suitable method has been selected. It was found that the accurate determination of the sampling position is of utmost importance in order to measure the correct ISI parameters. Therefore the algorithm used in chapter 4 has been revised and a suitable algorithm based on correlation with the filtered reference signal has been recommended.

Also two different possibilities for evaluating the ISI cloud have been presented and it has been found that using the graphical evaluation even under ideal conditions does not deliver the desired results. The method based on system identification also outperforms the graphical approach in terms of robustness under noisy conditions. By investigating the overall test system's performance it has been found that it is not possible to generate test signals with the ISI filter operating at sample rate  $f_{sample}$  for all ISI parameters within the definition space under all conditions. An iterative optimization algorithm has been developed, but did not deliver satisfying results, as the execution time was too long. It has been proven that it is possible to generate and measure signals with ISI parameters within the definition space using the ISI filter operating at symbol rate  $f_{symbol}$  and interpolating the points using an exponential function. The measurement and generation of phase noise has been discussed and the method based on a differential measurement of the phase noise on the unmodulated carrier has been selected.

# 6. Test Method Verification

This chapter is dedicated to the verification of the test methodology under real conditions. The test system is used to generate signals with defined ISI and to perform reception tests according to [5] with the VHBR PICC evaluation system developed by NXP. To also verify the test method for PCD tests according to [5], measurements of the signal parameters captured with the Reference PICC using different PICC and PCD, antenna parameters are performed.

## 6.1 Automatisation

In order to run the tests automatically a test framework was set up. To control the FPGA box, the amplifier and the oscilloscope, the NXP reader library is used. The NXP reader library includes an interface to many different readers and supports the control of several measurement instruments. An interface to C#, which is used to implement the test cases using NUnit<sup>1</sup>, is provided by the NXP reader library. NUnit is a unit testing framework which provides management functionality for test cases and enables comfortable selection and execution of them. In figure 6.1 a screen shot of the Graphical User Interface (GUI) of NUnit is plotted. The different test cases can be selected on the left. Once the test is started all selected test cases are processed and the result is displayed. An advantage of NUnit is, that if one test case fails, the program is not aborted, it rather continues with the next one until all selected test cases are processed.

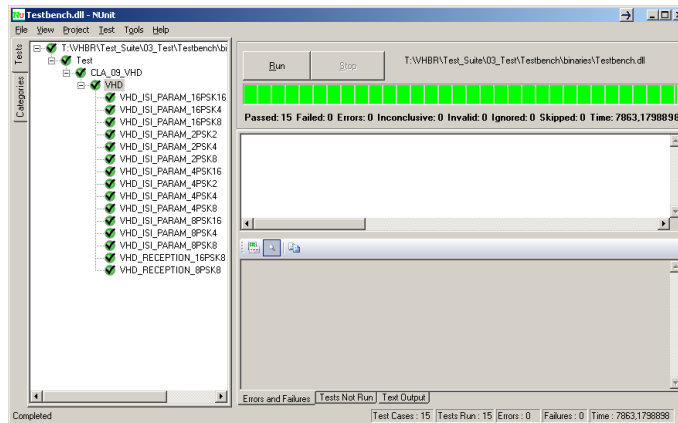


Figure 6.1: NUnit GUI

To provide an interface to the ISI analysis software written in MATLAB, the software is compiled as an executable and the input can be defined via a configuration file. Compiling the MATLAB analysis software to an executable has the advantage that only a MATLAB runtime environment has to be installed on the PC, on which the test software runs, and no licenses are required. By modifying the settings of the configuration file and launching the executable the analysis is started. In figure 6.2 a screen shot of the ISI analysis software is shown. It can be seen that already a few traces have been processed.

<sup>1</sup>[www.nunit.org](http://www.nunit.org)



Figure 6.2: VHD server screen shot

The result of the analysis is also written back into a file, which is then parsed. It is also possible to generate data frames with defined ISI parameters that are loaded into the FPGA box with this software. So there is no demand for MATLAB during the test execution. By offering a very simple interface it is also possible to use the analysis software as a standalone solution or an other software used for measurement automation such as LabVIEW<sup>2</sup> for example.

## 6.2 PICC Reception Tests

To verify the test method *PICC reception tests* using the VHBR PICC evaluation system are performed. This involves the generation of patterns with different ISI parameters within the parameters space for a reference transaction. These patterns have been calculated in advance using the exponential interpolation method. During the test run a pattern for particular ISI parameter set is loaded into the FPGA box and the reference transaction is performed several times in order to get reliable results. The raw Bit Error Rate (BER) before the error correction with the Hamming code, the resulting Frame Error Rate (FER) after the correction and also the number of block errors (BlkER) is evaluated. If the number of bit errors is equal to the number of block errors, meaning each block only contains one bit error, the Hamming code is able to correct the errors, otherwise it fails. To get reliable results the reference transaction is repeated several times for one ISI parameter set. The reception test covers the whole ISI parameter space and it is repeated for several field strengths.

An extraction of the log file for a 16PSK8 test run for a signal with  $ISI_m$  0.25 and 1.75 for an  $ISI_d$  of  $0^\circ$  at a field strength of 3 A/m can be seen below.

##### ISIm 0.25 ISId 0 #####	##### ISIm 1.75 ISId 0 #####
BER 0 BlkER 0 FER 0	BER 5 BlkER 5 FER 0
BER 0 BlkER 0 FER 0	BER 5 BlkER 5 FER 0
BER 0 BlkER 0 FER 0	BER 8 BlkER 8 FER 0
BER 0 BlkER 0 FER 0	BER 6 BlkER 6 FER 0
BER 0 BlkER 0 FER 0	BER 5 BlkER 5 FER 0
BER 0 BlkER 0 FER 0	BER 5 BlkER 5 FER 0
BER 1 BlkER 1 FER 0	BER 9 BlkER 9 FER 0
BER 1 BlkER 1 FER 0	BER 7 BlkER 7 FER 0

It can be seen that bit errors occur that can be corrected by the Hamming code. By further increasing the ISI parameters the VHBR PICC evaluations system have been determined. With this tests the test method for PICC reception test has been verified.

To demonstrate the capabilities of the signal generation and analysis a *special* VHBR test signal has been generated. The ideal constellation diagram of the generated test signal can

<sup>2</sup>[www.ni.com/labview/](http://www.ni.com/labview/)

be seen in figure 6.3 (a). Due to the differential encoding used, a slow phase drift does not influence the proper symbol detection. To generate the constellation diagram shown in (a) the phase of the signal is slowly ramped up and down in order to reach all constellation points, as can be seen in (b). The measured constellation diagram of the signal, which can be received error free by the VHBR PICC evaluation system, is visualized in (c).

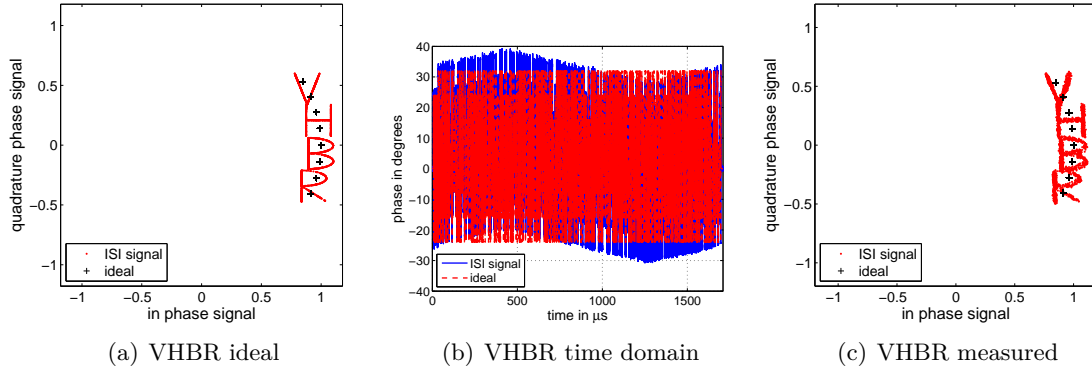


Figure 6.3: 8PSK VHBR test signal

### 6.3 PCD Transmission Tests

To check the test method, as well as to get an indication on which ISI parameters can be expected for practical systems, PCD transmission tests have been performed. A PCD test is to verify if the parameters of the signal present at the air interface are within the specification. Therefore the Reference PICC [13] is placed somewhere in the operational volume to capture the signal, whose ISI parameters are determined. For this measurement the Reference PICC is placed instead of the DUT.

Ideal rectangular modulation signals have been generated without the help of the pre-equalizer in order to measure the distortion introduced by the antenna. The same set of PCD antennas as in section 5.1.1 has been used, with a Q-factor of 8, 12 and 30. The resonant frequency is tuned to the carrier frequency for all measurements. Three different settings for the resonant frequency of the Reference PICC ranging from 13.56 MHz over 16.5 MHz to 19 MHz have been used to check their influence on the detuning of the PCD antenna and the resulting change of ISI parameters. The tests have been performed for the whole matrix of symbol durations and modulation orders. To verify the influence on the field strength, the tests have been repeated at 5 field strengths ranging from 1.5 A/m to 7.5 A/m. To simulate the behavior of the limiter in a real transponder the voltage at the Reference PICC was adjusted to 3 V for each field strength [13].

In table 6.1 the measured ISI parameters for the Q8 PCD antenna, a field strength of 3 A/m and the Reference PICC's resonant frequency tuned to 13.56 MHz can be seen. The ISI parameters are given using the notation  $ISI_m \angle ISI_d$ . For shorter symbol durations  $ISI_m$  significantly increases, as the transition time between two symbols gets shorter. For higher modulation orders  $ISI_m$  also increases as it is normalized to the symbol interval, which gets smaller for higher modulation orders. When considering the value of 0.22 for  $ISI_m$  for the 2PSK2 signal with a symbol interval of  $60^\circ$  and recalculating for a normalization to a symbol interval of  $20^\circ$  yields 0.66, which is exactly the value measured for the 4PSK2 signal. The absolute value of  $ISI_m$  is similar for all modulation orders with the same symbol duration. For longer symbol durations  $ISI_m$  gets very small thus making the measurement of  $ISI_d$  very sensitive to noise. This can be seen for the symbol durations of

8 and 16 carrier periods, where  $ISI_d$  shows a very large variance and has no significance anymore. The region of  $ISI_m$ , where  $ISI_d$  shows this large variance is anyhow clearly within the parameter space so the precise determination of  $ISI_d$  is not of importance. Only the ISI parameters measured for the 16PSK2 and 16PSK4 signal do not conform to the parameter space specified. The value of  $ISI_m$  for the 16PSK2 exceeds the limits, whereas for the 16PSK4 signal the value of  $ISI_d$  is not within the specification. But as these two combinations of symbol durations and modulation orders are anyhow not defined in the standard this does not matter.

	2PSKn	4PSKn	8PSKn	16PSKn
mPSK2	0.220/-6.0	0.660/-6.7	1.506/-6.7	<b>3.247/-6.2</b>
mPSK4	0.047/-21.1	0.139/-22.8	0.317/-23.6	<b>0.683/-23.1</b>
mPSK8	0.005/-29.4	0.003/-15.2	0.016/-49.4	0.020/-0.7
mPSK16	0.001/-69.4	0.001/-79.3	0.001/8.8	0.008/143.5

Table 6.1: Q8 antenna ISI parameters at 3 A/m

The measured values of  $ISI_m$  were not influenced by the different resonant frequencies of the Reference PICC. But the values of  $ISI_d$  were slightly influenced depending on the modulation order and the symbol duration. It was found that the field strength has, as well as the different resonant frequencies of the Reference PICC a minor influence on  $ISI_m$  and some influence on  $ISI_d$ . The resistor on the Q8PCD antenna when reducing the Q-factor gets very hot for higher field strengths and the resonant frequency of the PCD is detuned due to the temperature dependence of the matching network. To determine the influence of this effect a measurement series without the reference PICC and the signal captured at the calibration coil was performed. This measurement showed very similar trends to the measurement with the Reference PICC in the field. Therefore it can be concluded that the influence of the temperature dependence is larger than the detuning due to the Reference PICC in dependence of the field strength.

The measurement results of the ISI parameters of the Q30 antenna for a field strength of 3 A/m and the Reference PICC also tuned to 13.56 MHz are given in table 6.2. The measured values are significantly higher than for the Q8 antenna, due to the longer symbol transitions, as can be seen in figure 5.2. Thus the ISI parameters of more signals are not within the specification. All signals with a symbol duration of two fail, as well as the 8PSK4, 16PSK4 and 16PSK8 signals, where the 16PSK4 signal is not defined in the standard [15]. It has to be kept in mind that no preequalizer to compensate the ISI introduced by the antenna was used. When using a preequalizer it should be possible to generate signals that conform with the ISI parameter's space for all defined data rates.

	2PSKn	4PSKn	8PSKn	16PSKn
mPSK2	<b>0.679/-0.4</b>	<b>2.061/-1.1</b>	<b>4.787/-1.3</b>	<b>10.10/-1.3</b>
mPSK4	0.381/-3.7	1.149/-4.0	<b>2.690/-3.8</b>	<b>5.706/-4.1</b>
mPSK8	0.146/-7.5	0.442/-7.5	1.041/-7.9	<b>2.182/-7.9</b>
mPSK16	0.019/-17.6	0.056/-17.4	0.138/-15.9	0.293/-17.2

Table 6.2: Q30 antenna ISI parameters at 3 A/m

## 7. Conclusion

In this thesis a test methodology for Very High Bit Rates (VHBR) based on Phase Shift Keying (PSK) has been developed. This includes the selection of the instrument used for signal generation mainly based on the performance regarding phase noise. The FPGA box and an Arbitrary Waveform Generator (AWG) have been compared for that purpose. The FPGA box has been selected due to its better phase noise properties and due to the fact that it is already deployed at many test setups in the NXP laboratory. Furthermore the activation of VHBR based on communication on the standard data rates can be easily done using the standard functionality of the FPGA box. The built in preequalizer, which compensates the transfer function of the whole transmission chain additionally gave reason to choose the FPGA box.

The selection of the right measurement instrument for the signal analysis was also of importance. The properties of two state of the art signal analyzers using the IQ sampling mode, as well as a commercial signal analysis software running on one of the signal analyzers, and one state of the art oscilloscope have been compared regarding the analysis of PSK signals on a 13.56 MHz carrier. It was found that the Displayed Average Noise Level (DANL) is of importance in order to fulfill the stringent requirements of the phase noise of the signal. The signal analyzers showed a roughly 10 dB better DANL than the oscilloscope. But on the other hand the signal analyzers suffer from their operational principle involving analogue mixing, which leads to a feedthrough of the Local Oscillator (LO) at DC. This results in a strict limit for the analysis bandwidth and requires filters with very steep slopes in order to provide sufficient stop band attenuation.

It was found that due to this bandwidth limitation an ideal rectangular signal shows heavy ringing effects in some cases, this ringing can be explained by the Gibbs phenomenon. The oscilloscope generates the IQ baseband signal with the help of a digital IQ demodulator implemented in MATLAB. Also the estimation and correction of the frequency and phase error, as well as the determination of the right sampling position have been performed in MATLAB.

The signal analyzers do offer the possibility to synchronize to the 13.56 MHz reference signal, which makes the correction of the frequency error unnecessary. No difference in the measurement results has been observed between locking the signal analyzers oscillator to the signal generator and operating all instruments in free running mode and performing an estimation and correction of the frequency error. The oscilloscope does not offer the option to synchronize to an external reference signal and therefore the frequency error has to be corrected during postprocessing.

The constellation diagrams recorded with the signal analyzers suffer severely from the ringing effect for shorter symbol durations, whereas the signals recorded with the oscilloscope only show a small amount of noise. The measured RMS phase error of a 4PSK2 is with  $0.23^\circ$  for the oscilloscope a decade below the result of the signal analyzers with  $2.3^\circ$ . Therefore the oscilloscope together with the signal processing implemented in MATLAB was chosen for the signal analysis. Furthermore the oscilloscope as well as the FPGA box are already included in the contactless test setups to characterize conventional ISO/IEC 14443 smart card products, which was seen as a further argument, as no additional measurement instrument is required.

The influence of Proximity Coupling Devices (PCD) antennas with different Q-factors on the generated signal has been analyzed and the mitigation of these effects using the preequalizer of the FPGA box has been described. The different options to generate a test signal with well defined ISI parameters have been investigated and compared. The importance of the synchronization of the sampling with the symbol timing was figured out during the first measurements of the Inter Symbol Interference (ISI) parameters. Therefore the algorithm used for synchronization had been revised and an appropriate algorithm based on correlation with a filtered reference signal has been selected. Additionally the measurement of the ISI parameters has been investigated.

The different performances of the system identification algorithm proposed by the standard and a graphical evaluation algorithm to determine the ISI parameters have been outlined. It was found that the graphical solution does not deliver the correct results for values of  $ISI_m$  larger than 1 and for values of  $ISI_d$  around  $-180^\circ$ , even under noiseless conditions. The influence of noise on the performance of the system identification algorithm is significantly lower than the one for the algorithm based on the graphical evaluation. Comparing the RMS  $ISI_d$  error of the graphical evaluation ( $3.85^\circ$ ) and the system identification algorithm ( $0.178^\circ$ ) for a 4PSK signal with 2048 symbols and  $0.25^\circ$  RMS phase noise frame results in a difference by a factor of 20. The relation for the RMS  $ISI_m$  error is similar. Hence the system identification algorithm was used to measure the ISI parameters.

The overall system performance has been evaluated and it has been found that the generation and measurement of the test signal of the ISI filter running at the sample rate does not deliver the same results. Therefore the method using the exponential interpolation between the ISI constellation points calculated at symbol rate was chosen for the test signal generation. Furthermore different methods for measuring the phase noise and their robustness have been analyzed. It was found that the measurement of the noise during modulation is severely influenced by the precision of the system identification. Thus the phase noise is measured on the unmodulated carrier before a frame is transmitted. Moreover the prospects for the generation of additional phase noise have been described.

Finally the test methodology has been verified by performing a Proximity Card (PICC) reception test with the VHD evaluation system. By performing measurements on different antenna systems using ideal signals as input, the signal analysis chain has been verified and the range of ISI parameters that can be expected has been determined.

The test setup is now so far developed to be able to perform acPICC reception tests with signals containing defined ISI with a maximum frame length of 2.3 ms. Furthermore the verification of PCD signals with angles of  $ISI_d$  below  $90^\circ$  can be done. The current test setup will be used to perform PICC reception tests with the VHD evaluation system as well as with cards featuring VHBR. In a future update the signal processing for the test signal generation will be implemented in the FPGA box, removing the 2.3 ms limit and avoiding the time consuming downloads of the waveforms.

# Bibliography

- [1] *ISO/IEC 14443-1: Identification cards — Contactless integrated circuit cards — Proximity cards — Part 1: Physical characteristics*, 2<sup>nd</sup> edition, June 2008.
- [2] *ISO/IEC 14443-2: Identification cards — Contactless integrated circuit cards — Proximity cards — Part 2: Radio frequency power and signal interface*, 2<sup>nd</sup> edition, September 2010.
- [3] *ISO/IEC 14443-3: Identification cards — Contactless integrated circuit cards — Proximity cards — Part 3: Initialization and anticollision*, FDIS 2<sup>nd</sup> edition, November 2009.
- [4] *ISO/IEC 14443-4: Identification cards — Contactless integrated circuit cards — Proximity cards — Part 4: Transmission protocol*, 2<sup>nd</sup> edition, July 2008.
- [5] *ISO/IEC 10373-6:2010/WDAM 4: Identification cards — Test methods — Part 6: Proximity cards: Working Draft Amendment 4 Bit rates higher than  $f_c/16$  up to  $f_c$* , October 2010.
- [6] M. Gebhart. *Lecture RFID Systems*, 2009.
- [7] K. Finkenzerler. *RFID Handbook: Fundamentals and Applications in Contactless Smart Cards and Identification*. WILEY, 2<sup>nd</sup> edition, 2003.
- [8] *ISO/IEC 7816: Identification cards — cards with contacts*.
- [9] *ISO/IEC 10536: Identification cards — Contactless integrated circuit(s) cards - Part 1-4*.
- [10] *ISO/IEC 15693: Identification cards - Contactless integrated circuit cards - Vicinity cards - Part 1-3*.
- [11] W. Riedler, E. Leitgeb. *Vorlesungsskript Hochfrequenztechnik*, 2007.
- [12] B. Sklar. *Digital communications: fundamentals and applications*. Prentice-Hall PTR, 2<sup>nd</sup> edition, 2001.
- [13] *ISO/IEC FDIS 10373-6:2010(E): Identification cards — Test methods — Part 6: Proximity cards*, 1<sup>st</sup> edition, March 2010.
- [14] *ISO/IEC 14443-1:2008/FDAM:2010(E): Identification cards — Contactless integrated circuit cards — Proximity cards — Part 1: Physical characteristics: Amendment 1: Additional PICC classes*, April 2010.
- [15] *ISO/IEC 14443-2:2010/PDAM 1: Identification cards — Contactless integrated circuit cards — Proximity cards — Part 2: Radio frequency power and signal interface: Amendment 1 Bits rates higher than  $f_c/16$  and up to  $f_c$* , October 2010.

- [16] *ISO/IEC 14443-4:2010/PDAM 2: Identification cards — Contactless integrated circuit cards — Proximity cards — Part 4: Transmission protocol: Amendment 2: Activation of bit rates up to  $f_c$ , protocol activation of PICC Type A and increased frame size*, September 2010.
- [17] *ISO/IEC 14443-3:2010/PDAM 2: Identification cards — Contactless integrated circuit cards — Proximity cards — Part 3: Initialization and anticollision: Amendment 2 Bit rates higher than  $f_c / 16$  up to  $f_c$  and increased frame size*, November 2010.
- [18] T. Roermund, L. Szóstek. A study on bandwidth efficiency for very high datarates for smart cards. Technical Report Technical Note NXP-TN-2010-0049, NXP Semiconductors, October 2010.
- [19] T. Roermund, L. Szóstek. ISO/IEC 14443: Changes for Hamming and CRC. Technical report, NXP Semiconductors, November 2010.
- [20] *ISO/IEC 14443-4:2008/FDAM 1:2010(E): Identification cards — Contactless integrated circuit cards — Proximity cards — Part 4: Transmission protocol: Amendment 1: Exchange of additional parameters*, September 2010.
- [21] M. Gebhart, S. Birnstingl, J. Bruckbauer, E. Merlin. Properties of a Test Bench to Verify Standard Compliance of Proximity Transponders, July 2008.
- [22] R. Stadlmair and M. Gebhart. Cadence Simulation Environment for Contactless Near-Field Communication tags. submitted to the 11th International Conference on Telecommunications (CONTEL), June 2011.
- [23] Tabor Electronics Inc. 250 MS/s Dual-Channel Arbitrary Waveform / Function Generator Model WW2572A. <http://www.taborelec.com/pdf/WW2572A.pdf>, February 2011.
- [24] [http://www.radioradar.net/files/Image/articles/technics\\_measurements/tabor/ww2572.jpg](http://www.radioradar.net/files/Image/articles/technics_measurements/tabor/ww2572.jpg), February 2011.
- [25] C. Rauscher, V. Janseen, R. Minihold. *Grundlagen der Spektrumanalyse*. Rohde&Schwarz, 1<sup>st</sup> edition, 2000.
- [26] Agilent. *N9020A MXA X-Series Signal Analyzer Data Sheet*, December 2010.
- [27] <http://www.rohde-schwarz.at/live/rs/mediadb/pspic/image/32/FSV30img491983c46f3fc.jpg>, February 2011.
- [28] [http://cp.home.agilent.com/upload/cmc\\_upload/N9020A\\_XA8\\_800x428.jpg](http://cp.home.agilent.com/upload/cmc_upload/N9020A_XA8_800x428.jpg), February 2011.
- [29] [www.testmart.com/webdata/proding/LEC\\_WRXi\\_64Xi\\_Left\\_lg.jpg](http://www.testmart.com/webdata/proding/LEC_WRXi_64Xi_Left_lg.jpg), February 2011.
- [30] Rohde&Schwarz. *R&S FSV Signal and Spectrum Analyzer Specifications*, February 2010.
- [31] D. Seebacher, M. Gebhart, M. Stark. Selection of the Appropriate Measurement Instrument for Very High Data Rate Contactless Transponder Conformance Evaluation. submitted to IEEE International Conference on RFID-Technologies and Applications (RFID-TA), 2011.
- [32] Rohde&Schwarz. *R&S FSV-K70 Firmware Option Vector Signal Analysis Operating Manual*, 2010.

- [33] LeCroy. *Application Note A006A: Enhanced Resolution*.
- [34] STMicroelectronics. *Application Note AN2668: Improving STM32F101xx and STM32F103xx ADC resolution by oversampling*, 1<sup>st</sup> edition, July 2008.
- [35] Amplifier Research. *Model 75A250A Specifications*, revision 090503 edition.
- [36] U. Mühlmann. Pulse shaping in ISO/IEC14443 measurement systems using inverse system parameters for feed-forward compensation. submitted to IEEE International Conference on RFID-Technologies and Applications (RFID-TA), 2011.

# List of Figures

2.1	Components of a contactless RFID system [6]	3
2.2	Classification of a RFID system [7]	4
2.3	Contact(less) IC cards and applicable standards [7]	4
2.4	Architecture of a memory card [6]	5
2.5	Architecture of a microprocessor card [6]	5
2.6	Contactless card architecture [7]	6
2.7	Dual interface card architecture [7]	6
2.8	Illustration of the definition of inductance [7]	7
2.9	Illustration of the definition of mutual inductance [7]	7
2.10	Mutual inductance of two loops	8
2.11	Magnetic field strength over a short cylinder coil	11
2.12	Magnetic field in the near/far field region for 13.56 MHz [6]	11
2.13	Transponder Q-factor in dependence of the magnetic field [6]	12
2.14	$H_{min}$ in dependence of $f_{res}$ of the transponder antenna	13
2.15	Detuning in dependence of coupling coefficient [6]	13
2.16	Basic load modulation schematic [7]	14
2.17	Generation of the subcarrier modulated signal [6]	14
2.18	Load modulation with $f_{carrier} = f_{res}$ [7]	15
2.19	Load modulation with $f_{carrier} < f_{res}$ [7]	15
2.20	Load modulation amplitude minimum limits for a class 1 antenna [2]	16
2.21	Basic modulation schemes	16
2.22	PSK symbol constellation diagrams	17
2.23	Different line codes [7]	18
3.1	Life cycle of an international standard [6]	20
3.2	Life cycle of an amendment [6]	21
3.3	Class 1 antenna size [1]	21
3.4	Coding PCD to PICC [2]	22
3.5	Coding PICC to PCD [2]	22
3.6	Pause A for PCD to PICC transmission [2]	23
3.7	Type A state diagram [3]	24
3.8	Collision detection for NRZ and Manchester coding [7]	25
3.9	Activation sequence [4]	26
3.10	Structure of the ATS [4]	27
3.11	PSK symbol constellations for PCD to PICC communication [15]	28
3.12	PSK and ISI parameter definition [15]	29
3.13	VHBR coding chain [15]	30
3.14	Coaxial antenna arrangement according to ISO/IEC 10373-6 [13]	32
3.15	Antenna assembly profile [13]	32
3.16	Antenna resonator modelling [5]	33
4.1	Generators	34

4.2	Spectrum of signal generators at a span of 4MHz. . . . .	35
4.3	Generators 2PSK8 frame . . . . .	36
4.4	Analyzers . . . . .	37
4.5	Signal processing chain FSV, modified [32] . . . . .	39
4.6	Signal processing chain oscilloscope . . . . .	39
4.7	Synchronization chain MATLAB . . . . .	40
4.8	Frequency and phase error correction . . . . .	40
4.9	FSV sampling frequency IQ vector . . . . .	41
4.10	FSV sampling frequency spectrum . . . . .	42
4.11	16PSK8 demodulated signal . . . . .	42
4.12	16PSK8 simulated . . . . .	43
4.13	RMS phase error vs. relative symbol grid position, oscilloscope . . . . .	43
4.14	RMS phase error vs. relative symbol grid position, analyzer . . . . .	44
4.15	4PSK2 constellation diagrams . . . . .	45
4.16	16PSK2 constellation diagrams . . . . .	45
4.17	Phase noise spectrum of all instruments . . . . .	45
5.1	NXP ISO test setup . . . . .	47
5.2	16PSK8 time domain signal for different Q factors of antenna . . . . .	48
5.3	Preequalizer transfer functions . . . . .	49
5.4	Signal after preequalizer . . . . .	49
5.5	16PSK $n$ time domain signals with preequalizer . . . . .	50
5.6	16PSK8 ISI signals . . . . .	51
5.7	4PSK $n$ ISI cloud in dependence of sampling position . . . . .	52
5.8	16PSK8 frame with $t_{sample}$ of max-var algorithm . . . . .	53
5.9	Correlation algorithms performance . . . . .	54
5.10	ISI parameter space . . . . .	55
5.11	ISI evaluation algorithms performance 4PSK $n$ signal . . . . .	56
5.12	ISI evaluation algorithm 4PSK $n$ noise influence . . . . .	57
5.13	4PSK $n$ ISI cloud evaluation points . . . . .	58
5.14	ISI parameter RMS error in dependence of frame length . . . . .	58
5.15	Demodulation filter influence on ISI parameters . . . . .	59
5.16	Demodulation filter influence 4PSK2 $ISI_m$ 0.5 . . . . .	60
5.17	Initial and corrected parameters for a 4PSK $n$ signal simulation . . . . .	61
5.18	Initial and corrected parameters measured for a 4PSK $n$ signal . . . . .	61
5.19	Measured ISI parameters using exponential interpolation method . . . . .	62
6.1	NUnit GUI . . . . .	66
6.2	VHD server screen shot . . . . .	67
6.3	8PSK8 VHBR test signal . . . . .	68

# List of Tables

2.1	Hamming(7,4) code . . . . .	19
3.1	Data rates PCD to PICC and PICC to PCD [2] . . . . .	22
3.2	Subcarrier frequencies for VHBR, PICC to PCD communication [15] . . . . .	28
3.3	mPSK <sub>n</sub> bit rates for VHBR [15] . . . . .	29
3.4	ISI limits for PCD and PICC [15] . . . . .	30
3.5	SOF for VHBR [15] . . . . .	30
4.1	Phase noise Tabor WW2572A [23] . . . . .	36
4.2	Phase noise of the analyzers [30][26] . . . . .	38
4.3	RMS phase error 4PSK <sub>n</sub> signal . . . . .	46
5.1	ISI evaluation algorithms performance 4PSK <sub>n</sub> signal . . . . .	56
6.1	Q8 antenna ISI parameters at 3 A/m . . . . .	69
6.2	Q30 antenna ISI parameters at 3 A/m . . . . .	69

# List of Abbreviations

AAF	Anti Aliasing Filter
AC	Anticollision Command
AM	Amplitude Modulation
ASK	Amplitude Shift Keying
ATS	Answer To Select
ATTRIB	PICC selection command Type B
ATQA	Answer to Request Type A
ATQB	Answer to Request Type B
AWG	Arbitrary Waveform Generator
BCC	Block Check Character
BER	Bit Error Rate
BPSK	Binary Phase Shift Keying
CICC	Close Coupled Card
CID	Card IDentifier
CIU	Contactless Interface Unit
CPU	Central Processing Unit
CRC	Cyclic Redunandcy Check
DAC	Digital to Analog Converter
DANL	Displayed Average Noise Level
DBP	Differential Biphase Coding
DUT	Device Under Test
EAS	Electronic Article Surveillance
EEPROM	Electrically Erasable and Programmable Read Only Memory
EMC	Electromagnetic Compatibility
ETU	Elementary Time Unit
FDT	Frame Delay Time

FEC	Forward Error Correction
FER	Frame Error Rate
FIR	Finite Impulse Response
FPGA	Field Programmable Gate Array
FSCI	Frame Size for proximity Card Integer
FSD	Frame Size for proximity coupling Device
FSDI	Frame Size for proximity coupling Device Integer
FSK	Frequency Shift Keying
FWT	Frame Waiting Time
GUI	Graphical User Interface
HLTA	Halt Command Type A
HF	High Frequency
IC	Integrated Circuit
IEC	International Electrotechnical Commission
IF	Intermediate Frequency
iid	independent and identically distributed
ISI	Inter Symbol Interference
ISM	Industrial Scientific and Medical
ISO	International Organization for Standardization
IQ	Inphase Quadrature
LO	Local Oscillator
LSB	Least Significant Bit
mPSK	multiple Phase Shift Keying
NAD	Node ADdress
NCO	Numerical Controlled Oscillator
NFC	Near Field Communication
NRZ	Non Return to Zero
NVB	Number of Valid Bits
OOK	On Off Keying
OS	Operating System
PCD	Proximity Coupling Devices
PICC	Proximity Card4

PLL	Phase Locked Loop
PM	Phase Modulation
PPS	Protocol and Parameter Selection
PRN	Pseudorandom Noise
PSK	Phase Shift Keying
RAM	Random Access Memory
RATS	Request for Answer To Select
REQA	Request Command Type A
RFID	Radio Frequency Identification
RFU	Reserved for Future Use
RICC	Remote Coupled Card
RMS	Root Mean Square
ROM	Read Only Memory
RZ	Return to Zero
SAK	Select Acknowledge
SEL	Selection code
SFGT	Start-up Frame Guard Time
SNR	Signal to Noise Ratio
SOF	Start Of Frame
UID	Unique IDentifier
VHBR	Very High Bit Rates
VHD	Very High Data Rates
VICC	Vicinity Card
VSA	Vector Signal Analyzer
WUPA	Wake Up Command Type A